Interface Engineering of Solid-State Li Metal Batteries with Garnet Electrolytes

Jianfeng Cheng

2023

Table of Contents

Chapter 1 Introduction

1.1 Purpose of the Study

Increasing concerns on environmental pollution propel the development of electrification of transport worldwide. For example, according to a United States Environmental Protection Agency report, the transportation sector accounted for the most significant portion, 27%, of the total greenhouse gas emissions in the U.S. in 2020 (Figure 1.1). Specifically, cars, trucks, aircraft, trains, and ships contribute to transportation emissions.

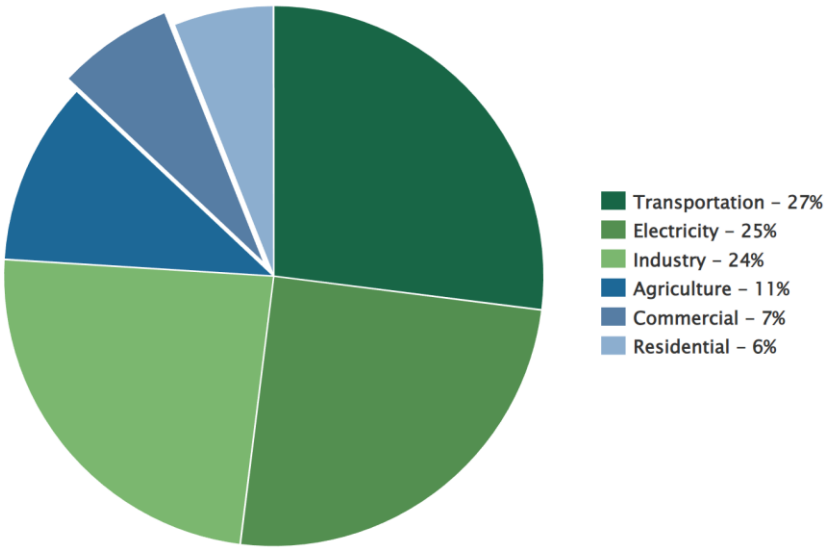

Figure 1.1 U.S. greenhouse emissions by sector in 2020.

https://www.epa.gov/greenvehicles/fast-facts-transportation-greenhouse-gas-emissions

As a result, reducing transportation emissions is one of the most important steps to tackling the climate emergency. It is necessary to shift away from gasoline or diesel-powered vehicles to electric vehicles (EVs). The critical component of an EV is the battery. In addition, using renewable energies, such as wind and solar energies, would be a great advantage because it can help to reduce fossil fuel usage, the largest source of carbon dioxide, and it can also help to mitigate the energy deficit. However, the sun does not always shine, and the wind does not always blow. Advanced

energy storage systems, i.e., advanced batteries, are required to use renewable energy resources more efficiently.

On July 14, the European Union announced an effective ban on selling new gasoline and diesel cars from 2035. This will undoubtedly speed up the switch to zero-emission EVs to counter global warming. As reported by Bloomberg New Energy Finance, EVs will cost almost the same as their internal combustion counterparts, which is believed to be the point of the liftoff for EV sales. This is evidenced by the fact that Tesla's stock jumped to a new record high last October. The automaker's market capitalization reached US$1 trillion, becoming the sixth company in U.S. history to achieve this record. Yet the world's first mass-produced 100% EV was Nissan LEAF, officially launched in 2010. Taking the Nissan LEAF 2021 as an example, it can go up to 458 km on a single charge with a standard 62 kWh battery pack (Figure 1.2). The battery life is estimated to be 8 years or 160,000 km in everyday use.

Figure 1.2 Nissan LEAF 2021. https://www.nissan.co.jp/

Nevertheless, many people have been deterred by the driving range anxiety because there is a lack of public charging stations. In addition, Li-ion batteries with a liquid electrolyte are potentially dangerous as the liquid electrolyte is usually flammable.

Rechargeable Li metal batteries are widely regarded as the next-generation batteries with a high energy density. This is because the Li metal anode has a high theoretical specific capacity (3860

mA h g^{-1}, about 10 times higher than a graphite anode) and the lowest redox potential of -3.04 V vs. a standard hydrogen electrode (SHE). Thus, the driving range of EVs powered by Li metal batteries is expected to increase significantly. However, uncontrollable Li dendrite growth and other side reactions between Li metal and common liquid electrolytes make its practical use as an anode material impossible. On the other hand, solid electrolytes, such as garnet-type $Li_7La_3Zr_2O_{12}$ (LLZO), can physically suppress the initiation and propagation of Li dendrite to a large extent because of their relatively high elastic and shear moduli. LLZO is also stable in dry air, odorless,

and chemically compatible with a Li metal anode. Thus, solid-state Li metal batteries are a potentially game-changing technology with many advantages, such as far less flammable, wider temperature windows, higher energy densities, and faster charging times.

This study aims to develop solid-state Li metal batteries with a garnet or a garnet-based solid electrolyte. Since LLZO is intrinsically brittle, forming good physical contact between LLZO and electrode materials is difficult, especially with the cathode materials. Therefore, solving the interfacial contact issue between LLZO and cathode materials, usually ceramic oxides, is crucial for the development of LLZO-based solid-state Li metal batteries. It is possible to mitigate the interfacial contact issue by developing an LLZO-based flexible sheet electrolyte or a quasi-solid-state composite cathode, where the active cathode material can be layered oxide $LiCoO_2$ (LCO) or high-nickel layered oxides (NMC). The research results are briefly presented and discussed here.

1.2 Brief Introduction of LLZO

A research group led by Prof. Werner Weppner at the University of Kiel, Germany, first reported Li^+ transport properties of a garnet-type solid-electrolyte, $Li_5La_3M_2O_{12}$ (M=Nb, Ta), in 2003. The lithium-stuffed garnet $Li_5La_3Ta_2O_{12}$ exhibited a relatively high Li^+ conductivity in the order of 10^{-6} S cm^{-1} [1]. The relatively high ionic conductivity and chemical stability of $Li_5La_3Ta_2O_{12}$ attracted

tremendous research attention on Li^+ conductivity optimization through appropriate structural and chemical composition modifications. The replacement of tetravalent Zr for M in $Li_5La_3Ta_2O_{12}$ led to the discovery of garnet-type $Li_7La_3Zr_2O_{12}$ in 2007, also by Prof. Weppner's research group. The cubic LLZO sintered at 1230 ℃ in an alumina crucible showed a high ionic conductivity, in the order of 10^{-4} S cm^{-1}, and good chemical stability against molten Li. However, LLZO exists in tetragonal and cubic polymorphs [2]. The tetragonal, LLZO sintered at relatively lower temperatures, shows a much lower ionic conductivity (about 10^{-6} S cm^{-1}) than the cubic counterpart.

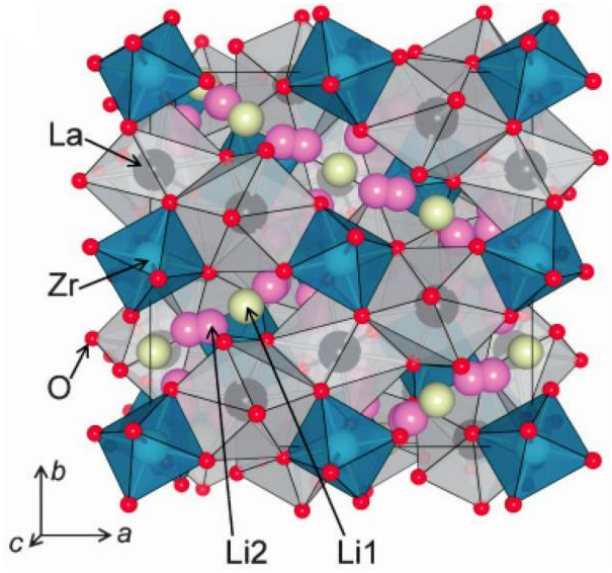

Figure 1.3 Crystal structure of cubic $Li_7La_3Zr_2O_{12}$ [3]

A milestone for the synthesis of cubic LLZO was achieved in 2011. Geiger et al. found that a small amount of Al-doping (incorporated from the alumina crucibles during high-temperature sintering) could help stabilize the LLZO cubic structure (Figure 1.3) [4]. As a result, Al_2O_3 powder has been widely used as one of the starting materials for the synthesis of cubic LLZO. At the same year, a research group led by Prof. Kiyoshi Kanamura at Tokyo Metropolitan University applied cubic LLZO as a solid electrolyte in an Li/LCO full cell for the first time.

Based on *ab initio* calculations, Li-ions are generally supposed to migrate through the adjacent Li(2) and Li(1) sites, as shown in Figure 1.4 [5]. The energy barrier for such a migration path was calculated to be only 0.26 eV, which explained the high ionic conductivity of cubic LLZO at room temperature.

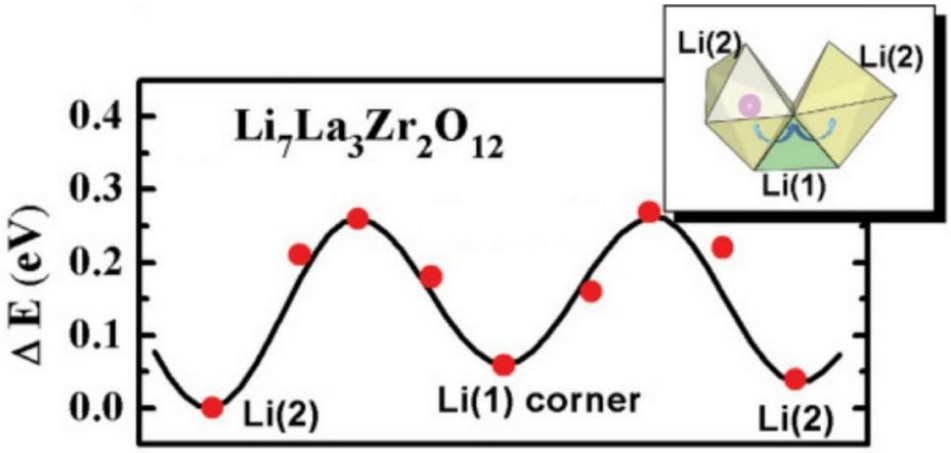

Figure 1.4 Li^+ transport mechanism in cubic $Li_7La_3Zr_2O_{12}$ [5]

For the electrochemical window, although experimental results indicate that LLZO has a very high oxidation potential above 5 V relative to Li/Li^+, *ab initio* calculations suggest that the electrochemical window of cubic LLZO is only in the range of 0.05 to 2.91 V vs. Li/Li^+ [6]. One explanation is that decomposed interphases form a protection layer on the solid electrolyte, preventing further decomposition. In addition, the decomposition of the interphases provides an extra electrochemical window. Overall, cubic LLZO is a promising solid electrolyte for Li metal batteries.

1.3 Issues of LLZO solid electrolyte

From an engineering point of view, high-temperature sintering for large-scale production of membrane LLZO is very difficult. Due to the intrinsically brittle nature of polycrystalline LLZO, it is difficult for LLZO to form good interfacial contact with the electrode, especially with the cathode, which usually results in high interfacial resistance. In addition, high-temperature sintering

(e.g., 1200 ºC) is necessary to densify the LLZO powders, while Li loss and various side reactions are likely to occur at high temperatures. Moreover, integrating a thin LLZO membrane into a Li metal battery is challenging because thin LLZO membranes are very fragile.

1.4 Flexible LLZO-based composite sheet electrolyte

PEO-based flexible sheet electrolytes with LLZO and Li salts as ionic conducting promoters have been reported [7,8]. The ceramic-in-polymer sheet electrolyte containing 60 wt% of LiTFSI and 34 % of Ta-doped LLZO showed a high ionic conductivity of 1.2×10^{-4} S cm^{-1} at 30 °C. However, the Li salt content was as high as 60 wt% (very expensive) and it was also difficult to scale up the production of the sheet electrolyte by hot pressing.

We thus adapted a different approach to producing LLZO-based composite flexible sheet electrolytes. An Al-LLZO powder and a polystyrene-type elastomeric binder were ball-mixed in toluene. The slurry was tape cast onto a polyethylene terephthalate (PET) substrate at room temperature, following drying at 80 ℃ for 6 h in vacuum. The thickness of the sheet could be easily controlled in the range of several tens to several hundreds of micrometers. After drying, the sheet could be easily peeled off from the PET substrate and was self-standing. Although the Al-LLZO content in the sheet electrolyte was as high as 90 wt%, the sheet could be folded and twisted without breaking, demonstrating good flexibility and mechanical stability. Cross-sectional SEM micrographs revealed the porous structure of the tape-cast sheet electrolyte, where nano-sized pores were observed among primary Al-LLZO particles (Figure 1.5). In contrast, micro-sized pores were observed among secondary Al-LLZO particles. The porosity of the as-cast sheet was estimated to be 50%.

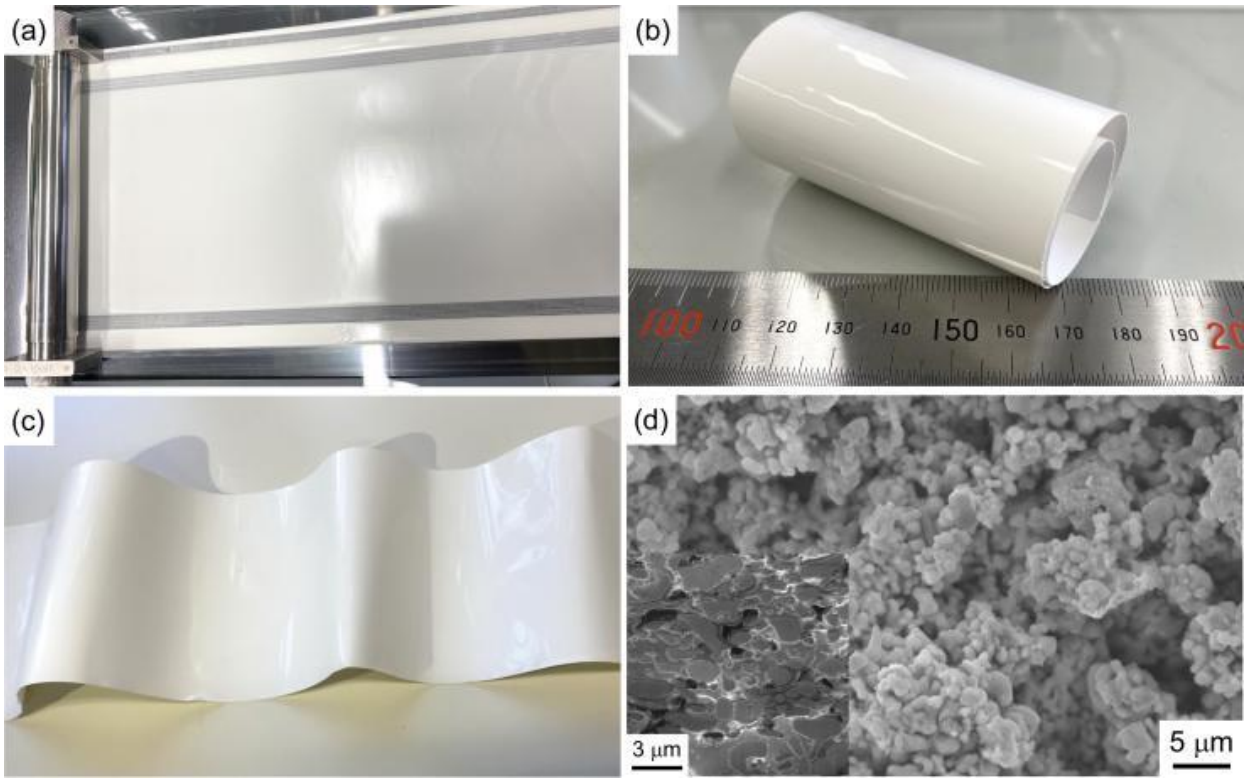

Fig. 1.5 Optical and SEM images of the flexible Al-LLZO sheet electrolyte after drying. (a) Tape-casting of the Al-LLZO sheet on a 75 μm-thick PET substrate, (b) Self-standing Al-LLZO sheet after peeling off the PET substrate, (c) Dry sheet with a thickness of 350 μm shows good flexibility, (d) Fractured cross-section of the sheet electrolyte. The inset shows a cross-section of the sheet cut by focused ion beam (FIB).

To increase the ionic conductivity of the sheet electrolyte, we cold-pressed the sheet to reduce its porosity. However, particle rearrangement and consolidation through plastic deformation were almost completed when the sheet was cold pressed at 700 MPa. The porosity of the sheet electrolyte was decreased to 15 % accordingly, while its ionic conductivity could only reach 1.2×10^{-9} S cm^{-1} at 25 ℃ through cold pressing. To further improve the ionic conductivity of the sheet electrolyte, the sheet electrolyte was impregnated with a solvate ionic liquid (IL). The absorbed IL content was proportional to the sheet porosity, which could be tuned by cold-pressing. The IL uptake by the

100 MPa cold-pressed sheet was 14.6 wt%, corresponding to 32 vol%. Based on percolation theory [9], a solid-liquid system would become locked when the liquid was less than 30 vol%. This is because the liquid became discontinuous and was unable to flow. Therefore, 100 MPa was slightly lower than the ideal pressure.

The cell delivered an initial discharge capacity of 126 mA h g^{-1} at 30 °C and 117 mA h g^{-1} at 60 °C. However, noticeable capacity fading was observed after a few cycles. The instability of the solvate IL was believed to be one of the main reasons for the capacity degradation. Thus, searching for a suitable IL is essential for developing the quasi-solid-state LLZO-based composite flexible sheet electrolyte.

1.5 Quasi-solid-state composite cathode

Another way to counter the interfacial resistance issue between the cathode and the LLZO solid electrolyte is to introduce a small amount of IL into the cathode. A Li metal battery with an IL-containing quasi-solid-state $LiFePO_4$ (LFP) cathode and an Al-LLZO pellet electrolyte was reported by a research group led by Prof. Honma at Tohoku University in 2018 [10]. Similarly, we developed an IL-containing quasi-solid-state LCO cathode here. The pre-introduction of an IL effectively reduced the cathode-side interfacial resistance. Compared with the solvate IL of Li(G4)FSI, a conventional IL of 1 mol dm^{-3} LiTFSI/EMI-TFSI, designated ET, was found to be more electrochemically stable. In addition, although excessive IL can thoroughly wet the solid-state LCO/Al-LLZO interface, electron transport can also be blocked because the IL is electrically insulating. Meanwhile, particle (e.g., LCO and carbon black) agglomeration is also likely to occur, reducing the utilization rate of LCO. The cycling performance of the quasi-solid-state LCO cathode with the ET IL (7.8-17.6 wt%) is shown in Figure 6.

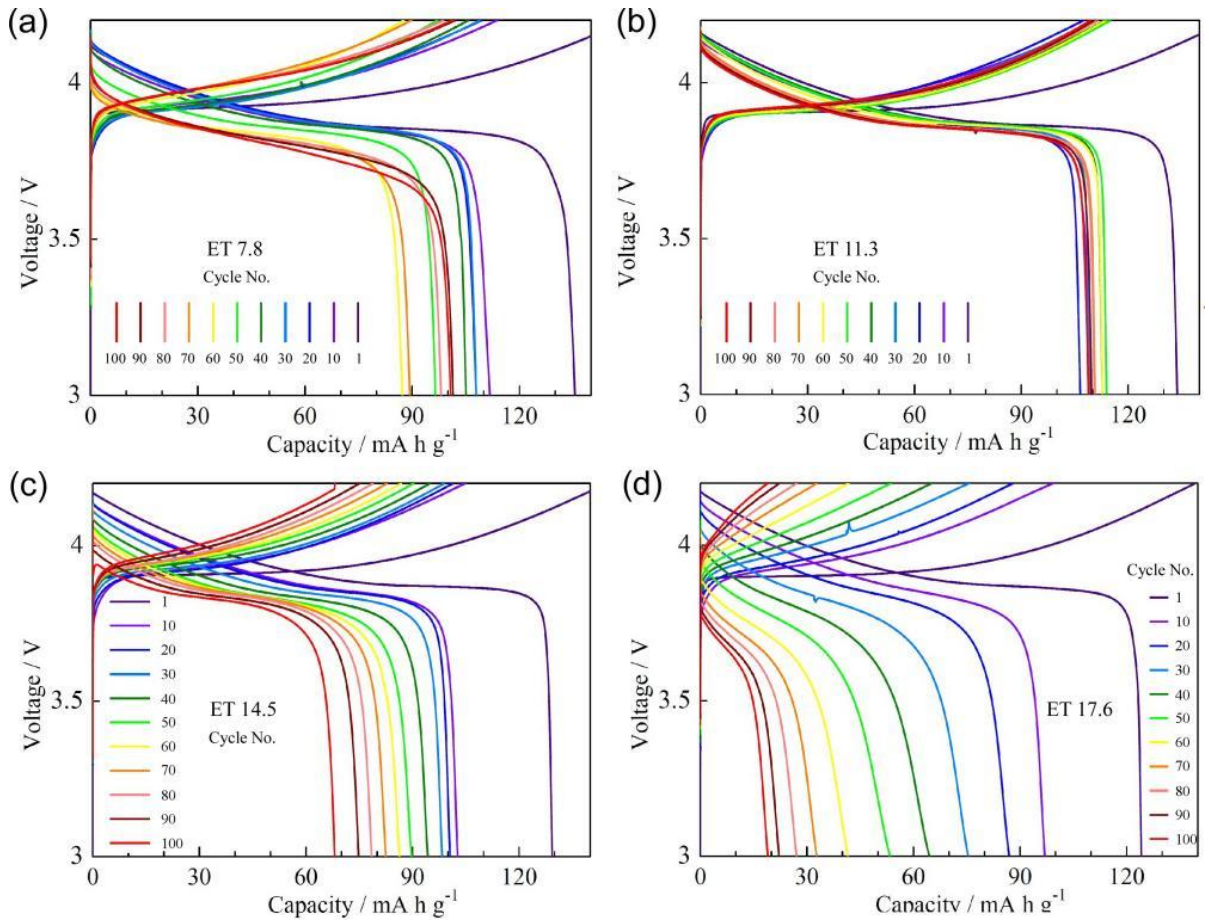

Figure 1.6 Cycling performance of the quasi-solid-state LCO cathode with the ET IL at 60 °C.

The optimal content of the ET IL was found to be 11.3 wt%. However, noticeable capacity decay of the quasi-solid-state Li/Al-LLZO/LCO cell was observed with cycling. The increase in the overall resistance of the cell also indicated this. We assumed that there were interfacial reactions between the IL and the LCO active material. The stability of LCO against the ET IL was investigated using XPS and TEM. Failure mechanisms of the quasi-solid-state Li/Al-LLZO/LCO cell are illustrated in Figure 1.7. First, GF was thermally decomposed after prolonged cycling at 60 °C, as indicated by the FTIR analysis, although it was electrochemically stable up to 4.5 V vs. Li/Li^+. On the other hand, ET became electrochemically oxidized at potentials slightly above 4.0 V vs. Li/Li^+, as evidenced by LSV and CV analysis. Thus the primary reasons accounting for the

decay of the cell could be: dissociation or desolvation of the ILs, cracking and agglomeration of LCO particles, the continuous growth of the CEI layer on LCO, reactions between the ILs and the Al current collector, and the blocking of the charge transfer pathway between LCO and the Al current collector.

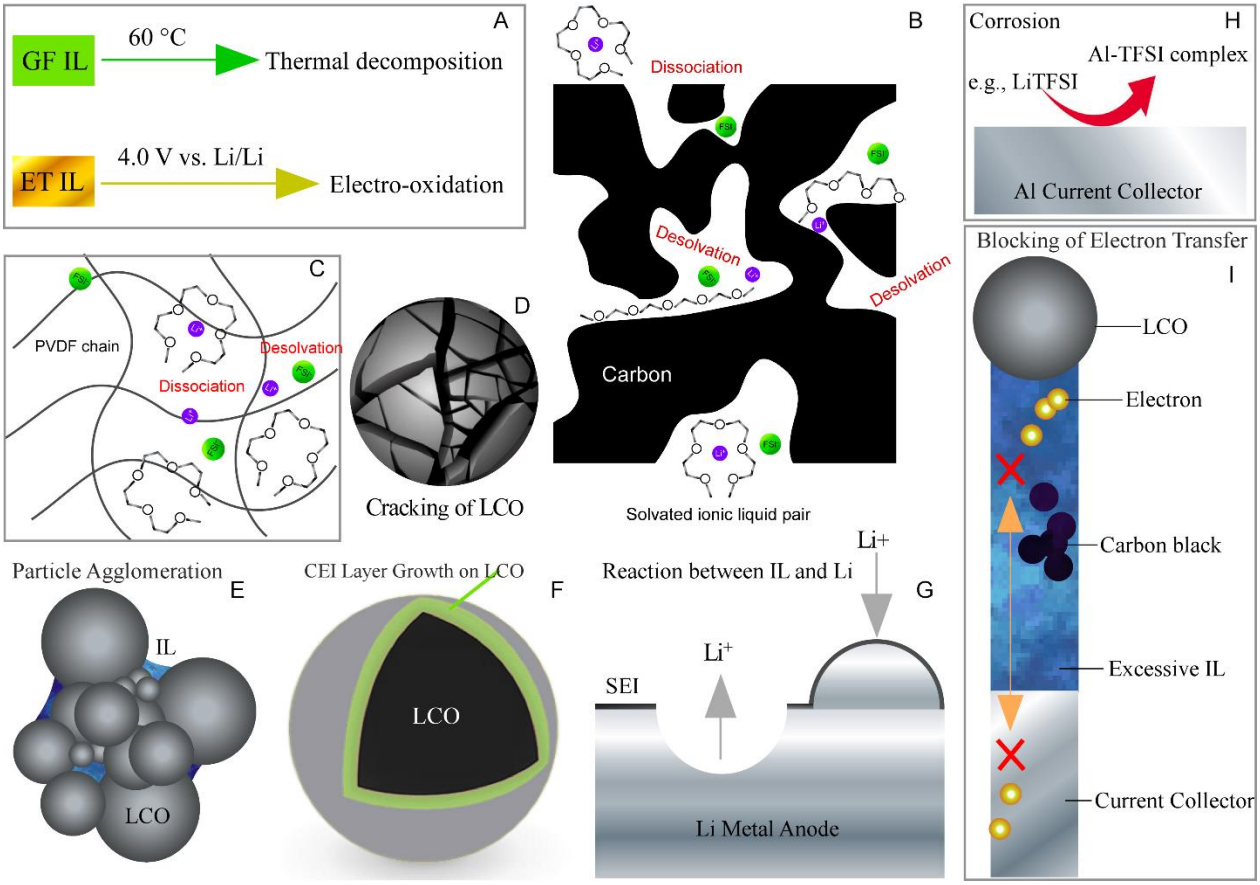

Figure 1.7 Illustration of the failure mechanisms of the quasi-solid-state Li/Al-LLZO/LCO cell. (a) Thermal decomposition or electron-oxidation of the ILs, (b) and (c) Dissociation or desolvation of GF in carbon black and PVDF binder, (d) Cracking of LCO caused by stress accumulation and fatigue, (e) Agglomeration of LCO (or AB) particles, (f) Growth of the CEI layer on LCO because of reactions between LCO and the IL, (g) Possible reaction between Li metal and the ILs, (h) Corrosion of Al current collector in the ILs and (i) Blocking of electron transport by excessive IL.

Thus, a quasi-solid-state and non-fluidic LCO composite cathode was developed, and the interfacial resistance between the quasi-solid-state LCO cathode and LLZO was less than 120 Ω cm^2. The optimal concentration of a conventional IL in the quasi-solid-state LCO was 11.3 wt% (27.1 vol%). The quasi-solid-state Li/Al-LLZO/LCO cell achieved relatively high capacity retention of about 80% after 100 cycles at 60 °C. The capacity decay was mainly due to the reactions between LCO and the IL as well as the decomposition of the IL.

1.6 All-Solid-State-Li Metal batteries

The large interfacial resistance between solid electrolytes and cathodes is the major challenge to overcome in developing all-solid-state Li-metal batteries. Introducing a small amount of liquid electrolyte to wet the solid electrolyte/electrode interface is a convenient and effective way to reduce the interfacial resistance [11]. Besides, polymer-in-LLZO flexible sheet electrolytes were also proposed to optimize the physical contact between solid electrolytes and cathodes [12]. Nevertheless, introducing a liquid electrolyte or applying a polymer-based flexible electrolyte to reduce the interfacial resistance will compromise battery safety. For example, the most widely used poly(ethylene oxide) solid-state polymer electrolyte (PEO) is readily flammable. In comparison, thermally soldering cathodes and solid electrolytes with a low-melting-point solid electrolyte was a relatively new approach to mitigating interfacial resistance [13].

Aerosol deposition (AD) is a room-temperature coating technology that deposits cathode films on ceramic electrolytes. An illustration of the aerosol deposition setup is shown in Figure 1.8**A**. Accelerated particles are cracked and deformed when hitting the ceramic substrate (Figures 1.8**B** and **C**) [14, 15]. The high surface energy generated from particle fracture or plastic deformation is likely to be the driving force for the densification of small particles at room temperature. However, ceramic-based all-solid-state Li metal batteries prepared by AD usually can hardly work and

degrade rapidly with cycling, most likely due to the high interfacial resistance and the degradation of the electrode-solid electrolyte interface. The stresses generated by the insertion and extraction of Li-ions into and out of the cathode materials can result in interfacial cracking. As a result, further interface engineering is needed to reduce the interfacial resistance and to maintain the integrity of the cathode-solid electrolyte interface prepared by AD. For example, the deposited cathode layer and the ceramic electrolyte can be joined together with a low-melting-point solid electrolyte at heating (Figure 1.8**D**), which has been pre-coated on the surface of the cathode material.

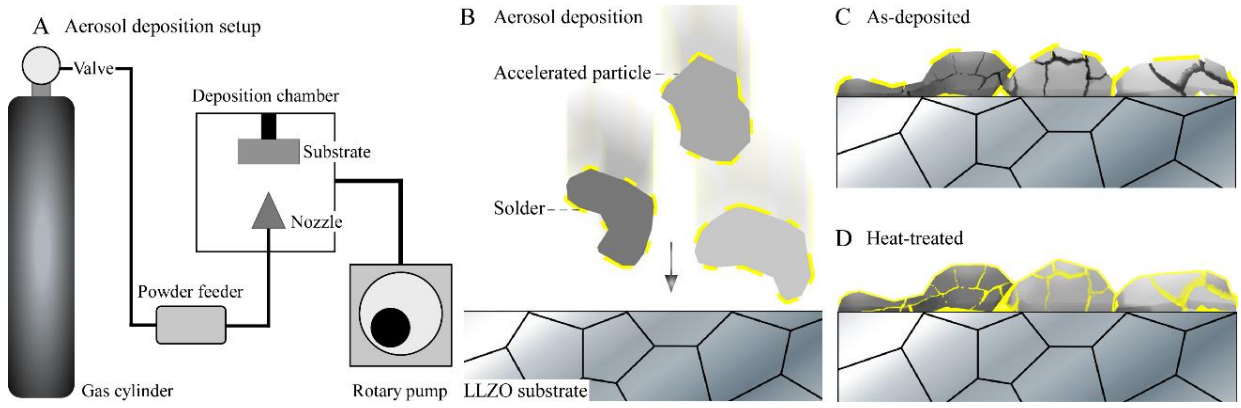

Figure 1.8 Illustration of the AD process. (**A**) Illustration of the AD setup, (**B**) Solder-coated cathode particles hitting onto an LLZO substrate, (**C**) As-deposited cathode layer, where the particles are cracked and deformed, (**D**) Heat-treated cathode layer, where a low-melting-point solder material upon heating fills the cracks and voids.

An SEM image of the pristine LCO powder synthesized by a sol-gel method is shown in Figure 1.9a. The particle size is in the range of 0.5-3.0 μm, and the surface is clean. The LBO coated the LCO particle (Figures 1.9b and c) through ball milling and heat treatment (800 °C). The mass ratio between LCO and LBO in the composite LCO-LBO cathode material is 7:3. The synthesized crystalline LBO became amorphous-like after ball milling.

The LBO-LCO powder was deposited onto a cubic LLZO substrate by AD at room temperature. The interfacial contact between LBO-LCO and LLZO was further improved following heat treatment at 750 °C for 1 h (Figure 1.9d). The thickness of the deposited composite cathode layer is generally in the range of 4 to 8 μm, while it is also possible to deposit much thicker cathode films (e.g., a 25 μm-thick film on LLZO by AD. Figures 1.9e and f show the energy-dispersive X-ray spectroscopy (EDS) mappings of oxygen and cobalt at the LBO-LCO|LLZO interface region, indicating good interfacial contact was achieved.

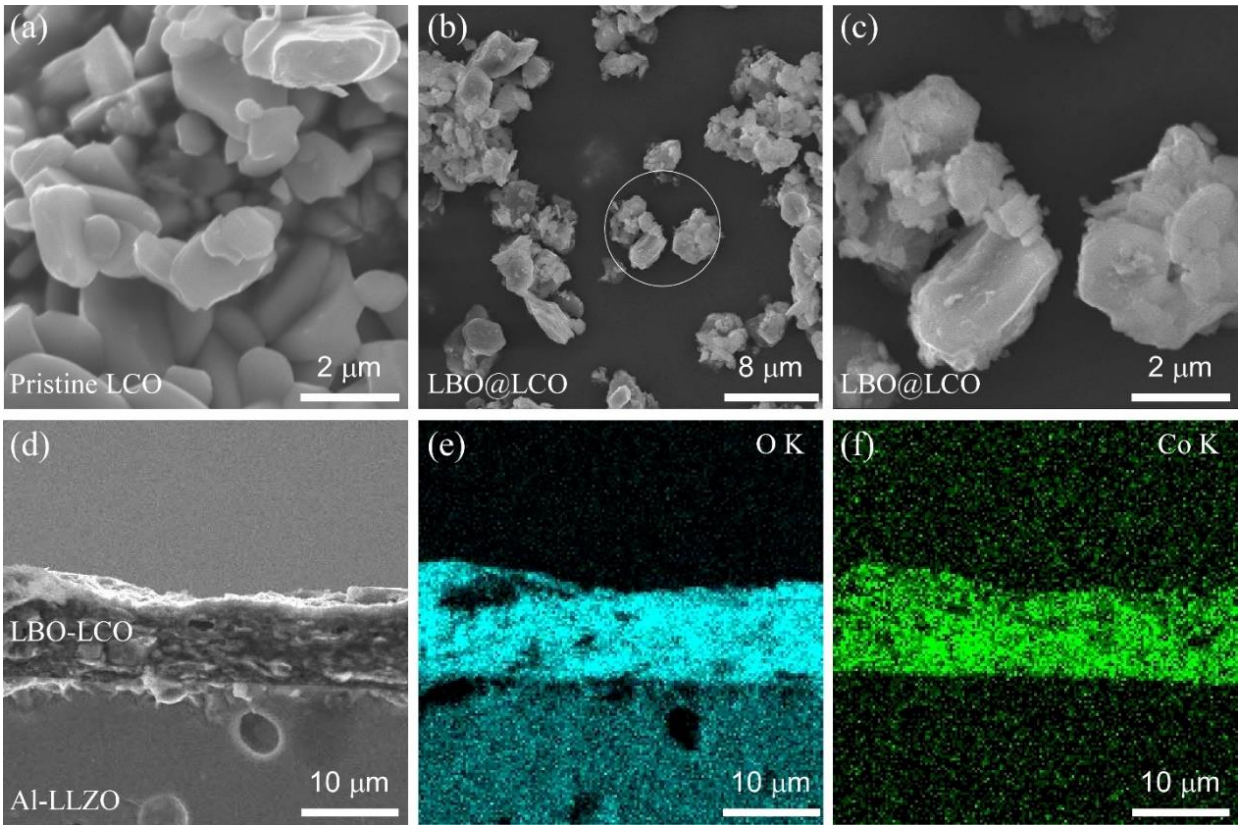

Figure 1.9 SEM micrographs of the LBO-LCO/LLZO interface. (a) As-synthesized LCO powder, (b) LBO-coated LCO powder, (c) High-resolution SEM image of the circled area in (b), (d) LBO-LCO cathode layer deposited on LLZO by AD at room temperature, following heat treatment at

750 °C for 1 h, (e) Element mapping of oxygen at the LBO-LCO/LLZO interface area, (f) Element mapping of cobalt at the LBO-LCO/LLZO interface area

In this study, I tried to engineer the interface between cathodes and the garnet-type LLZO solid electrolyte to reduce the interfacial resistance, which is the bottleneck for further improving the performance of solid-state Li metal batteries. As a result, I developed an ionic-liquid-containing quasi-solid-state LLZO-based flexible sheet electrolyte and an ionic-liquid-containing quasi-solid-state LCO cathode. I also deposited several cathode materials, such as Li-rich $Li_{1.2}Mn_{0.54}Ni_{0.13}Co_{0.13}O_2$, on the Al-LLZO ceramic electrolyte by aerosol deposition for making all-solid-state Li metal batteries. Some progress in reducing the interfacial resistance between the LLZO solid electrolyte and electrodes has been achieved.

Reference

[1] K. Subramanian, G. Alexander, K. Karthik, S. Patra, M. Indu, O. Sreejith, R.Viswanathan, J. Narayanasamy, R. Murugan, A brief review of recent advances in garnet structured solid electrolyte based lithium metal batteries. *Journal of Energy Storage* **33**, 102157 (2021).

[2] T. Thompson, J. Wolfenstine, J. Allen, M. Johannes, A. Huq, I. David, J. Sakamoto, Tetragonal vs. cubic phase stability in Al–free Ta doped $Li_7La_3Zr_2O_{12}$ (LLZO). *Journal of Materials Chemistry A* **2**, 13431-13436 (2014).

[3] J. Awaka, A. Takashima, K. Kataoka, N. Kijima, Y. Idemoto, J. Akimoto, Crystal structure of fast lithium-ion-conducting cubic $Li_7La_3Zr_2O_{12}$. *Chemistry letters* **40**, 60-62 (2011).

[4] C.A. Geiger, E. Alekseev, B. Lazic, M. Fisch, T. Armbruster, R. Langner, M. Fechtelkord, N. Kim, T. Pettke, W. Weppner, Crystal chemistry and stability of "Li7La3Zr2O12" garnet: a fast lithium-ion conductor, Inorganic chemistry 50(3) (2011) 1089-1097.

[5] M. Xu, M. S. Park, J. M. Lee, T. Y. Kim, Y. S. Park, E. Ma, Mechanisms of Li^+ transport in garnet-type cubic $Li_{3+x}La_3M_2O_{12}$ (M= Te, Nb, Zr). *Physical Review B* **85**, 052301 (2012).

[6] Y. Zhu, X. He, Y. Mo, Origin of outstanding stability in the lithium solid electrolyte materials: insights from thermodynamic analyses based on first-principles calculations. *ACS applied materials & interfaces* **7**, 23685-23693 (2015).

[7] M. Keller, G. Appetecchi, G. Kim, V. Sharova, M. Schneider, J. Schuhmacher, A. Roters, S. Passerini, Electrochemical performance of a solvent-free hybrid ceramic-polymer electrolyte based on $Li_7La_3Zr_2O_{12}$ in $P(EO)_{15}$LiTFSI. *Journal of Power Sources* **353**, 287-297 (2017).

[8] L. Chen, Y. Li, S. Li, L. Fan, C. Nan, J. B. Goodenough, PEO/garnet composite electrolytes for solid-state lithium batteries: From "ceramic-in-polymer" to "polymer-in-ceramic". *Nano Energy* **46**, 176-184 (2018).

[9] J. L. Vigneresse, P. Barbey, M. Cuney, Rheological transitions during partial melting and crystallization with application to felsic magma segregation and transfer. *Journal of Petrology* **37**, 1579-1600 (1996).

[10] S. Sugata, N. Saito, A. Watanabe, K. Watanabe, J.-D. Kim, K. Kitagawa, Y. Suzuki, I. Honma, Quasi-solid-state lithium batteries using bulk-size transparent $Li_7La_3Zr_2O_{12}$ electrolytes. *Solid State Ionics* **319**, 285-290 (2018).

[11] C. Zhao, B. Zhao, C. Yan, X. Zhang, J. Huang, Y. Mo, X. Xu, H. Li, and Q. Zhang, Liquid phase therapy to solid electrolyte–electrode interface in solid-state Li metal batteries: a review. *Energy Storage Materials* **24,** 75-84 (2020).

[12] L. Chen, Y. Li, C. Nan, J. Goodenough, PEO/garnet composite electrolytes for solid-state lithium batteries: From "ceramic-in-polymer" to "polymer-in-ceramic", Nano Energy **46**, 176-184 (2018)

[13] Fudong Han, Jie Yue, Cheng Chen, Ning Zhao, Xiulin Fan, Zhaohui Ma, Tao Gao, Fei Wang, Xiangxin Guo, Chunsheng Wang, Interphase Engineering Enabled All-Ceramic Lithium Battery, Joule **2**, 497-508 (2018)

[14] Jun Akedo, Aerosol Deposition of Ceramic Thick Films at Room Temperature: Densification Mechanism of Ceramic Layers, Journal of the American Ceramic Society **89**, 1384-1839 (2006)

[15] Miyuki Sakakura, Yasuhiro Suzuki, Takayuki Yamamoto, Yuta Yamamoto, Munekazu Motoyama, and Yasutoshi Iriyama, Low-Resistive $LiCoO_2/Li_{1.3}Al_{0.3}Ti_2(PO_4)_3$ Interface

Formation by Low-Temperature Annealing Using Aerosol Deposition, Energy Technology 9, 2001059 (2021)

Chapter 2 Preparation of garnet-based flexible sheet electrolyte

2.1 Abstract

The increasing demand for high-energy-density batteries stimulated the renaissance of research interest in Li metal batteries. The garnet-type ceramic $Li_7La_3Zr_2O_{12}$ (LLZO) is one of the few solid-state fast ion conductors that are stable against Li metal. However, densification of LLZO powders usually requires high sintering temperatures (e.g., 1200 ℃), which likely results in Li loss and various side reactions. From an engineering point of view, high-temperature sintering of thin LLZO electrolytes (brittle) on a large scale is difficult. Moreover, the high interfacial resistance between the solid LLZO electrolytes and electrodes is a notorious problem. Here we report a practical synthesis of a flexible composite Al-doped LLZO (Al-LLZO) sheet electrolyte (75 μm in thickness), which can be mass-produced at room temperature. This ceramic-based flexible sheet electrolyte enables Li metal batteries to operate at 60 ℃ and 30 ℃, demonstrating its potential for developing practical Li metal batteries.

2.2 Introduction

Sustainable energies, such as wind and solar energy, must be further explored to resolve the conflict between the growing global energy demands and the depleting fossil fuels [1]. Meanwhile, increasing concerns on environmental pollution propel the development of electric vehicles (EVs). Advanced energy storage systems are the key to effectively using renewable but intermittent energy resources for grid storage and EVs. Though Li-ion batteries have profoundly impacted modern society since their first commercialization by Sony in 1991 [2], EVs with a range of 800 km or more still require substantial improvements in capacity, cyclability, and safety of the state-of-the-art Li-ion technology [3]. This led to the renaissance of research on Li metal batteries because

metallic Li has an ultrahigh theoretical specific capacity of 3860 mA h g^{-1} and the lowest redox potential of -3.04 V vs. standard hydrogen electrode [4]. In contrast, the widely used graphite anode has only about one-tenth the capacity of Li metal (372 mA h g^{-1}). However, the utilization of Li metal anode is problematic in liquid-based batteries due to the inhomogeneous deposition of Li metal [5]. Inorganic solid-state electrolytes can stabilize the Li-electrolyte interface and reduce the risk of fires and explosions from flammable liquid electrolytes [6-10]. Compared with sulfides (e.g., Li_2S-P_2S_5 and $Li_{10}GeP_2S_{12}$), ceramic oxides (e.g., (La, Li)NbO_3) and $Li_{1.3}Al_{0.3}Ti_{1.7}(PO_4)_3$) are generally more stable against ambient air and thus can be more easily handled during processing [9, 11-14]. In particular, the garnet-type LLZO has attracted tremendous interest as a promising solid electrolyte due to its high ionic conductivity (about 10^{-3} S cm^{-1} at 25 ºC) and high chemical stability against metallic Li [15-20].

However, high-temperature sintering (e.g., 1200 ℃), which is very energy inefficient and time-consuming, is generally necessary to densify LLZO powders [21-23]. Meanwhile, Li loss and side reactions are likely to occur at high temperatures. Therefore, considerable efforts have been put into lowering the sintering temperature of LLZO powders. For example, a dense LLZO-Li_3BO_3 composite was prepared at 900 ℃ with Li_3BO_3 as a sintering aid [24]. Using Li_3N as a Li source for compensation, cubic LLZO was synthesized at 660 ℃ using a pulsed laser deposition technique [25]. Nevertheless, from an engineering point of view, high-temperature sintering for large-scale production of LLZO membranes is very difficult.

Besides the high sintering temperature, the poor physical contact between LLZO pellets and cathode materials usually results in high interfacial resistance [26]. To solve this issue, co-sintering of cathode materials, e.g., $LiCoO_2$ (LCO) and LLZO powders, was proposed [27]. However, LCO would decompose at a sintering temperature higher than 900 ℃ [28]. Therefore, IL-contained

quasi-solid-state electrolytes were explored, where the interfacial resistance was substantially reduced by introducing a small amount of IL [29-30]. ILs are generally supposed to be thermally stable, almost non-volatile, and non-flammable [31]. For example, an IL of N-butyl-N-methylpyrrolidinium bis(trifluoromethanesulfonyl)imide (Py_{14}TFSI), a Li salt of lithium bis(trifluoromethanesulfonyl)imide (LiTFSI), and an LLZO powder (w:w:w=19:1:80) were ball-mixed and cold pressed, forming a highly conductive quasi-solid-state electrolyte [29]. However, the cold-pressed quasi-solid-state LLZO pellets are still brittle and unsuitable for mass production. Alternatively, LLZO particles have been integrated into LiTFSI-containing polyethylene oxide (PEO) polymers to form flexible composite sheet electrolytes, which are not only flexible and easy to handle but also capable of self-healing. Yet the PEO-based flexible electrolytes usually suffer from poor ionic conductivity ($<1.0 \times 10^{-5}$ S cm^{-1} at 25 ℃) and low oxidation stability [32]. A question arises, can we produce a flexible and highly conductive LLZO sheet electrolyte at room temperature?

Here we report a room-temperature synthesis of a flexible composite Al-LLZO sheet electrolyte by tape-casting and IL-impregnation (IL: Li(G4)FSI, a lithium bis(fluorosulfonyl)imide (LiFSI) and tetraglyme (G4) equimolar complex, regarded as a solvate IL [31]; G4 is less costly in comparison to conventional ILs, e.g., 1-ethyl-3-methylimidazolium-bis(trifluoromethylsulfonyl)imide (EMI-TFSI)). ILs are not only capable of bridging the LLZO particles, forming an efficient Li^+ pathway, but could also wet the solid electrolyte/electrode interface (as illustrated in Figure 1(a)), effectively reducing the interfacial resistance. The synthesized sheet electrolyte is flexible, mechanically robust, and highly conductive (close to 1.0×10^{-4} S cm^{-1} at 25 ℃). Moreover, room-temperature synthesis is simple and suitable for industrial production. Composite Li/AL-LLZO sheet/LCO cells can deliver an initial discharge capacity of

139 mAh g^{-1} at 0.1 C and 60 ℃. In addition, the cells can also work at 30 ℃ and deliver an initial discharge capacity of about 110 mAh g^{-1} at 0.1 C. These results demonstrated the potential of the flexible sheet electrolyte for developing practical Li metal batteries.

2.3 Experiment

2.3.1 Casting of flexible Al-LLZO sheet electrolytes

An Al-LLZO powder (D50 = 10 μm, Daiichi Kigenso Kagaku Kogyo Co., Ltd., Japan) and a polystyrene-type elastomeric binder (Chukyo Yushi Co., Ltd., Japan) (w:w = 20:1) were mixed in toluene (Wako Pure Chemical Corp., Japan). The mixture was ball-mixed (ZrO_2 ball, 5 mm in diameter) with a planetary centrifugal vacuum mixer (ARV-310, Thinky, Japan) at 2000 rpm for 15 min. The formed slurry was cast onto a polyethylene terephthalate (PET) substrate (75 μm in thickness) using a doctor blade. Though the polystyrene-type binder is a Li-ion insulator, it has a high binding affinity to ceramics. Its relatively slow solidification rate makes it suitable for forming a stable LLZO slurry for tape casting at room temperature. The as-cast sheet was dried at 25 ℃ for 8 h in a vacuum.

2.3.2 Cold isostatic pressing and IL-impregnation processes

Circular samples were punched from the dried sheet and were cold isostatically pressed (CIP) at 150 MPa for 5 min. After Au-coating (ion current: 3.5 mA; sputtering time: 1 h for one side), the circular samples were immersed in a solvate IL of Li(G4)FSI for 8 h in an Ar-filled glove box. The sample surface was dried with glass filter papers, and the weight percentage of the IL absorbed was about 10.2 wt% (about 26.1 vol%).

2.3.3 Preparation of IL-containing composite LCO cathode

LCO powder, acetylene black (AB), and polyvinylidene difluoride (PVDF) (w:w:w=92:4:4) were ball-mixed in N-methyl-2-pyrrolidone (NMP), and the slurry was cast onto an Al foil (20 μm thick). The composite cathode layer was dried at 80 ℃ in a vacuum for 8 h and then immersed in the IL (Li(G4)FSI) for 8 h in an Ar atmosphere.

2.3.4 Materials characterization

Scanning electron microscopy was conducted on a JSM-6490A SEM. Liquid nuclear magnetic resonance (NMR) spectroscopy (^{7}Li NMR, JEOL ECS-300, Japan) was used to determine the interaction between the IL and Al-LLZO. Differential scanning calorimetric (DSC) analysis was performed using a thermal analyzer (TA-60 WS, Shimadzu, Japan) from -80 ℃ to 80 ℃ at a scanning rate of 2 ℃ min^{-1}. The thermal stability of the sheet electrolyte was investigated using the thermogravimetric analysis technique (TG, DTG-60 H, SHIMADZU, Japan) between 30 ℃ and 250 ℃ with a heating rate of 5 ℃ min^{-1}. The total ionic conductivity of the composite sheet electrolyte was measured by electrochemical impedance spectroscopy (EIS) (5 MHz to 0.1 Hz, 10 mV amplitude; Biologic SP-300 Potentiostat, France) in the temperature range of 25 to 80 ℃.

2.3.5 Cell fabrication

CR-2032 coin cells were assembled with the composite LCO layers (8 mm in diameter and ～ 35 μm thick in thickness; LCO loading: ~7 mg cm^{-2}), the flexible composite Al-LLZO sheets (16 mm in diameter) or Al-LLZO pellets (15 mm in diameter and with the anode side Au-coated), and Li foils (10 mm in diameter and 25 μm in thickness) in an Ar-filled glove box. The assembled cells were heat-treated at 60 ℃ for 12 h in that the Au layer deposited on the LLZO surface would form

an Au-Li alloy with the Li metal anode, and good contact between the Al-LLZO pellet and the Li metal anode was expected [33]. For the case of the flexible composite Al-LLZO sheet, it was relatively easy to form good physical contact with the Li metal anode upon pressure. Also, IL could be squeezed out from the flexible composite sheet electrolyte to wet the interface between the Li metal anode (or the LCO cathode) and the flexible composite sheet electrolyte. Galvanostatic cycling was performed at 30 ℃ and 60 ℃, respectively, with a C-rate of 0.1 C in the voltage range of 2.5-4.2 V.

2.4 Results and Discussion

2.4.1 Concept and optical image of the sheet electrolyte

The doctor-blade casting of the Al-LLZO sheet electrolyte in ambient air is shown in Fig. 2.1(b). The as-cast sheet (about 100 μm thick) can be easily removed from the PET substrate after drying (Fig. 2.1(c)). Although the volume fractions of the Al-LLZO particle in the as-cast ((Fig. 2.1(c)) and the IL-impregnated ((Fig. 2.1(d)) sheets are as high as about 80 % and 60 %, respectively, both sheets show good flexibility and high mechanical stability. In addition, different from sulfide electrolytes, this flexible Al-LLZO sheet electrolyte is easy to handle in ambient air.

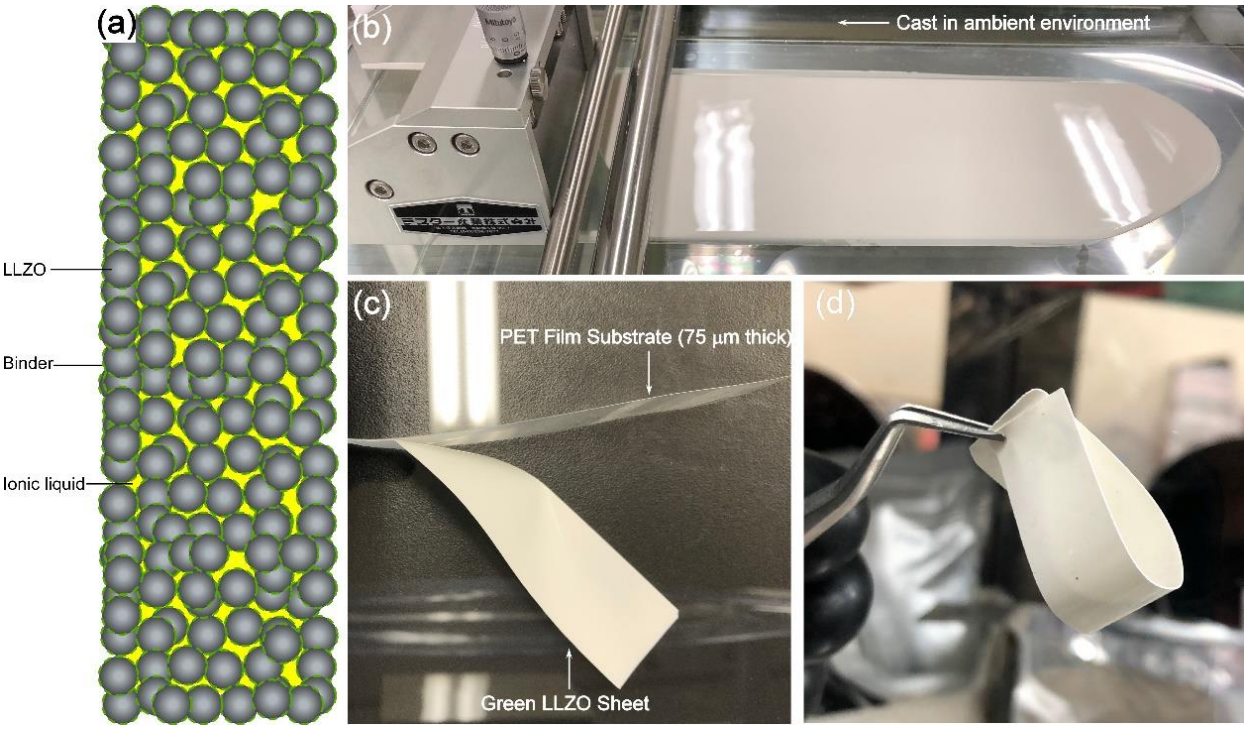

Fig. 2.1 Concept of the flexible composite Al-LLZO sheet electrolyte and its synthesis at room temperature. (a) illustration of the composite sheet electrolyte, (b) doctor-blade casting of the sheet electrolyte in ambient air, (c) as-cast green sheet, (d) cold-pressed and IL-impregnated Al-LLZO sheet electrolyte

2.4.2 Microstructure of the sheet electrolyte

A cross-sectional SEM micrograph of the as-cast Al-LLZO sheet electrolyte is shown in Fig. 2.2(a), where Al-LLZO particles are bound together, forming a sponge-like structure. Nano-sized pores are observed among primary Al-LLZO particles, while micro-sized pores are observed among secondary particles (Fig. 2.2(b)). The porosity of the as-cast sheet electrolyte was estimated to be 50%, based on the densities of the polystyrene-type binder and Al-LLZO. After cold-pressing at 150 MPa for 5 min, the thickness of the sheet electrolyte decreased to about 75 μm (Fig. 2.2(c)), and the porosity decreased from 50% to 35%, correspondingly (Fig. 2.2(d)). EDS element mapping

of La (Fig. 2.2(c)) indicates a uniform distribution of the Al-LLZO particle in the sheet electrolyte. On the one hand, denser solid electrolytes usually have higher ionic conductivities; conversely, a more porous sheet can absorb more IL, increasing its ionic conductivity. Thus, a systematic study is needed to find a balance between the porosity, the ionic conductivity, and the cost of the flexible composite sheet electrolyte.

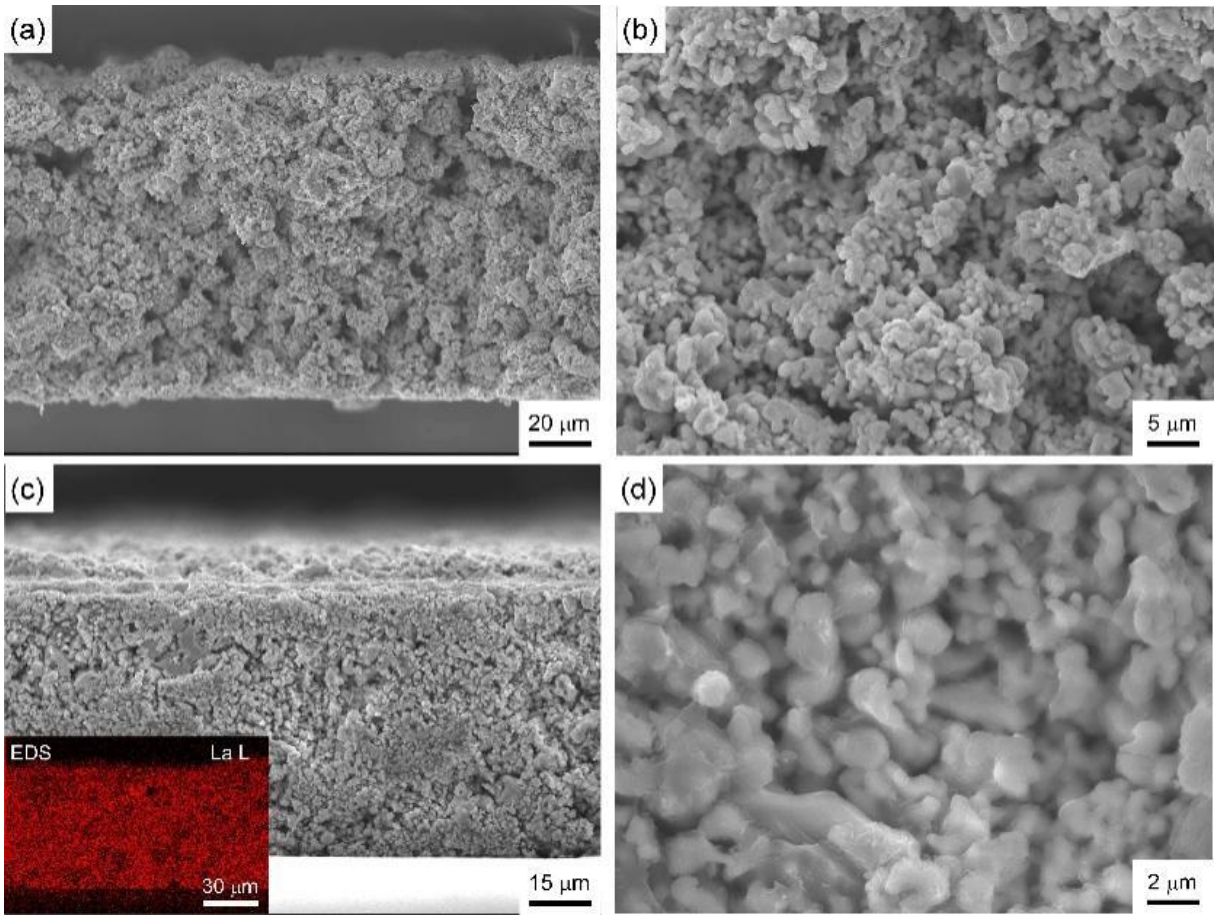

Fig. 2.2 SEM micrographs of as-cast and cold-pressed Al-LLZO sheet electrolytes. (a) cross-section of the as-cast sheet electrolyte, (b) enlarged view of part of the cross-section shown in (a), (c) cross-section of a 150 MPa cold-pressed sheet (inset: EDS mapping of La), (d) enlarged view of part of the cross-section shown in (c)

2.4.3 Interactions between Al-LLZO and IL

Interactions between the IL and Al-LLZO particles were expected in the IL-impregnated Al-LLZO sheet electrolyte. To prove this claim, NMR and DSC analyses were carried out. As shown in Fig. 2.3(a), the ^{7}Li peak of the IL in the sheet electrolyte significantly broadened, and the peak position also slightly shifted to a higher magnetic field. This could be attributed to the strong interactions of the Li^{+} in the IL and Al-LLZO [34], indicating the formation of an IL/Al-LLZO composite material. Similarly, as shown in Fig. 2.3(b), the DSC endothermic peak of the IL in the sheet electrolyte shifted about 2.5 ℃ toward higher temperature, further proving the interactions between the IL and the Al-LLZO particles. Besides, to study the thermal stability of the composite sheet electrolyte, TG analysis was performed in air and N_2, respectively (Fig. 2.3(c)). A slight weight loss (about 1.5%) occurred at 46 ℃, possibly

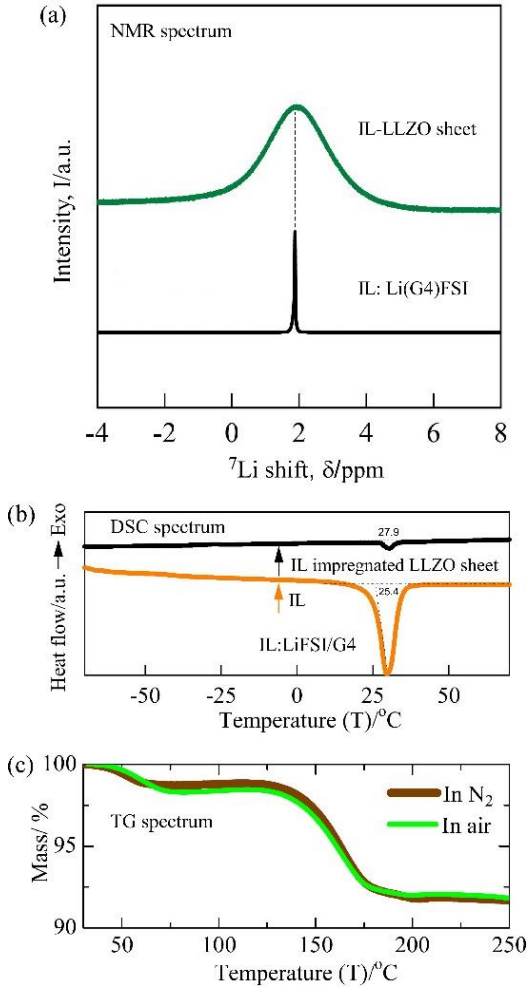

Fig. 2.3 Analysis of the interaction between the IL and the Al-LLZO particle in the sheet electrolyte. (a) NMR spectra of the IL and the IL impregnated in the Al-LLZO sheet, (b) DSC spectra of the IL and the IL impregnated in the Al-LLZO sheet, (c) TG spectra of the IL-impregnated Al-LLZO sheet in both air and N_2

corresponding to the evaporation of the residual toluene. The composite sheet electrolyte was thermally stable up to 142 ℃, where a sudden weight loss (about 6.5%) occurred, most likely due to the decomposition of the IL [35].

2.4.4 Electrochemical performance of the sheet electrolyte

The impedance (R) of the composite sheet electrolyte was measured using EIS, and the total ionic conductivity σ is determined using the following equation (Eq. (2.1)),

$$\sigma = \frac{L}{RA} \qquad (2.1)$$

where L is the thickness of the sheet electrolyte, and A is the active electrode area. The ionic conductivity of the as-cast Al-LLZO green sheet was only about 2.0×10^{-9} S cm^{-1} at 60 ℃ because the interfacial resistance was as high as about 1.0×10^{7} Ω (Fig. 2.4(a)). In contrast, the ionic conductivity of the IL-impregnated sheet electrolyte reached 7.1×10^{-5} S cm^{-1} at 25 ℃ (Fig. 2.4(b)), indicating that the IL filled the pores and connected the LLZO particles, forming an efficient Li^+ pathway in the sheet electrolyte. Since the green sheet was cast in ambient air, common LLZO surface contaminants, i.e., Li_2CO_3 and LiOH, would decrease its ionic conductivity and increase the interfacial resistance [36]. Thus, the ionic conductivity of the composite sheet electrolyte would be expected to improve by optimizing the processing conditions, such as casting the green sheet in Ar or removing the surface contaminants by acid etching [37]. In addition, impregnating the sheet

with highly conductive ILs would increase its ionic conductivity. In comparison, the ionic conductivity of the hot-pressed flexible LLZO/PEO/LiTFSI hybrid electrolyte was only about 1.0 × 10^{-5} S cm^{-1} at 25 ℃ [32].

The temperature dependence of the ionic conductivities of the flexible composite sheet electrolyte, the IL, and a 1200 ℃-sintered Al-LLZO pellet was fitted with the Arrhenius equation (Eq. (2.2)):

$$\sigma(T) = \sigma_0 \exp[-E_a/(k_B T)] \qquad (2.2)$$

where σ is the ionic conductivity, σ_0 is the pre-exponential factor (a constant with the same unit as σ), T is the absolute temperature, E_a is the activation energy, and k_B is the Boltzmann constant. The activation energies of the composite sheet electrolyte, the IL, and the 1200 ℃-sintered Al-LLZO pellet were estimated to be 0.24 eV, 0.31 eV, and 0.26 eV, respectively (Fig. 2.4(c) and Table 2.1). The composite sheet electrolyte has lower activation energy than its two ionically conductive components (the elastomeric binder is ionically insulating). Thus Li^+ ions are supposed to diffuse through the Al-LLZO particles and the IL for transport in the composite sheet electrolyte, as illustrated in Fig. 2.4(d), and a highly conductive layer (SEI layer) could be formed between the Al-LLZO particles and the IL.

Additionally, according to the percolation theory [38], when the volume fraction of the particles reaches about 70% (particle locking threshold), the solid-liquid system becomes totally locked, and the liquid phase becomes discontinuous and unable to flow (the volume fracture of the IL is about 26% in the composite sheet electrolyte). Thus, the Li^+ must diffuse through the IL and the Al-LLZO particles for migration. Though the high ionic conductivity of the composite sheet electrolyte could be mainly attributed to the IL, the Al-LLZO particles act as an ionically conductive matrix to hold

the IL.

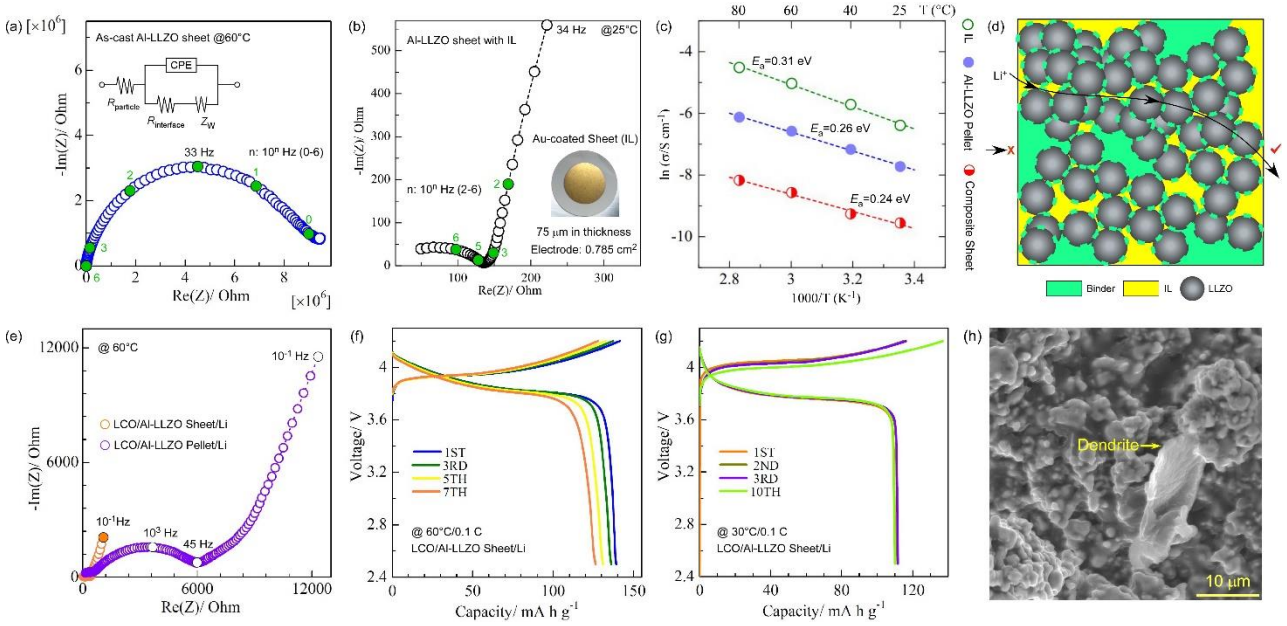

Fig. 2.4 Electrochemical evaluation of the flexible composite sheet electrolyte. (a) EIS spectrum of the as-cast Al-LLZO green sheet at 60 ℃ (inset: equivalent circuit), (b) EIS spectrum of the IL-impregnated composite Al-LLZO sheet electrolyte, (c) temperature dependence of the total ionic conductivities of the IL, a 1200 ℃-sintered Al-LLZO pellet (relative density: 95%), and the flexible composite sheet electrolyte, (d) illustration of the Li-ion pathway in the flexible composite sheet electrolyte, (e) EIS spectra of a composite LCO/composite Al-LLZO sheet/Li cell and an LCO (without IL)/Al-LLZO pellet/Li cell at 60 ℃, (f) cycling profile of the composite LCO/composite Al-LLZO sheet/Li cell at 60 ℃, (g) cycling profile of the composite LCO/composite Al-LLZO sheet/Li cell at 30 ℃, (h) SEM micrograph of the fracture surface of the cycled flexible composite Al-LLZO sheet

Table 2.1 Measured ionic conductivities σ and activation energies E_a of the IL, the 1200 ℃-sintered Al-LLZO pellet, and the flexible composite sheet electrolyte

σ (10^{-4} S cm^{-1})	25 ℃	40 ℃	60 ℃	80 ℃	E_a (eV)
IL: Li(G4)FSI	16.79	33.09	65.44	109.56	0.31
Al-LLZO Pellet	4.41	7.70	13.88	21.84	0.26
Composite Sheet	0.71	0.95	1.90	2.82	0.24

The effect of the IL in reducing the interfacial resistance between the sheet electrolyte and the LCO cathode was investigated. The total resistance of the two cells, i.e., composite LCO/composite Al-LLZO sheet/Li and LCO (without IL)/Al-LLZO pellet/Li, were 400 Ω and 8000 Ω, respectively, at 60 ℃ (Fig. 2.4(e)). It should be noted that the total resistance of the Li/Al-LLZO pellet/Li symmetric cell was only about tens to hundreds of ohms at 60 ℃. Thus, the introduction of the IL effectively reduced the cathode interfacial resistance. In addition, the LCO/Al-LLZO pellet/Li cell could not be cycled, while the composite LCO/composite Al-LLZO sheet/Li cell could be reversibly cycled and delivered an initial discharge capacity of 139 mAh g^{-1} at 0.1 C and 60 ℃ (Fig. 2.4(f)). The cell could also work at 30 ℃ and deliver a discharge capacity of around 110 mAh g^{-1} at 0.1 (Fig. 2.4(g)). Though the discharge capacity decreased with cycling, these results demonstrated the potential of the flexible composite Al-LLZO sheet electrolyte for use in Li metal batteries. As shown in Fig. 2.4(h), Li dendrite was observed on the fracture surface of the cycled flexible composite sheet electrolyte, indicating that the mechanical stiffness of the flexible sheet electrolyte was inadequate to sustain the high-stress build-up during Li dendrite growth [39-40].

The formation of electrically isolated Li dendrites and possible side reactions could be the main reasons for the capacity fading. Further work needs to be done to elucidate the mechanism.

2.5 Conclusions

In summary, a 75 μm-thick flexible composite Al-LLZO sheet electrolyte with an ionic conductivity of close to 1.0×10^{-4} S cm^{-1} at 25 ℃ was prepared by tape casting and IL-impregnation at room temperature. The IL connected the Al-LLZO particles, forming an efficient Li-ion pathway, effectively reducing the cathode interfacial resistance. There is still a large space to improve the ionic conductivity of the flexible sheet electrolyte, e.g., impregnating the sheet electrolyte with highly conductive ILs or casting it in Ar or a dry room. The synthesis is simple and suitable for industrial production. The Li/Al-LLZO sheet/LCO cell could be reversibly cycled at both 30 ℃ and 60 ℃, demonstrating the potential of the flexible composite Al-LLZO sheet electrolyte for developing practical Li metal batteries. However, the cyclability of the ceramic-based flexible sheet electrolyte has to be improved first.

Reference

[1] Larcher, D.; Tarascon, J.-M. Towards Greener and More Sustainable Batteries for Electrical Energy Storage. *Nature Chemistry* **2015,** *7* (1), 19-29.

[2] Yoshino, A. The Birth of the Lithium-Ion Battery. *Angewandte Chemie International Edition* **2012,** *51* (24), 5798-5800.

[3] Van Noorden, R. The Rechargeable Revolution: A Better Battery. *Nature News* **2014,** *507* (7490), 26-28.

[4] Liu, J.; Bao, Z.; Cui, Y.; Dufek, E. J.; Goodenough, J. B.; Khalifah, P.; Li, Q.; Liaw, B. Y.; Liu, P.; Manthiram, A. Pathways for Practical High-Energy Long-Cycling Lithium Metal Batteries. *Nat. Energy* **2019**, 4, 180-186

[5] Famprikis, T.; Canepa, P.; Dawson, J. A.; Islam, M. S.; Masquelier, C. Fundamentals of Inorganic Solid-State Electrolytes for Batteries. *Nature Materials* **2019**,18, 1278-1291

[6] Taylor, N. J.; Stangeland-Molo, S.; Haslam, C. G.; Sharafi, A.; Thompson, T.; Wang, M.; Garcia-Mendez, R.; Sakamoto, J. Demonstration of High Current Densities and Extended Cycling in the Garnet $Li_7La_3Zr_2O_{12}$ Solid Electrolyte. *J. Power Sources* **2018,** *396*, 314-318.

[7] Duan, H.; Fan, M.; Chen, W. P.; Li, J. Y.; Wang, P. F.; Wang, W. P.; Shi, J. L.; Yin, Y. X.; Wan, L. J.; Guo, Y. G. Extended Electrochemical Window of Solid Electrolytes via Heterogeneous Multilayered Structure for High-Voltage Lithium Metal Batteries. *Advanced Materials* **2019,** *31* (12), 1807789-107795.

[8] Shoji, M.; Cheng, E. J.; Kimura, T.; Kanamura, K. Recent Progress for All Solid State Battery Using Sulfide and Oxide Solid Electrolytes. *Journal of Physics D: Applied Physics* **2019,** *52* (10), 103001

[9] Kamaya, N.; Homma, K.; Yamakawa, Y.; Hirayama, M.; Kanno, R.; Yonemura, M.; Kamiyama, T.; Kato, Y.; Hama, S.; Kawamoto, K.; Mitsui, A. A lithium Superionic Conductor. *Nature Materials* **2011,** *10* (9), 682-686

[10] Zheng, H.; Wu, S.; Tian, R.; Xu, Z.; Zhu, H.; Duan, H.; Liu, H. Intrinsic Lithiophilicity of Li-Garnet Electrolytes Enabling High-Rate Lithium Cycling. *Advanced Functional Materials*, **2019**, (1906189), DOI: 10.1002/adfm.201906189.

[11] Kawahara, K.; Ishikawa, R.; Nakayama, K.; Higashi, T.; Kimura, T.; Ikuhara, Y. H.; Shibata, N.; Ikuhara, Y. Fast Li-Ion Conduction at Grain Boundaries in (La, Li)NbO_3 Polycrystals. *J. Power Sources* **2019,** *441*, 227187-227193

[12] Ren, Y.; Chen, K.; Chen, R.; Liu, T.; Zhang, Y.; Nan, C. W. Oxide Electrolytes for Lithium Batteries. *J. Am. Ceram. Soc.* **2015,** *98* (12), 3603-3623.

[13] Seino, Y.; Ota, T.; Takada, K.; Hayashi, A.; Tatsumisago, M. A Sulphide Lithium Super Ion Conductor Is Superior to Liquid Ion Conductors for Use in Rechargeable Batteries. *Energy & Environmental Science* **2014,** *7* (2), 627-631.

[14] Ma, F.; Zhao, E.; Zhu, S.; Yan, W.; Sun, D.; Jin, Y.; Nan, C. Preparation and Evaluation of High Lithium Ion Conductivity $Li_{1.3}Al_{0.3}Ti_{1.7}(PO_4)_3$ Solid Electrolyte Obtained Using a New Solution Method. *Solid State Ionics* **2016,** *295*, 7-12.

[15] Zhang, J.; Zang, X.; Wen, H.; Dong, T.; Chai, J.; Li, Y.; Chen, B.; Zhao, J.; Dong, S.; Ma, J. High-Voltage and Free-Standing Poly(Propylene Carbonate)/$Li_{6.75}La_3Zr_{1.75}Ta_{0.25}O_{12}$ Composite Solid Electrolyte for Wide Temperature Range and Flexible Solid Lithium Ion Battery. *J. Mater. Chem. A* **2017,** *5* (10), 4940-4948.

[16] Murugan, R.; Thangadurai, V.; Weppner, W. Fast Lithium Ion Conduction in Garnet-Type $Li_7La_3Zr_2O_{12}$. *Angewandte Chemie International Edition* **2007,** *46* (41), 7778-7781.

[17] Duan, H.; Yin, Y.X.; Shi, Y.; Wang, P.F.; Zhang, X.D.; Yang, C.P.; Shi, J.L.; Wen, R.; Guo, Y.G.; Wan, L.J. Dendrite-Free Li-metal Battery Enabled by a Thin Asymmetric Solid Electrolyte with Engineered Layers. *Journal of the American Chemical Society* **2017,** *140* (1), 82-85.

[18] Han, F.; Yue, J.; Chen, C.; Zhao, N.; Fan, X.; Ma, Z.; Gao, T.; Wang, F.; Guo, X.; Wang, C. Interphase Engineering Enabled All-Ceramic Lithium Battery. *Joule* **2018,** *2* (3), 497-508.

[19] Kotobuki, M.; Munakata, H.; Kanamura, K.; Sato, Y.; Yoshida, T. Compatibility of $Li_7La_3Zr_2O_{12}$ Solid Electrolyte to All-Solid-State Battery Using Li Metal Anode. *J. Electrochem. Soc.* **2010,** *157* (10), A1076-A1079.

[20] Kataoka, K. Oxide Single Crystals with High Lithium-Ion Conductivity as Solid Electrolytes for All-Solid-State Lithium Secondary Battery Applications. *Journal of the Ceramic Society of Japan* **2020,** *128* (1), 7-18.

[21] Kim, Y.; Jo, H.; Allen, J. L.; Choe, H.; Wolfenstine, J.; Sakamoto, J. The Effect of Relative Density on the Mechanical Properties of Hot-Pressed Cubic $Li_7La_3Zr_2O_{12}$. *J. Am. Ceram. Soc.* **2016,** *99* (4), 1367-1374.

[22] Yamada, H.; Ito, T.; Basappa, R. H. Sintering Mechanisms of High-Performance Garnet-Type Solid Electrolyte Densified by Spark Plasma Sintering. *Electrochim. Acta* **2016,** *222*, 648-656.

[23] Inada, R.; Yasuda, S.; Hosokawa, H.; Saito, M.; Tojo, T.; Sakurai, Y. Formation and Stability of Interface between Garnet-Type Ta-Doped $Li_7La_3Zr_2O_{12}$ Solid Electrolyte and Lithium Metal Electrode. *Batteries* **2018,** *4* (2), 26-37

[24] Tadanaga, K.; Takano, R.; Ichinose, T.; Mori, S.; Hayashi, A.; Tatsumisago, M. Low Temperature Synthesis of Highly Ion Conductive $Li_7La_3Zr_2O_{12}$–Li_3BO_3 Composites. *Electrochemistry Communications* **2013,** *33*, 51-54.

[25] Pfenninger, R.; Struzik, M.; Garbayo, I.; Stilp, E.; Rupp, J. L. A low Ride on Processing Temperature for Fast Lithium Conduction in Garnet Solid-State Battery Films. *Nat. Energy* **2019**, 4, 475-483.

[26] Takada, K. Progress and Prospective of Solid-State Lithium Batteries. *Acta Materialia* **2013,** *61* (3), 759-770.

[27] Ohta, S.; Seki, J.; Yagi, Y.; Kihira, Y.; Tani, T.; Asaoka, T. Co-Sinterable Lithium Garnet-Type Oxide Electrolyte with Cathode for All-Solid-State Lithium Ion Battery. *J. Power Sources* **2014,** *265*, 40-44.

[28] Cheng, E. J.; Taylor, N. J.; Wolfenstine, J.; Sakamoto, J. Elastic Properties of Lithium Cobalt oxide ($LiCoO_2$). *Journal of Asian Ceramic Societies* **2017,** *5* (2), 113-117

[29] Kim, H. W.; Manikandan, P.; Lim, Y. J.; Kim, J. H.; Nam, S.-c.; Kim, Y. Hybrid Solid Electrolyte with the Combination of $Li_7La_3Zr_2O_{12}$ Ceramic and Ionic Liquid for High Voltage Pseudo-Solid-State Li-Ion Batteries. *J. Mater. Chem. A* **2016,** *4* (43), 17025-17032.

[30] Zhao, C.-Z.; Zhao, B.-C.; Yan, C.; Zhang, X.-Q.; Huang, J.-Q.; Mo, Y.; Xu, X.; Li, H.; Zhang, Q. Liquid Phase Therapy to Solid Electrolyte–Electrode Interface in Solid-State Li Metal Batteries: A Review. *Energy Storage Materials* **2020**, 24, 75-84

[31] Watanabe, M.; Thomas, M. L.; Zhang, S.; Ueno, K.; Yasuda, T.; Dokko, K. Application of Ionic Liquids to Energy Storage and Conversion Materials and Devices. *Chem. Rev.* **2017,** *117* (10), 7190-7239.

[32] Keller, M.; Appetecchi, G. B.; Kim, G.-T.; Sharova, V.; Schneider, M.; Schuhmacher, J.; Roters, A.; Passerini, S. Electrochemical Performance of a Solvent-Free Hybrid Ceramic-Polymer Electrolyte Based on $Li_7La_3Zr_2O_{12}$ in $P(EO)_{15}LiTFSI$. *J. Power Sources* **2017,** *353*, 287-297.

[33] Wakasugi, J.; Munakata, H.; Kanamura, K. Effect of Gold Layer on Interface Resistance between Lithium Metal Anode and $Li_{6.25}Al_{0.25}La_3Zr_2O_{12}$ Solid Electrolyte. *J. Electrochem. Soc.* **2017,** *164* (6), A1022-A1025.

[34] Wang, X.; Zhu, H.; Girard, G. M.; Yunis, R.; MacFarlane, D. R.; Mecerreyes, D.; Bhattacharyya, A. J.; Howlett, P. C.; Forsyth, M. Preparation and Characterization of Gel Polymer Electrolytes Using Poly(Ionic Liquids) and High Lithium Salt Concentration Ionic Liquids. *Journal of Materials Chemistry A* **2017,** *5* (45), 23844-23852.

[35] Ueno, K.; Yoshida, K.; Tsuchiya, M.; Tachikawa, N.; Dokko, K.; Watanabe, M. Glyme–Lithium Salt Equimolar Molten Mixtures: Concentrated Solutions or Solvate Ionic Liquids? *J. Phys. Chem. B* **2012,** *116* (36), 11323-11331.

[36] Sharafi, A.; Kazyak, E.; Davis, A. L.; Yu, S.; Thompson, T.; Siegel, D. J.; Dasgupta, N. P.; Sakamoto, J. Surface Chemistry Mechanism of Ultra-Low Interfacial Resistance in the Solid-State Electrolyte $Li_7La_3Zr_2O_{12}$. *Chemistry of Materials* **2017,** *29* (18), 7961-7968.

[37] Motoyama, M.; Tanaka, Y.; Yamamoto, T.; Tsuchimine, N.; Kobayashi, S.; Iriyama, Y. The Active Interface of Ta-Doped $Li_7La_3Zr_2O_{12}$ for Li Plating/Stripping Revealed by Acid Aqueous Etching. *ACS Appl. Energy Mater.* **2019,** *2* (9), 6720-6731.

[38] Vigneresse, J. L.; Barbey, P.; Cuney, M. Rheological Transitions during Partial Melting and Crystallization with Application to Felsic Magma Segregation and Transfer. *Journal of Petrology* **1996,** *37* (6), 1579-1600.

[39] Zhang, L.; Yang, T.; Du, C.; Liu, Q.; Tang, Y.; Zhao, J.; Wang, B.; Chen, T.; Sun, Y.; Jia, P. Lithium Whisker Growth and Stress Generation in an In Situ Atomic Force Microscope–Environmental Transmission Electron Microscope Set-Up. *Nature Nanotechnology* **2020**, 1-5.

[40] Cheng, E. J.; Sharafi, A.; Sakamoto, J. Intergranular Li Metal Propagation through Polycrystalline $Li_{6.25}Al_{0.25}La_3Zr_2O_{12}$ Ceramic Electrolyte. *Electrochim. Acta* **2017,** *223*, 85-91.

Chapter 3 Effects of porosity and ionic liquid-impregnation on the ionic conductivity of garnet-based flexible sheet electrolyte

3.1 Abstract

Although the garnet-type ceramic ionic conductor, $Li_7La_3Zr_2O_{12}$ (LLZO), shows relatively high stability against Li metal and can potentially replace flammable liquid electrolytes for Li metal batteries, the large interfacial resistance between LLZO and electrodes challenges its practical application. A possible solution is to produce a quasi-solid-state LLZO-based flexible sheet electrolyte. Here we prepared an Al-doped LLZO-based flexible sheet electrolyte and studied its ionic conductivity as functions of porosity and ionic liquid (IL) impregnation. Possible Li^+ ion conducting pathways through the quasi-solid-state composite sheet electrolyte were discussed, and its electrochemical performance was evaluated.

3.2 Introduction

With climate change becoming a pressing global issue, demand for clean and renewable energy has increased significantly in recent years. Rechargeable Li batteries, one of the most efficient energy storage systems to date, are promising in integrating renewable energy resources, such as wind and solar energies, into the electric power grid for electricity supply [1]. As electric vehicles (EVs) are quickly taking over the automobile industry, they are expected to considerably reduce CO_2 emission from the transport sector [2]. Consequently, EV batteries with improved safety and higher energy density are highly desirable.

Since a Li metal anode has a very high theoretical specific capacity of 3860 mA h g^{-1} (about 10 times higher than that of a graphite anode) and the lowest redox potential (-3.04 V *vs*. a standard hydrogen electrode), it is widely regarded as the ultimate anode material for high-energy-density

rechargeable Li batteries [3]. However, uncontrollable Li dendrite growth and other side reactions between Li metal and common liquid electrolytes make its practical use as an anode material impossible [4, 5]. In contrast, ceramic solid electrolytes, such as LLZO, can physically suppress the initiation and propagation of Li dendrite to a large extent because of their relatively high elastic and shear moduli [6-10]. Besides, LLZO is relatively stable in dry air, odorless, non-flammable, and compatible with Li metal anodes.

Nevertheless, because of the intrinsically brittle nature of polycrystalline LLZO, it is difficult to form good interfacial contacts between LLZO and electrode materials, which usually results in high interfacial resistance, especially on the cathode side [11]. Considerable research effort has been devoted to decreasing the high interfacial resistance in Li metal batteries with an LLZO solid electrolyte [12-17]. For example, the interfacial resistance between LLZO and Li metal can be effectively reduced by introducing a thin Au interlayer [18-19]. In contrast, much less effort has been placed on reducing the cathode-side interfacial resistance. Although good interfacial bonding between LLZO and some cathode materials, such as $LiCoO_2$ (LCO), could be achieved by co-sintering [20], Li loss and various side reactions are also likely to occur at high temperatures. A few works have explored the potential of IL-impregnated composite cathodes, where the pre-introduced IL can wet the cathode/solid electrolyte interface [21, 22]. LLZO particles can also be incorporated into polyethylene oxides (PEOs) to form composite flexible sheet electrolytes, forming good interfacial contact with the cathode [23, 24]. In our research, we have developed an IL-containing LLZO-based flexible sheet electrolyte at room temperature through tape-casting [21]. It is worth noting that high-temperature sintering (e.g., at 1200 °C) for large-scale production of LLZO membranes is very difficult, mainly due to the poor mechanical stability of LLZO membranes.

Here we studied the effect of porosity and IL impregnation on the ionic conductivity of an Al-doped LLZO-based flexible sheet electrolyte. The ionic conductivity of the sheet electrolyte increased with decreasing porosity before IL impregnation. However, the IL uptake of the sheet electrolyte was proportional to its porosity, and the absorbed IL was found to play a dominant role in determining the ionic conductivity of the sheet electrolyte after IL impregnation. The optimal porosity for IL impregnation was about 30 vol%, and the quasi-solid-state sheet electrolyte showed an ionic conductivity of 1.1×10^{-4} S cm^{-1} at 25 ℃. In addition, the electrochemical stability and cycling performance of the quasi-solid-state composite sheet electrolyte were also evaluated.

3.3 Experiment

3.3.1 Tape-casting of flexible Al-doped LLZO sheet electrolyte

An Al-doped LLZO powder (D50 = 10 μm, Daiichi Kigenso Kagaku Kogyo Co., Ltd., Japan) and a polystyrene-type elastomeric binder (Chukyo Yushi Co., Ltd., Japan) (w:w = 20:1) were mixed in toluene (Wako Pure Chemical Corp., Japan). The mixture was ball-mixed (ZrO_2 ball, 5 mm in diameter) with a planetary centrifugal vacuum mixer (ARV-310, Thinky, Japan) at 2000 rpm for 30 min. The obtained slurry was cast onto a polyethylene terephthalate (PET) substrate (75 μm in thickness) using a doctor blade. The thickness of the sheet could be easily controlled by changing the gap between the moving doctor bade and the stationary PET substrate. In this study, the thickness of the as-cast sheet electrolyte was controlled to be around 350 μm.

3.3.2 Cold isostatic pressing

Circular samples were punched from the vacuum-dried sheet and were cold isostatically pressed (CIP) at 100, 300, 500, 700, and 900 MPa for 5 min at room temperature. After Au coating (ionic current: 3.5 mA; sputtering time: 1 h for one side), the samples were immersed in a solvate IL for 8 h in an Ar atmosphere. The IL, Li(G4)FSI, was prepared by dissolving lithium

bis(fluorosulfonyl)imide (LiFSI) in equimolar tetraglyme (G4). The absorbed IL content was determined by weighing the sheet samples before and after IL impregnation.

3.3.3 Preparation of quasi-solid-state LCO cathode

An LCO powder, an acetylene black (AB), a polyvinylidene difluoride (PVDF) binder, and the solvate IL (w:w:w = 92:4:4:18) were ball-mixed in N-methyl-2-pyrrolidone (NMP), and the slurry was cast onto an Al foil (20 μm thick). The composite cathode was dried at 80 °C in a vacuum for 8 h before use.

3.3.4 Materials characterization

The microstructure of the flexible sheet electrolyte was observed using a scanning electron microscope (SEM, JSM-6490A). The thermal stability of the sheet electrolyte was studied using a thermogravimetric analyser (TG, DTG-60 H, SHIMADZU, Japan) between 30 and 300 ℃ with a heating rate of 5 ℃ min^{-1}. Interaction between the IL and Al-LLZO was analyzed with differential scanning calorimetry (DSC, TA-60 WS, Shimadzu, Japan) from -80 to 80 ℃ with a scanning rate of 2 ℃ min^{-1}.

3.3.5 Electrochemical characterization

AC electrochemical impedance spectroscopy (EIS, Biologic SP-300 Potentiostat, France) was carried out to determine the ionic conductivity of the sheet electrolyte in the frequency range from 1 MHz to 1 Hz with a perturbation of 10 mV. The temperature range for the EIS measurement was 25 to 100 ℃. The surface of the sheet electrolyte was coated with a thin gold layer as an ionically blocking electrode for the EIS measurement. The electrochemical stability of the IL was evaluated by linear sweep voltammetry (LSV) and cyclic voltammetry (CV) at 30 °C. The scan rates for LSV and CV were 1 mV s^{-1}. Li/Al-LLZO/Li symmetric cells were galvanostatically cycled with a

current density of up to 0.5 mA cm^{-2}. To reduce the anode-side interfacial resistance, the surface of the sheet electrolyte was coated with a thin Au layer, which would alloy with Li metal at heating. Quasi-solid-state LCO/Al-LLZO sheet/Li cells were galvanostatically cycled at both 30 and 60 °C in the voltage range of 2.5-4.2 V.

3.4 Results and discussions

3.4.1 Optical image of tape-cast Al-LLZO sheet electrolyte

Fig. 3.1(a) shows an optical image of the tape-cast Al-LLZO sheet electrolyte on a PET substrate. After drying, the Al-LLZO sheet with a thickness of 350 μm could be easily peeled off from the PET substrate and was self-standing (Fig. 3.1(b)). Although the Al-LLZO content in the dry sheet was as high as 95 wt%, the sheet could be folded and twisted without breaking, demonstrating good flexibility and mechanical stability (Fig. 3.1(c)). Cross-sectional SEM micrographs revealed the porous structure of the tape-cast sheet electrolyte (Fig. 3.1(d)). Nano-sized pores were observed among primary Al-LLZO particles, while micro-sized pores were observed among secondary Al-LLZO particles. The porosity of the sheet after drying was estimated to be 50%.

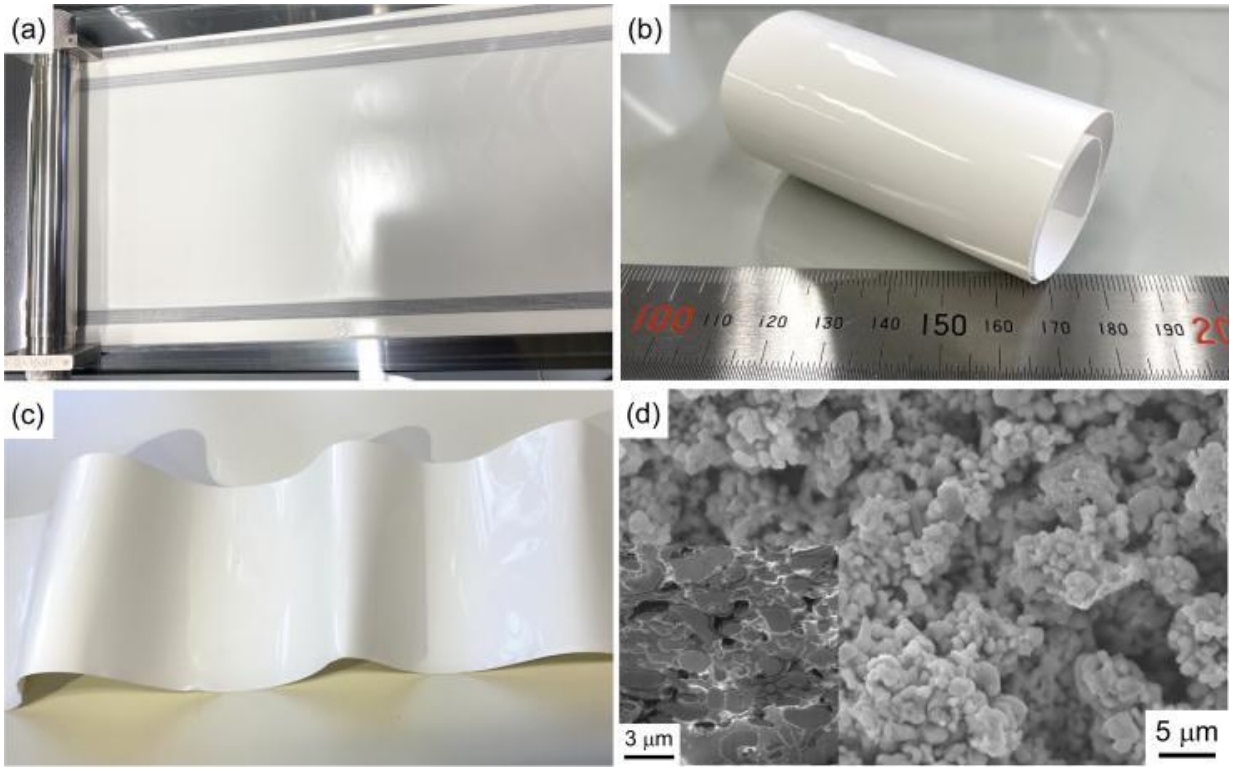

Fig. 3.1 Optical and SEM images of the flexible Al-LLZO sheet electrolyte. (a) Tape-casting of the Al-LLZO sheet on a 75 μm-thick PET substrate, (b) Self-standing Al-LLZO sheet after peeling off the PET substrate, (c) Dry sheet with a thickness of 350 μm shows good flexibility, (d) Fractured cross-section of the sheet electrolyte. The inset shows a cross-section of the sheet cut by focused ion beam (FIB).

3.4.2 SEM micrographs of as-dried and cold-pressed Al-LLZO sheets

Fractured cross-sectional SEM images of the as-dried and isostatically cold-pressed Al-LLZO sheet electrolytes are shown in Fig. 3.2. The sheet thickness decreased from 343 to 253 μm (Figs. 3.2(a) and (c)) when pressed at 100 MPa. The sheet porosity was reduced from 50% to 32% accordingly (Figs. 3.2(b) and (d)). The sheet thickness and porosity were further decreased to 230 μm and 25%, respectively, when pressed at 300 MPa (Figs. 3.2(e) and (f)). With the pressure

increasing to 500 MPa, the sheet porosity decreased to 19% (Figs. 3.2(g) and (h)). However, the porosity only slightly decreased from 15% to 13% when the pressure increased from 700 to 900 MPa (Figs. 3.2(i)-(l)), indicating that particle rearrangement and consolidation through plastic deformation were almost completed when pressed at 700 MPa.

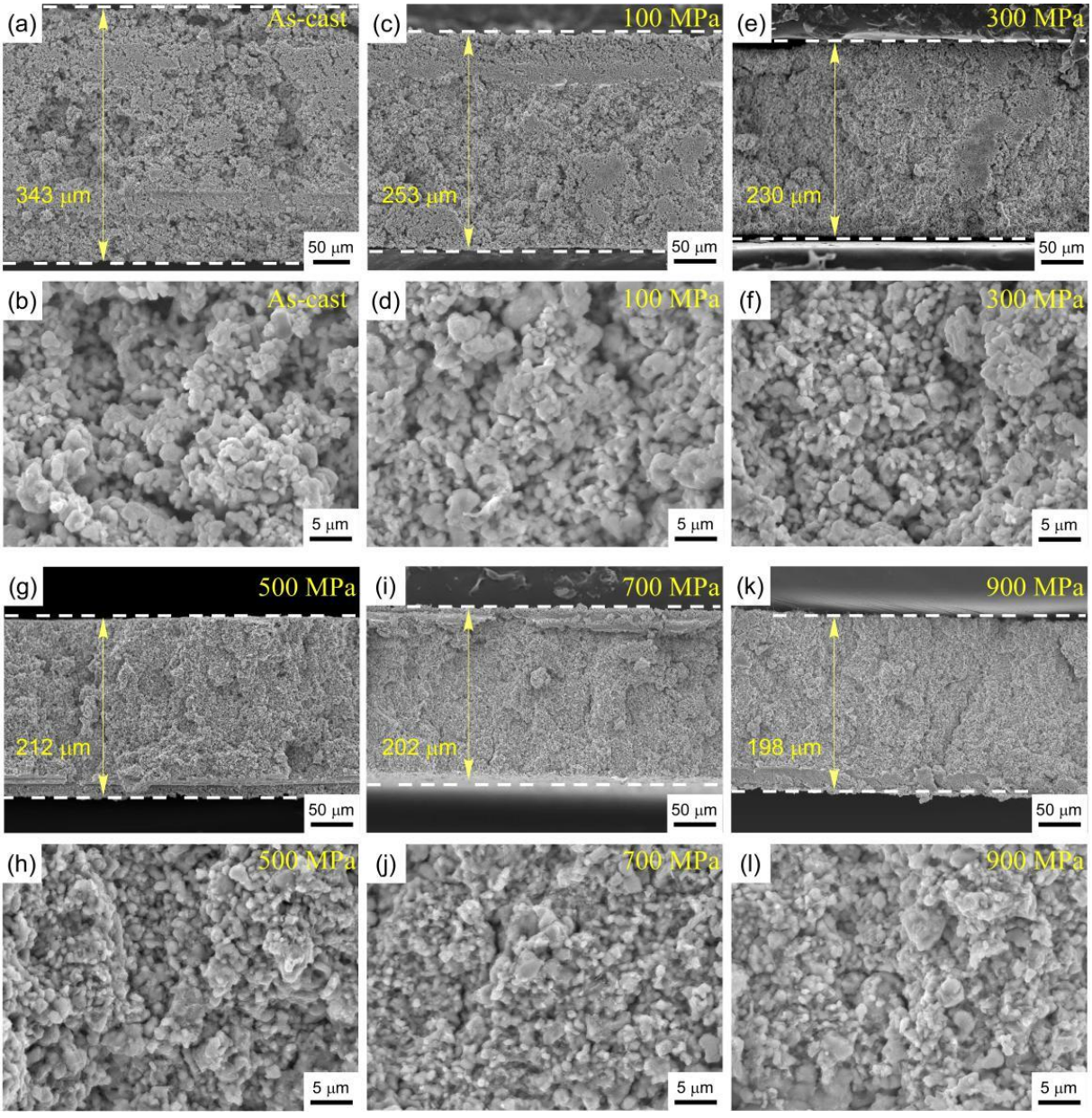

Fig. 3.2 SEM cross-sectional micrographs of as-dried and cold-pressed Al-LLZO sheets. (a) and (b) as-dried sheet, 343 μm thick, (c) and (d) 100 MP cold-pressed sheet, 253 μm thick, (e) and (f)

300 MP cold-pressed sheet, 230 μm thick, (g) and (h) 500 MP cold-pressed sheet, 212 μm thick, (i) and (j) 700 MP cold-pressed sheet, 202 μm thick, (k) and (l) 900 MP cold-pressed sheet, 198 μm thick. The pressure holding time was 5 min for all cases.

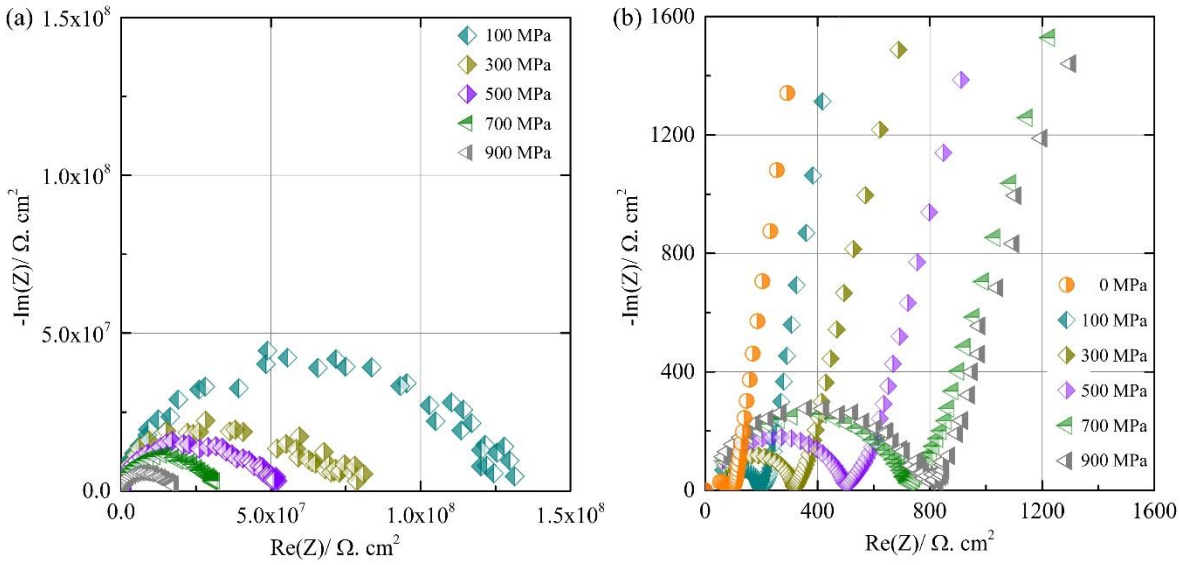

Fig. 3.3 EIS measurement of the sheet electrolyte at 25 ℃ before and after IL impregnation. (a) Impedance evolution of the as-dried sheet electrolyte as a function of cold-pressing pressure (before IL impregnation), (b) Impedance evolution of the IL-impregnated sheet electrolyte as a function of cold-pressing pressure.

3.4.3 EIS measurement of the sheet electrolyte

As shown in Fig. 3.3, (a), the overall impedance $R_{overall}$ of the sheet electrolyte decreased drastically from 1.3×10^8 Ω cm^2 when pressed at 100 MPa to 1.8×10^7 Ω cm^2 when pressed at 900 MPa. However, the ionic conductivity of the sheet electrolyte could only reach 1.2×10^{-9} S cm^{-1} at 25 ℃ even when pressed at 900 MPa. Cold-pressed sheets were immersed in the solvate Li(G4)FSI IL to improve the ionic conductivity. Since IL uptake by the sheet was proportional to the sheet porosity, the IL uptake was expected to decrease with increasing pressure. The impedance

evolution of the IL-impregnated sheet electrolyte as a function of cold-pressing pressure is depicted in Fig. 3.3(b). On the other hand, the $R_{overall}$ of the cold-pressed and IL-impregnated sheet electrolyte decreased from 803 to 198 Ω cm^2 when the cold-pressing pressure decreased from 900 to 100 MPa. Accordingly, the ionic conductivity of the cold-pressed and IL-impregnated sheet electrolyte increased from 2.7×10^{-5} to 1.1×10^{-4} S cm^{-1} at 25 ℃. When no pressure was applied, the impedance of the quasi-solid-state sheet was only 81 Ω cm^2, corresponding to an ionic conductivity of 2.6×10^{-4} S cm^{-1} at 25 ℃, which was comparable to that of high-temperature sintered Al-LLZO pellets [25, 26]. Given that the room temperature ionic conductivity of the cold-pressed sheet electrolyte was only 1.2×10^{-9} S cm^{-1}, the IL likely played a dominant role in determining the ionic conductivity of the quasi-solid-state composite sheet electrolyte.

3.4.4 Ionic conductivity of the 100 MPa cold-pressed and IL-impregnated sheet electrolyte

After IL impregnation, the IL content in the 100 MPa cold-pressed sheet was 14.6 wt%, corresponding to 32 vol%. Based on percolation theory [27], a solid-liquid system would become locked when the liquid was less than 30 vol%. This is because the liquid became discontinuous and was unable to flow. Fig. 3.4 shows the temperature dependence of the total ionic conductivity of the 100 MPa pressed and IL-impregnated sheet electrolyte. The ionic conductivity σ was determined using the following equation (Eq. (3.1)):

$$\sigma = \frac{L}{RA} \qquad (3.1)$$

where L is the sheet thickness, and A is the active electrode area. The ionic conductivity increased from 1.1×10^{-4} S cm^{-1} at 25 ℃ to 6.5×10^{-4} S cm^{-1} at 85 ℃. The temperature dependence of the ionic conductivity was fitted with the Arrhenius equation (Eq. (3.2))

$$\sigma(T) = \sigma_0 \exp[-E_a/(RT)] \qquad (3.2)$$

where σ is the ionic conductivity, σ_0 is the pre-exponential factor (a constant with the same unit as σ), T is the absolute temperature, E_a is the activation energy, and R is the universal gas constant. The activation energy was estimated to be 0.27 eV, slightly higher than that of Al-LLZO, 0.26 eV, but lower than that of the IL, 0.31 eV [21]. The activation energy of the quasi-solid-state sheet electrolyte was expected to vary with the absorbed IL content.

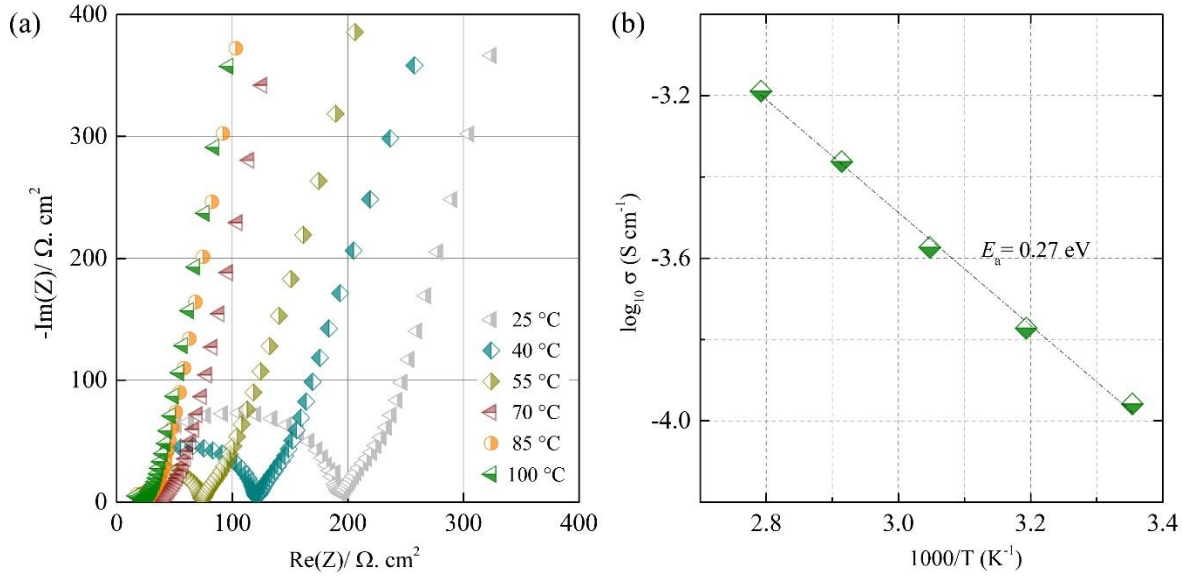

Fig. 3.4 Temperature dependence of the ionic conductivity of the 100 MPa cold-pressed and IL-impregnated quasi-solid-state sheet electrolyte. (a) Impedance evolution of the quasi-solid-state sheet electrolyte as a function of temperature, (b) Arrhenius conductivity.

3.4.5 Thermal stability of the 100 MPa cold-pressed and IL-impregnated sheet electrolyte

TGA measurement was performed in dry air and N_2 in the temperature range of 30 to 300 ℃ to study the thermal stability of the 100 MPa cold-pressed and IL-impregnated quasi-solid-state sheet electrolyte (Fig. 3.5(a)). The weight loss of the sheet was less than 1% up to 110 ℃, most likely due to the evaporation of residual toluene, adsorbed water, and the impregnated solvate IL. However, a sharp weight loss was observed when the temperature was greater than 150 ℃,

indicating the thermal decomposition of the IL. In addition, the quasi-solid-state sheet electrolyte showed slightly higher thermal stability in N_2 than in dry air. DSC analysis of the quasi-solid-state sheet electrolyte is shown in Fig. 3.5(b). The endothermic peak of the IL at 29.5 ℃ was associated with the melting of the IL. The melting point shifted slightly to a higher temperature with the presence of Al-LLZO, indicating an interaction between the IL and Al-LLZO, likely a Li^+ exchange reaction [28].

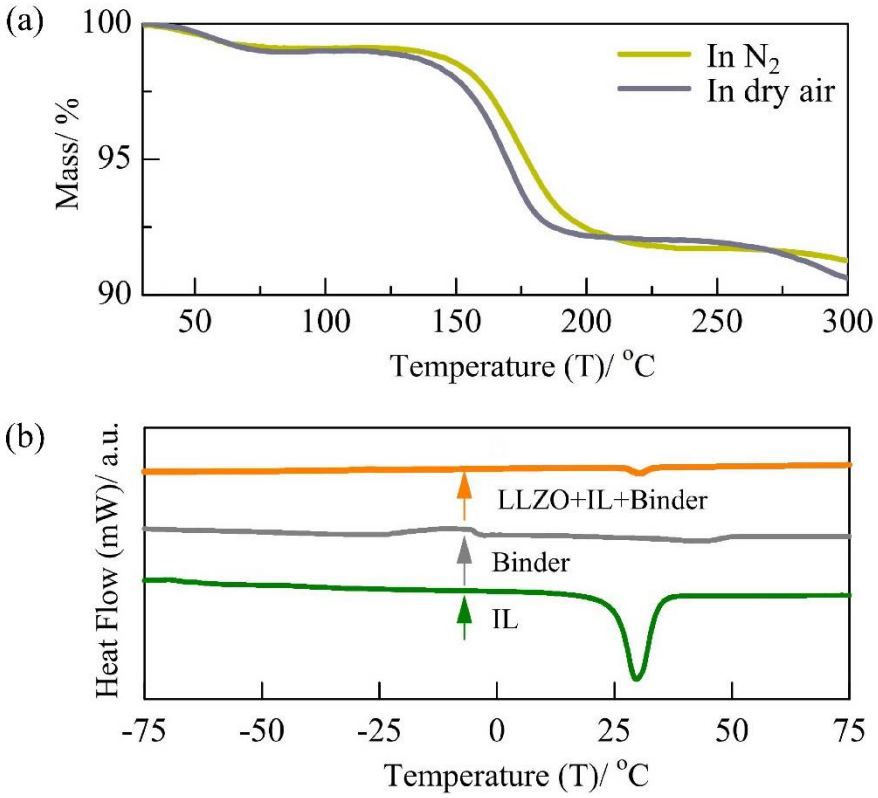

Fig. 3.5 Thermal stability of the 100 MPa cold-pressed and IL-impregnated quasi-solid-state sheet electrolyte. (a) TGA spectra of the electrolyte in dry air and N_2 from 30 to 300 ℃, (b) DSC analysis.

3.4.6 Electrochemical stability analysis of the Li(G4)FSI solvate IL

The electrochemical stability of the Li(G4)FSI solvate IL was studied by linear sweep voltammetry and cyclic voltammetry (Fig. 3.6). An Au foil was used as the working electrode (WE), and a Li foil was used as the counter electrode (CE) as well as the reference electrode (RE). The IL showed good anodic stability of up to 4.5 V *vs*. Li/Li^+ because the anodic current density was negligible (less than 0.025 mA cm^{-2}) at potentials below 4.5 V *vs*. Li/Li^+ (Fig. 3.6(a)). The drastic increase of the anodic current density at potentials above 5.0 V *vs*. Li/Li^+ could be attributed to the strong oxidation of the solvate IL. More specific information was provided by CV analysis. As shown in Fig. 3.6(b), no noticeable redox peaks were observed in the potential range of 2.8 V to 4.8 V *vs*. Li/Li^+, indicating that the IL had a relatively wide electrochemical window. However, broad redox peaks were observed in CV profiles when an Al foil was used as the WE (Fig. 3.1S), possibly related to the corrosion of the Al current collector in the solvate IL.

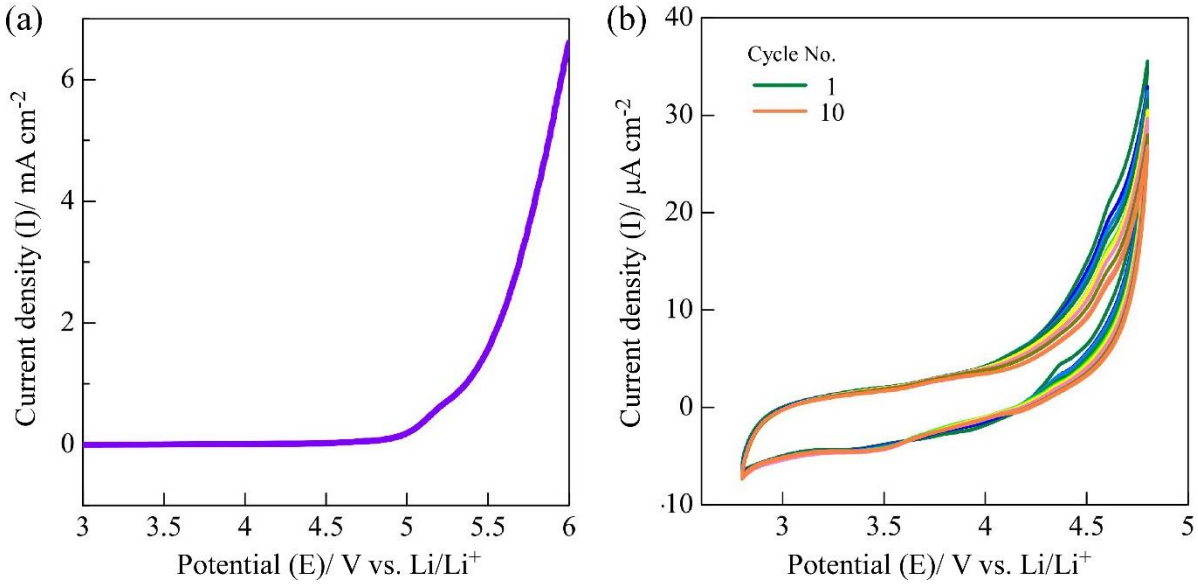

Fig. 3.6 Electrochemical stability analysis of the Li(G4)FSI solvate IL. (a) Linear sweep voltammogram of Li(G4)FSI. (b) Cyclic voltammogram of Li(G4)FSI. The scan rates for LSV and

CV were 1 mV s^{-1}. An Au foil was used as the WE, and Li was used as the CE and the RE. A highly porous polyimide film (PI) was used as the separator.

3.4.7 Critical current density and possible Li^+ ion pathways in the sheet electrolyte

The relationship between the applied potential across the Li/Al-LLZO sheet/Li symmetric cell and the current density obtained at a steady state is plotted in Fig. 3.7(a). The 100 MPa cold-pressed and IL-impregnated quasi-solid-state sheet electrolyte showed good stability at current densities up to 250 μA cm^{-2} at 60 ℃. Short-circuiting occurred at 300 μA cm^{-2}, likely due to Li dendrite growth as observed in Li/LLZO pellet/Li symmetric cells [29-31]. However, the critical current density of the quasi-solid-state sheet electrolyte was lower than that of dense Al-LLZO pellets. One explanation was that high-temperature sintered Al-LLZO pellets had higher elastic moduli than the quasi-solid-state flexible sheet electrolyte. Possible Li^+ ion conducting pathways through the quasi-solid-state sheet electrolyte are illustrated in Fig. 3.7(b). Since the IL was discontinuous in the sheet electrolyte as its volume fraction was less than the particle locking threshold of 30% according to percolation theory, both the Al-LLZO particles and the IL were supposed to participate in the conduction of Li^+ through the sheet electrolyte (pathway I). The proposed Li^+ pathway was also evidenced by the activation energy of the sheet electrolyte. However, considering that the volume fraction of the IL was slightly over 30%, Li^+ ions could also migrate through the IL directly to some extent (pathway II).

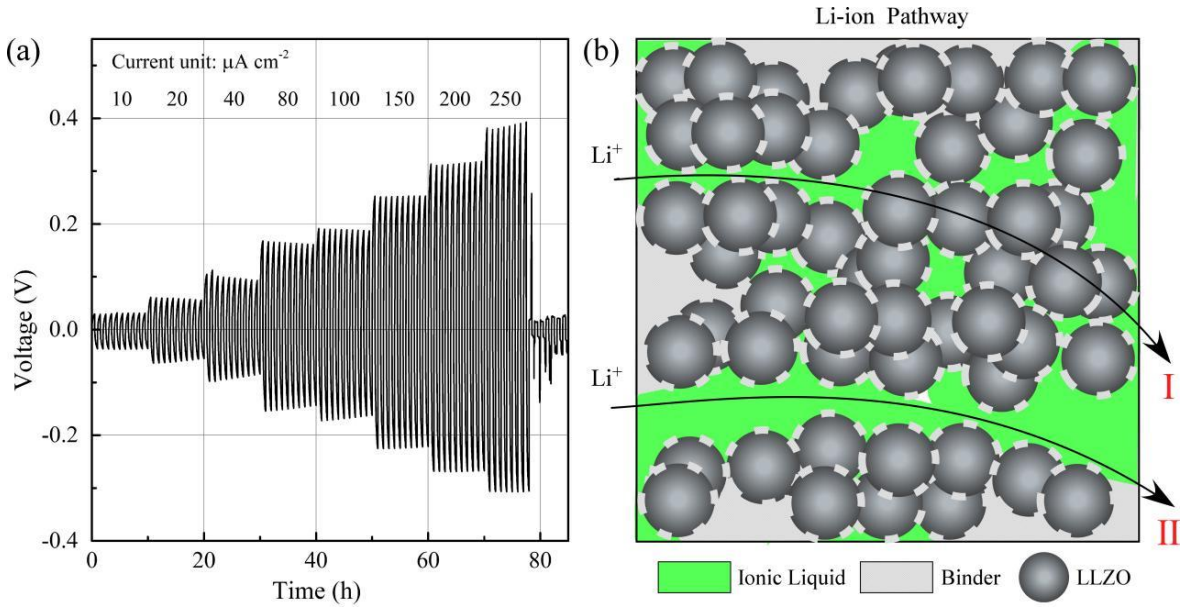

Fig. 3.7 Critical current density and possible Li^+ ion pathways of the 100 MPa cold-pressed and IL-impregnated quasi-solid-state sheet electrolyte. (a) Charge and discharge profile of a Li/quasi-solid-state Al-LLZO sheet/Li symmetric cell at 60 ℃, (b) Proposed Li^+ ion pathways.

3.4.8 Cycling performance of the quasi-solid-state sheet electrolyte

Cycling tests of the quasi-solid-state LCO/ Al-LLZO sheet/ Li cells at both 30 and 60 °C are shown in Fig. 3.8. The cell delivered an initial discharge capacity of 126 mA h g^{-1} at 30 °C (Fig. 3.8(a)). However, noticeable capacity fading was observed after a few cycles. On the other hand, the initial discharge capacity was 117 mA h g^{-1} at 60 °C, and the capacity decayed faster than that at 30 °C (Fig. 3.8(b)). The instability of the solvate IL was believed to be one of the main reasons for the capacity degradation. As illustrated in Fig. 3.8 (c), interactions between nanoporous carbon black and the solvate IL, such as nanoconfinement effects [32-33], may lead to dissociation or desolvation of the ionic pairs of Li(G4)FSI. In addition, possible side reactions between LLZO and

the IL could also be responsible for the decay of the Li metal cell. Thus, searching for a suitable IL is essential for developing the quasi-solid-state LLZO-based composite flexible sheet electrolyte.

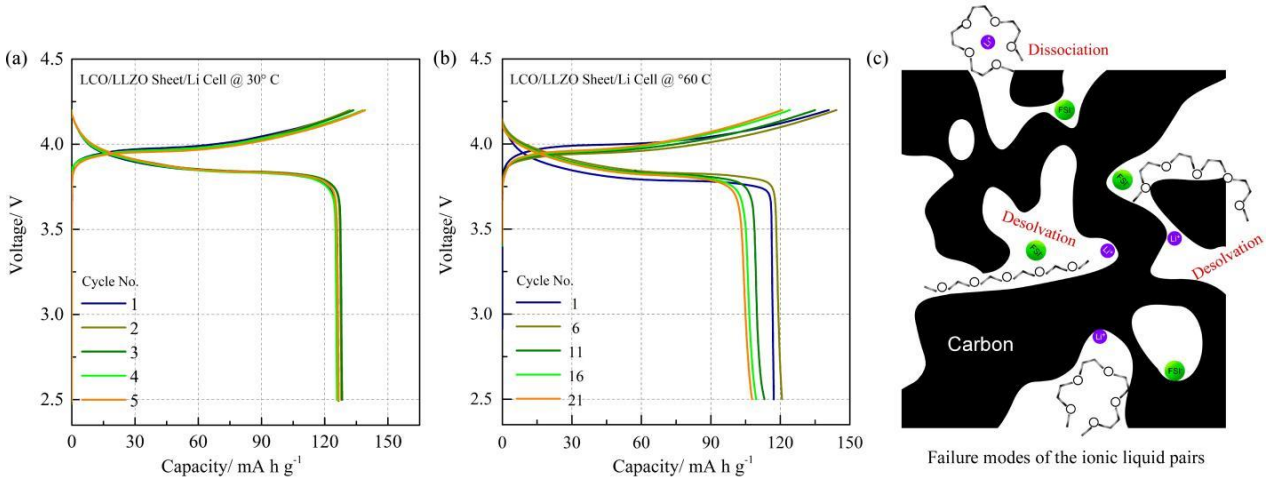

Fig. 3.8 Cycling performance of a quasi-solid-state Li/LLZO sheet/LCO cell and possible mechanisms for the cell capacity decay. (a) Galvanostatic cycling (0.1 C) at 30 °C, (b) Galvanostatic cycling (0.1 C) at 60 °C, and (c) Proposed failure modes of the solvate IL.

3.5 Conclusions

The effects of porosity and IL-impregnation on the ionic conductivity of a room-temperature synthesized Al-LLZO-based flexible sheet electrolyte were investigated. The ionic conductivity increased with decreasing porosity but could only reach 1.2×10^{-9} S cm^{-1} at 25 °C through cold pressing. On the other hand, IL uptake by the flexible sheet electrolyte was proportional to its porosity, and the optimal porosity was about 30%, according to percolation theory. Both the Al-LLZO particles and the IL were supposed to participate in the conduction of Li^+ ions in the IL-impregnated sheet electrolyte, and the quasi-solid-state flexible sheet electrolyte showed an improved ionic conductivity of 1.1×10^{-4} S cm^{-1} at 25 °C. The IL appeared to play a dominant role in determining the ionic conductivity of the quasi-solid-state sheet electrolyte. However, the

discharge capacity of the quasi-solid-state Li/LLZO sheet/LCO cell degraded rapidly with cycling. One main reason was likely related to the dissociation or desolvation of the Li(G4)FSI solvate IL. Thus, identifying a suitable IL is critical for developing the LLZO-based quasi-solid-state flexible sheet electrolyte.

Reference

[1] M.S. Whittingham, Nano Lett. 20 (2020)8435-8437.

[2] M.J. Haugen, L. Paoli, J. Cullen, D. Cebon, A.M. Boies, Applied Energy, 283 (2021) 116295.

[3] X. Shen, X. Zhang, F. Ding, J. Huang, R. Xu, X. Chen, C. Yan, F. Su, C. Chen, X. Liu, Energy Material Advances, 2021 (2021).

[4] X. Fan, C. Wang, Chemical Society Reviews, (2021).

[5] C. Fang, X. Wang, Y.S. Meng, Trends in Chemistry, 1 (2019) 152-158.

[6] R. Murugan, V. Thangadurai, W. Weppner, Angewandte Chemie International Edition, 46 (2007) 7778-7781.

[7] N.J. Taylor, S. Stangeland-Molo, C.G. Haslam, A. Sharafi, T. Thompson, M. Wang, R. Garcia-Mendez, J. Sakamoto, Journal of Power Sources, 396 (2018) 314-318.

[8] H. Zheng, S. Wu, R. Tian, Z. Xu, H. Zhu, H. Duan, H. Liu, Advanced Functional Materials, 30 (2020) 1906189.

[9] N. Zhao, W. Khokhar, Z. Bi, C. Shi, X. Guo, L.Z. Fan, C.W. Nan, Joule, 3 (2019) 1190-1199.

[10] D. Wang, C. Zhu, Y. Fu, X. Sun, Y. Yang, Advanced Energy Materials, 10 (2020) 2001318.

[11] Y. Iriyama, M. Wadaguchi, K. Yoshida, Y. Yamamoto, M. Motoyama, T. Yamamoto, Journal of Power Sources, 385 (2018) 55-61.

[12] T. Matsuyama, R. Takano, K. Tadanaga, A. Hayashi, M. Tatsumisago, Solid State Ionics, 285 (2016) 122-125.

[13] D. Wang, Q. Sun, J. Luo, J. Liang, Y. Sun, R. Li, K. Adair, L. Zhang, R. Yang, S. Lu, ACS applied materials & interfaces, 11 (2019) 4954-4961.

[14] W. Feng, X. Dong, P. Li, Y. Wang, Y. Xia, Journal of Power Sources, 419 (2019) 91-98.

[15] Y. Shao, H. Wang, Z. Gong, D. Wang, B. Zheng, J. Zhu, Y. Lu, Y.S. Hu, X. Guo, H. Li, ACS Energy Letters, 3 (2018) 1212-1218.

[16] F. Han, J. Yue, C. Chen, N. Zhao, X. Fan, Z. Ma, T. Gao, F. Wang, X. Guo, C. Wang, Joule, 2 (2018) 497-508.

[17] L. Chen, Z. Huang, W. Pang, Z. Jin, Y. Li, C.A. Wang, Electrochimica Acta, 330 (2020)135352.

[18] C. Tsai, V. Roddatis, C. Chandran, Q. Ma, S. Uhlenbruck, M. Bram, P. Heitjans, O. Guillon, ACS applied materials & interfaces, 8 (2016) 10617-10626.

[19] J. Wakasugi, H. Munakata, K. Kanamura, Journal of The Electrochemical Society, 164 (2017) A1022-A1025.

[20] S. Ohta, M. Kawakami, H. Nozaki, C. Yada, T. Saito, H. Iba, Journal of Materials Chemistry A, 8 (2020) 8989-8996.

[21] E.J. Cheng, T. Kimura, M. Shoji, H. Ueda, H. Munakata, K. Kanamura, ACS applied materials & interfaces, 12 (2020) 10382-10388.

[22] L. Liu, X. Qi, Q. Ma, X. Rong, Y Hu, Z. Zhou, H. Li, X. Huang, L. Chen, ACS applied materials & interfaces, 8 (2016) 32631-32636.

[23] M. Keller, G.B. Appetecchi, G. Kim, V. Sharova, M. Schneider, J. Schuhmacher, A. Roters, S. Passerini, Journal of Power Sources, 353 (2017) 287-297.

[24] L. Chen, Y. Li, S. Li, L. Fan, C. Nan, J.B. Goodenough, Nano Energy, 46 (2018) 176-184.

[25] J. Gao, J. Zhu, X. Li, J. Li, X. Guo, H. Li, W. Zhou, Advanced Functional Materials, 31 (2021) 2001918.

[26] M. Kotobuki, M. Koishi, Journal of Alloys and Compounds, 826 (2020) 154213.

[27] J.L. Vigneresse, P. Barbey, M. Cuney, Journal of Petrology, 37 (1996) 1579-1600.

[28] X. Wang, H. Zhu, G.M. Girard, R. Yunis, D.R. MacFarlane, D. Mecerreyes, A.J. Bhattacharyya, P.C. Howlett, M. Forsyth, Journal of Materials Chemistry A, 5 (2017) 23844-23852.

[29] Y. Ren, Y. Shen, Y. Lin, C. Nan, Electrochemistry Communications, 57 (2015) 27-30.

[30] E.J. Cheng, A. Sharafi, J. Sakamoto, Electrochimica Acta, 223 (2017) 85-91.

[31] X. Liu, R. Garcia-Mendez, A.R. Lupini, Y. Cheng, Z.D. Hood, F. Han, A. Sharafi, J.C. Idrobo, N.J. Dudney, C. Wang, Nature Materials, (2021) 1-6.

[32] F. Borghi, C. Piazzoni, M. Ghidelli, P. Milani, A. Podestà, The Journal of Physical Chemistry C, 125 (2021) 1292-1303.

[33] D. Weingarth, R. Drumm, A. Foelske-Schmitz, R. Kötz, V. Presser, Phys. Chem. Chem. Phys., 2014, 16, 21219-21224

Chapter 4 Preparation of garnet-based flexible separator

4.1 Abstract

A separator between a battery's anode and cathode is crucial to isolate the electrodes and prevent an electrical short circuit. Separators in Li-ion batteries are generally made of polyolefins, such as polyethylene (PE) and polypropylene (PP). However, the relatively low thermal stability and mechanical strength of polyolefin-based separators have raised safety concerns, especially when overheating occurs. Ceramic coatings, for instance, Al_2O_3 and ZrO_2, have been applied to improve the thermal and mechanical properties of polyolefin separators. Here we developed Al_2O_3 and $Li_7La_3Zr_2O_{12}$ (LLZO)-based polymer-in-ceramic membranes and studied their porosity, thermal stability, electrolyte wettability, and ionic conductivity as Li-ion battery separators. In particular, the polymer-in-LLZO separator showed higher thermal stability, higher ionic conductivity, and better wettability with the 1 M $LiPF_6$/EC: DEC (1:1) electrolyte than the commercial PP separator Celgard 2400. The performance of the polymer-in-LLZO separator was also evaluated in an NCM811|Li cell with the 1 M $LiPF_6$/EC: DEC (1:1) electrolyte.

4.2 Introduction

Li-ion batteries are ubiquitous today, powering various electronic systems, from consumer electronics to electric vehicles (EVs). As EVs quickly take over the automobile industry, EV batteries with higher energy density and improved safety are highly desired [1]. A separator is essential in a Li-ion battery, preventing physical contact between the positive and negative electrodes while allowing fast Li-ion transport. Polyolefin-based membranes dominate the separator market of Li-ion batteries because polyolefin-based membranes can be very thin (20-25 μm), mechanically robust, porous, wettable with liquid electrolytes, and cost-effective [2-4].

Nevertheless, they also have some disadvantages, such as low thermal stability and porosity (about 40%) [5]. Thermal shrinkage of polyolefin-based separators can potentially lead to thermal runaway and explosion of Li-ion batteries. Thus, separators with improved thermal stability are highly desired to improve battery safety.

Ceramic coatings, such as Al_2O_3 and ZrO_2, have been used to increase the thermal stability of polyolefin-based separators [6, 7]. Nonetheless, the ceramic coatings will increase the thickness of the separator and block the pores, inevitably decreasing the separator's ionic conductivity. LLZO-in-polymer flexible solid electrolytes (separators) have recently attracted attention and demonstrated good electrochemical performances [8, 9]. The garnet-type fast Li-ion conducting LLZO with a cubic crystal structure (space group Ia-3d) was first discovered in 2007 [10]. It has a high ionic conductivity of about 10^{-4} S cm^{-1} at room temperature and is relatively stable against reaction with molten Li. As a result, LLZO is widely regarded as one of the most promising solid electrolytes for all-solid-state Li metal batteries [11, 12]. However, LLZO does not form good contact with electrodes because of its high elastic modulus [13], which results in high interfacial resistance. Alternatively, LLZO particles have been used as ceramic fillers in polymer-based composite electrolytes to improve the low conductivities and poor mechanical properties of polymer electrolytes, such as polyethylene oxide (PEO) [9, 14]. In this situation, porosity is undesirable for the LLZO-in-polymer solid electrolyte because it is detrimental to ionic conductivity. On the other hand, high porosity is favorable for the LLZO-in-polymer separator used in combination with liquid electrolytes because a highly porous structure can facilitate the infiltration of the liquid electrolyte.

Besides thickness and ionic conductivity, wettability is another important characteristic of Li-ion battery separators because electrolyte absorption is essential for Li^+ transport. Meanwhile, a

highly porous structure will improve wettability and electrolyte uptake [15]. Recent literature on Li-ion battery separators is focused on applying nano-particle additives and surface coatings to improve their electrolyte wettability, mechanical strength, and thermal stability [16]. Here we developed polymer-in-Al_2O_3 and polymer-in-LLZO flexible thin films through tape casting at room temperature and studied their porosity, thermal stability, electrolyte wettability, and ionic conductivity. Although tape-cast polymer-in-Al_2O_3 flexible films have been reported previously, they are usually several hundred microns thick [17, 18].

In contrast, the polymer-in-Al_2O_3 film we developed here was only about 25 μm thick. Moreover, replacing the ionically insulating Al_2O_3 with the fast-ion-conducting LLZO is expected to improve the separator's ionic conductivity. So far, almost no research has been reported on the tape casting of polymer-in-LLZO flexible thin films at room temperature [19, 20]. Finally, the electrochemical performance of the polymer-in-ceramic films as separators was evaluated in an NCM811|Li cell with a 1 M $LiPF_6$/EC: DEC (1:1) electrolyte, and the cell failure mechanism was also discussed.

4.3 Material and methods

4.3.1 Casting of polymer-in-ceramic thin films

An α-Al_2O_3 powder (average particle size: 10 μm, Admatechs Co., Ltd., Japan) and an elastomeric binder (Chukyo Yushi Co., Ltd., Japan) were mixed in toluene (99.0%, Wako Pure Chemical Corp., Japan). The mass ratio between the toluene and the alumina powder was 3:8. The mixture was ball-mixed (ZrO_2 balls with a diameter of 5 mm) using a planetary centrifugal vacuum mixer (ARV-310, Thinky, Japan) at 2000 rpm for 30 min. The formed Al_2O_3 slurry was cast onto a polyethylene terephthalate (PET) substrate. The PET substrate was 75 μm thick with good flexibility and mechanical robustness. The thickness of the as-cast polymer-in-Al_2O_3 film could be

easily controlled by changing the gap between the moving doctor blade and the stationary PET substrate. The as-cast Al_2O_3 film was vacuum-dried at 25 ℃ for 12 h, and the mass ratio between the polymer binder and the ceramic powder was 3:20. The polymer-in-LLZO film was prepared similarly. However, the viscosity of the LLZO slurry was much higher than that of the Al_2O_3 slurry, making it relatively difficult to prepare films as thin as 25 μm. The D50 value of the LLZO (Daiichi Kigenso Kagaku Kogyo Co., Ltd., Japan) particle size distribution was about 10 μm.

4.3.2 Materials characterization

The microstructure of the polymer-in-ceramic films was observed using a scanning electron microscope (SEM, JSM-6490A, JEOL, Japan). Cross-sections were prepared with focused ion beam milling (FIB) (FIB-SEM, SMF2000, Hitachi High-Tech Science, Japan). The thermal stability was studied by thermogravimetric analysis (TGA, DTG-60 H, Shimadzu, Japan) between 30 and 500 ℃ with a heating rate of 5 ℃ min^{-1}. The polymer-in-ceramic films were also subjected to a burning test with an alcohol lamp. The electrolyte contact angle was measured using a digital microscope (Sato Shoji INC. Japan). The theoretical density of the film was calculated based on the mixture rule. In contrast, the real density was determined by the ratio between the mass and dimension of the film. The porosity was the ratio of the real density to the theoretical density.

4.3.3 Electrochemical measurement

The polymer-in-ceramic films were soaked in 1 M $LiPF_6$/EC: DEC (1:1) electrolyte for 2 h in a vacuum for electrolyte impregnation. AC electrochemical impedance spectroscopy (EIS) was conducted between 1 MHz to 0.1 Hz with a perturbation of 20 mV on a potentiostat (Biologic SP-300, France). Both sides of the polymer-in-ceramic films were sputtered with a thin Au layer for the EIS measurement before liquid electrolyte impregnation. The ionic current was 3.5 mA, and

the sputtering time was 1 h for each side. The electrochemical performance of the polymer-in-LLZO separator was evaluated in an NCM811|Li cell with a 1 M $LiPF_6$/EC: DEC (1:1) electrolyte and was compared with that of a PP separator, Celgard 2400. Galvanostatic cycling was carried out between 2.5 and 4.2 V. The NCM811 cathode slurry was prepared by mixing an NCM811 powder (Beijing Easpring Material Technology Co., Ltd, China), acetylene black (AB), and polyvinylidene difluoride (PVDF) (w:w:w=92:4:4) in N-methyl-2-pyrrolidone (NMP). The slurry was then cast onto an Al foil (20 μm thick) to prepare the cathode layer. The NCM811 cathode layer was dried at 80 °C in a vacuum oven for 8 h before coin cell assembly (CR2032), and the active material loading was about 5.0 mg cm^{-2}. A Li@Cu foil (Li layer thickness: 20 μm, Honjo Metal Co., Ltd., Osaka, Japan) was used as the anode.

4.4 Results and discussions

4.4.1 Tape casting of flexible polymer-in-ceramic thin films

The polymer-in-ceramic thin films were tape cast using a doctor blade in an ambient environment, as shown in Fig. 4.1(a). After vacuum-drying at room temperature, they could be easily stripped off the PET substrate, showing good mechanical stability (Fig. 4.1(b)). In addition, the as-dried films were self-standing and could be folded and twisted without breaking, demonstrating high flexibility, although the Al_2O_3 or LLZO content in the polymer-in-ceramic films was as high as 87.0 wt% (Figs. 4.1(c) and (d)). The room-temperature synthesis of the flexible polymer-in-ceramic thin films was simple and suitable for industrial production. Although the Al_2O_3 and LLZO powders were similar in particle size and were processed using the same parameters, the LLZO slurry was more viscous than the Al_2O_3 slurry and was difficult to form films as thin as 25 μm (although possible). The difference in the slurry viscosity could be attributed to the difference in particle morphology. The Al_2O_3 particles were spheres, while the LLZO

secondary particles were irregular in shape and very porous (Figs. 4.1 (e) and (f)). In addition, the surface chemistry of the two powders was very different, which would also affect the slurry viscosity. Additionally, the elastomeric binder showed a higher affinity to the Al_2O_3 particles than to the LLZO particles, rendering the Al_2O_3 film with higher mechanical properties and less porous than the LLZO film. As a result, the LLZO film was prepared with a thickness of 75 μm, considering the castability of the LLZO slurry and the mechanical robustness of the as-cast LLZO film.

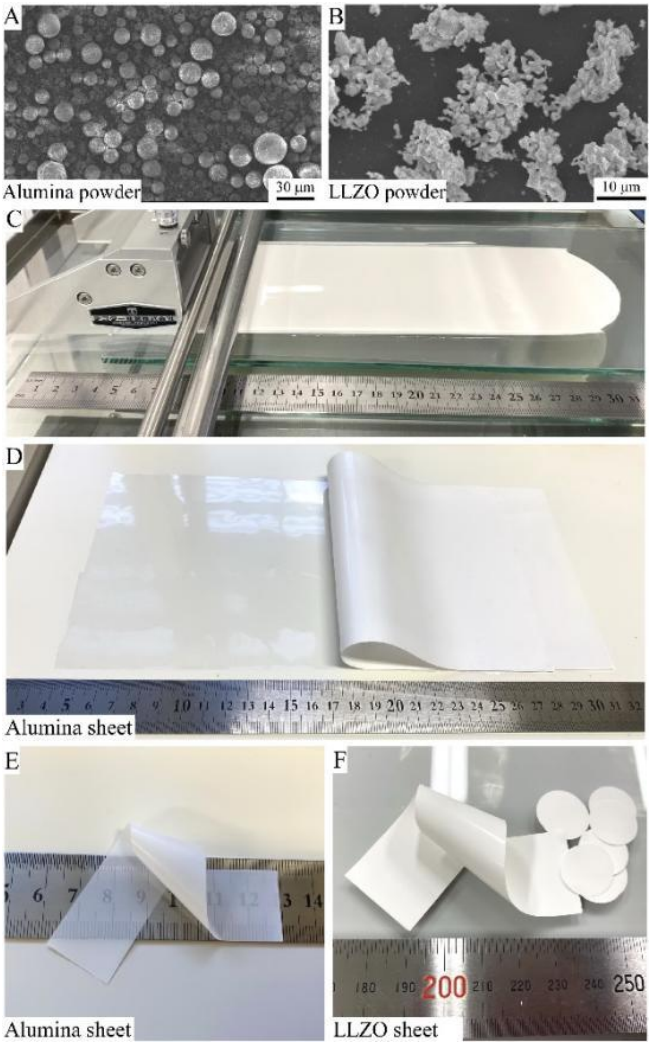

Fig. 4.1 Optical images of polymer-in-ceramic (Al_2O_3 or LLZO) thin films. (a) and (b) Al_2O_3 and LLZO starting powders used for the film casting, (c) An as-cast film in an ambient environment,

(d) An as-dried film that could be stripped off from the PET substrate demonstrating good mechanical stability, (e) and (f) As-dried polymer-in-Al_2O_3 and polymer-in-LLZO films, demonstrating good flexibility. The Al_2O_3-based film is about 25 μm in thickness, and the LLZO-based film is about 75 μm.

4.4.2 SEM micrographs of the polymer-in-ceramic thin films

SEM micrographs of the as-dried polymer-in-ceramic thin films are shown in Fig. 4.2. The Al_2O_3-based film was about 20 to 26 μm thick (Fig. 4.2(a)), and shallow pores on the surface were observed (Fig. 4.2(b)). The elastomeric binder firmly bonded the Al_2O_3 particles, and the pores inside the film were isolated when viewed from the cross-section milled by FIB (Fig 4.2. (c)). The porosity of polymer-in-Al_2O_3 thin film was estimated to be around 24.4%, unsuitable for use as a separator for Li-ion batteries. On the other hand, the polymer-in-LLZO film was more porous (Figs. 4.2 (d), (e), and (f)), and the internal pores were interconnected (Fig. 4.2(f)). The porosity of the polymer-in-LLZO film was estimated to be 50%, even higher than that of Celgard 2400 (about 40%) [2].

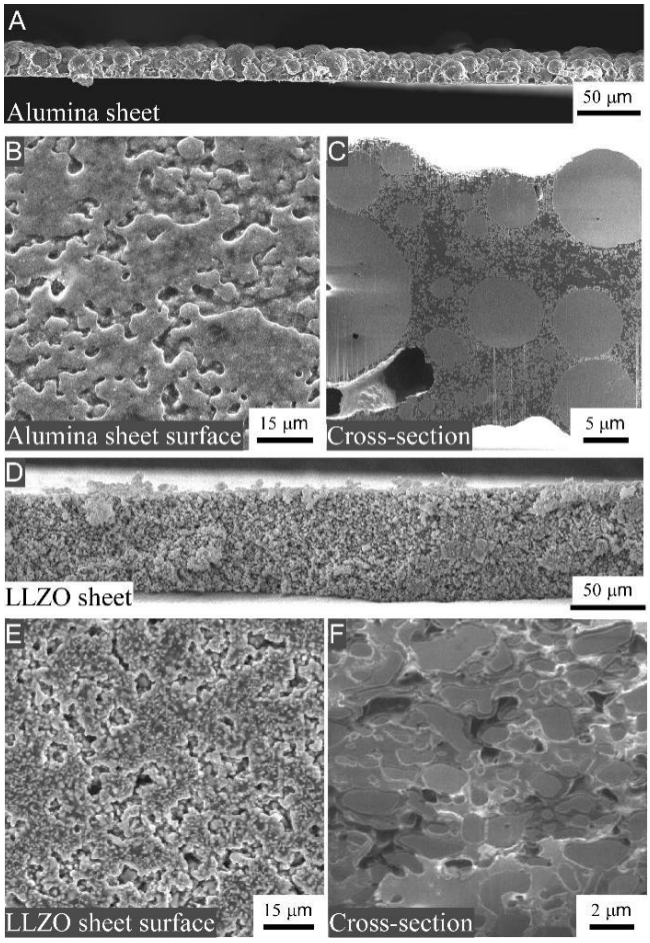

Fig. 4.2 SEM micrographs of the as-dried polymer-in-ceramic thin films. (a) Cross-section of the polymer-in-Al_2O_3 film, (b) Surface of the polymer-in-Al_2O_3 film, (c) Cross-section of the polymer-in-Al_2O_3 film milled by FIB, (d) Cross-section of the polymer-in-LLZO film, (e) Surface of the polymer-in-LLZO film, (f) Cross-section of the polymer-in-LLZO film milled by FIB.

4.4.3 Thermal stability of the polymer-in-ceramic thin films

TGA measurement was performed in dry air to study the thermal stability of the polymer-in-ceramic thin films. (Fig. 4.3). Celgard 2400 was used as a reference for comparison, whose thermal degradation roughly started from 240 °C (Fig. 4.3(a)). The sharp weight loss of Celgard 2400 could be attributed to the depolymerization of polypropylene. Similarly, the polymer-in-Al_2O_3 film began

to degrade thermally around 238 ℃ but more benignly (Fig. 4.3(b)). However, the onset temperature of thermal degradation for the polymer-in-LLZO film was 325 ℃ (Fig. 4.3(c)), indicating that the polymer-in-LLZO film had higher thermal stability than both Celgard 2400 and the polymer-in-Al_2O_3 film. The volume fraction of the ceramic particles was larger in the LLZO film than in the Al_2O_3 film. In addition, the LLZO film was more porous than the Al_2O_3 film. Thus, the thermal decomposition behavior (such as the onset temperature and degradation rate) was likely affected by both the ceramic particle's volume fraction and the film's porosity. The mass loss was only about 10% for both the polymer-in-ceramic films when heated to 400 ℃. On the other hand, the Celgard 2400 separator was almost completely vaporized. As shown in Figs. 4.3(d)-(f), the flame propagation of the polymer-in-ceramic films was less pronounced than that of Celgard 2400 when subjected to alcohol flame. Moreover, the polymer-in-ceramic films maintained structural integrity after combustion because of the ceramic skeletons (Figs. 4.3 (g)-(i)), enabling them to suppress thermal runaway propagation in the case of fire. In contrast, the Gelgard 2400 separator was burnt into ashes after 3 s.

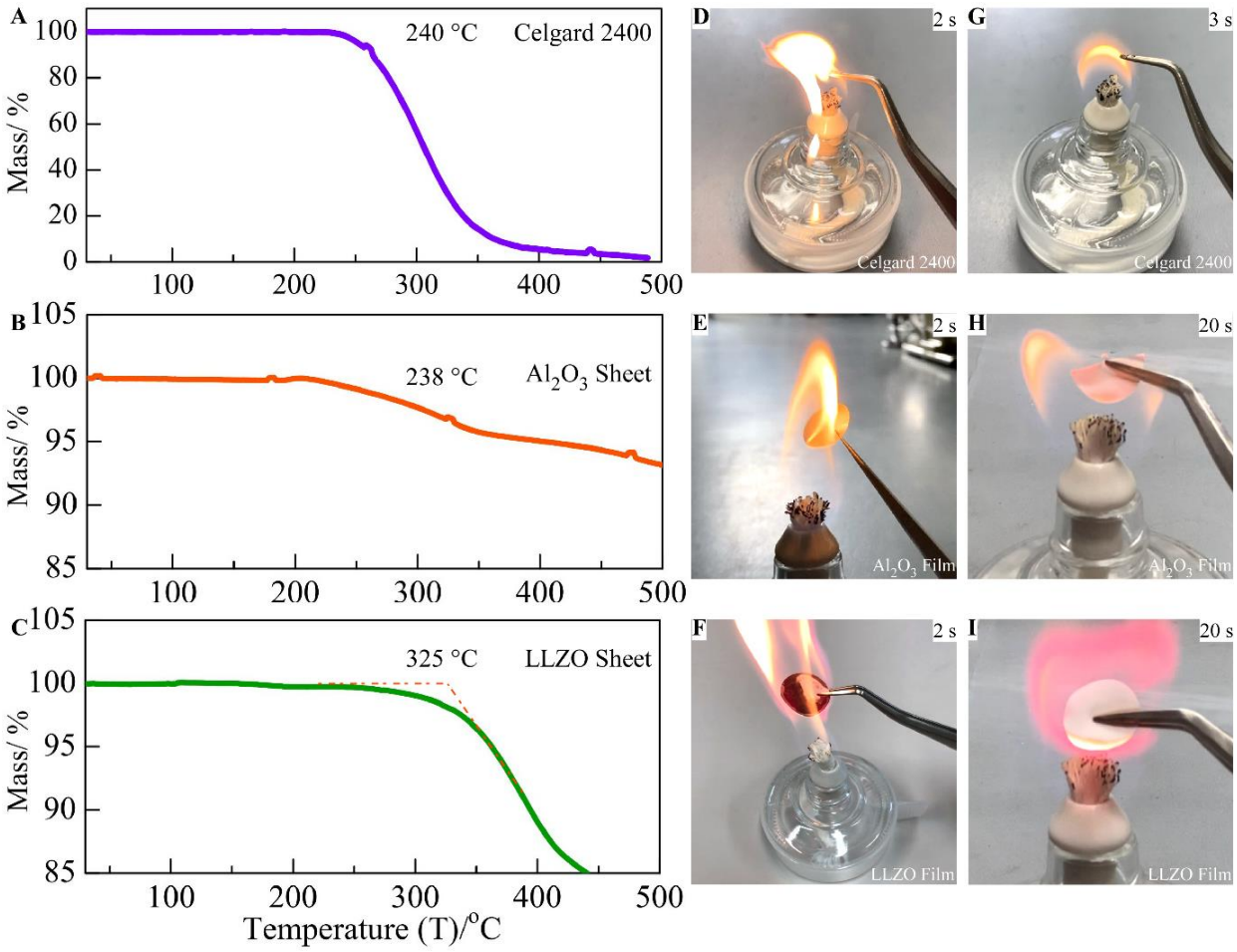

Figure. 4.3 Thermal stability and flammability tests of Celgard 2400 and the polymer-in-ceramic thin films in air. (a), (d) and (g) Celgard 2400, (b), (e) and (h) polymer-in-Al_2O_3 film, (c), (f) and (i) polymer-in-LLZO film.

4.4.4 Wettability of the polymer-in-ceramic thin films

Wettability is an important parameter of separators. Thus, for comparison, electrolyte contact angle measurements were carried out on the polymer-in-ceramic thin films and Celgard 2400. The electrolyte contact angle of Celgard 2400 was about 43.3° (Fig. 4.4(a)), while that of the polymer-in-Al_2O_3 thin film was about 38.4° (Fig. 4.4(b)). In the case of the polymer-in-LLZO film, the electrolyte contact angle was only 19.6° (Fig. 4.4(c)), much smaller than that of Celgard 2400,

implying that the polymer-in-LLZO film had better wettability with the electrolyte than Celgard 2400. Moreover, the electrolyte was spread over the polymer-in-LLZO film's surface after 5 s. Since the polymer-in-LLZO film was prepared in ambient conditions, carbonate contamination on LLZO was unavoidable [21, 22], which was supposed to decrease the electrolyte wettability of the polymer-in-LLZO separator.

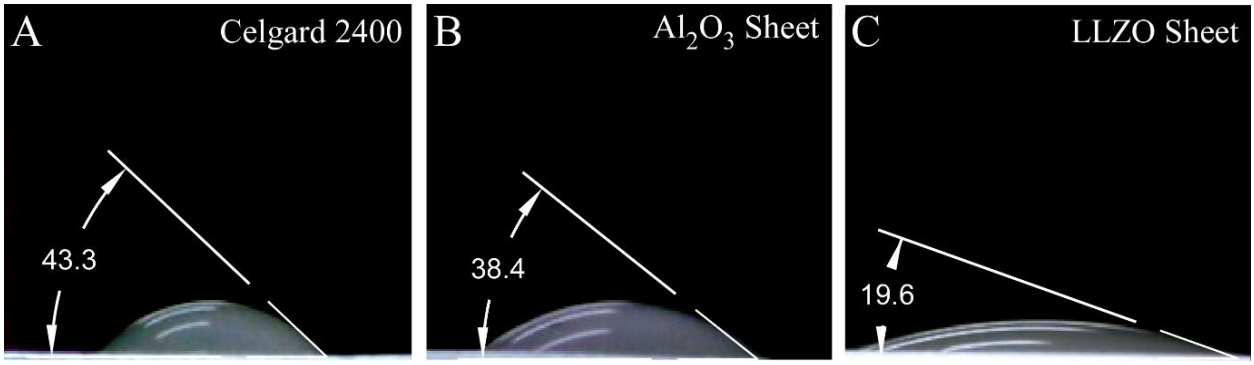

Fig. 4.4 Electrolyte (1 M $LiPF_6$/EC: DEC (1:1)) contact angle measurements of Celgard 2400 and the polymer-in-ceramic thin films (Temperature: 20 ℃. Volume of the electrolyte droplet: 1 μL).

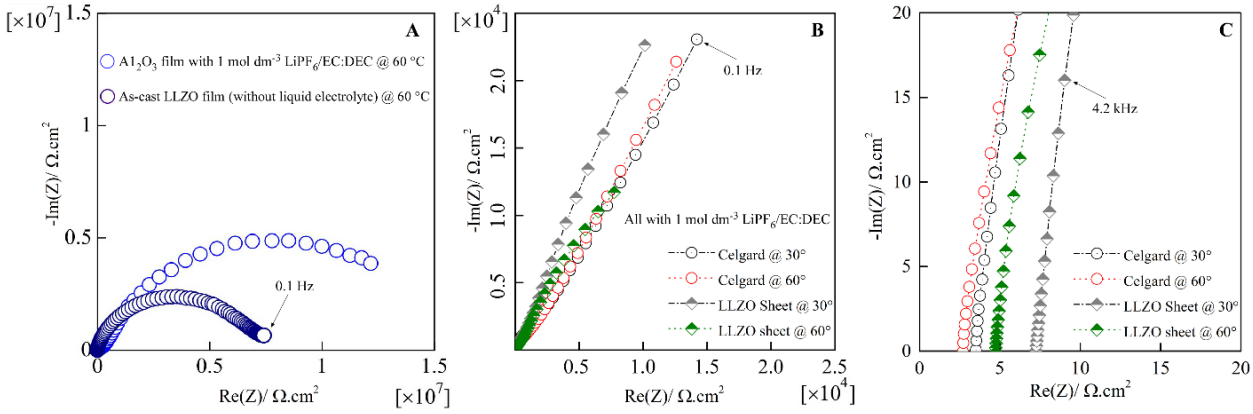

Fig. 4.5 EIS of the polymer-in-ceramic thin films. (a) EIS spectra of the as-cast LLZO-based film and the liquid electrolyte-impregnated Al_2O_3-based film at 60 ℃, (b) EIS spectra of the liquid

electrolyte-impregnated LLZO-based film (75 μm thick) and the Celgard 2400 separator (25 μm) at 30 and 60 ℃, (c) EIS of spectra shown in (b) at high-frequency regions

4.4.5 Ionic conductivity of the polymer-in-ceramic thin films

The ionic conductivity σ of the polymer-in-ceramic thin films is calculated using the following equation (Eq. (4.1)),

$$\sigma = \frac{L}{RA} \qquad (4.1)$$

where L is the thickness of the film, R is the resistance, and A the active electrode area. The as-cast LLZO-based film almost behaved like a parallel combination of a capacitor and a resistor (Fig. 5(a)) [23]. Its ionic conductivity at 60 ℃ was estimated to be 2.0×10^{-9} S cm^{-1}. The Al_2O_3-based film showed similar behavior, and its ionic conductivity at 60 ℃ was only about 2.1×10^{-10} S cm^{-1} even when impregnated with the 1 M $LiPF_6$/EC: DEC (1:1) liquid electrolyte. Thus, the liquid electrolyte uptake of the Al_2O_3-based film was negligible. On the contrary, the ionic conductivity of the LLZO-based film drastically increased when impregnated with the 1 M $LiPF_6$/EC: DEC (1:1) electrolyte and reached about 2.8×10^{-3} S cm^{-1} at 30 ℃ and 4.2×10^{-3} S cm^{-1} at 60 ℃ (Figs. 5.5(b) and (c)). In contrast, the ionic conductivity of the 1 M $LiPF_6$/EC: DEC (1:1)-impregnated Celgard 2400 separator was only 0.77×10^{-3} S cm^{-1} at 30 ℃ and 1.0×10^{-3} S cm^{-1} at 60 ℃ (Fig. 5.5(c)), much lower than that of the liquid electrolyte-impregnated LLZO-based film. This was likely because the LLZO film had a more porous structure than the Celgard 2400 separator. Besides, the LLZO skeleton could also contribute to the high ionic conductivity.

4.4.6 Electrochemical performance of the polymer-in-LLZO separator

Fig. 4.6 (a) shows the galvanostatic cycling profile of an Li|Celgard 2400|NCM811cell with a 1 M $LiPF_6$/EC: DEC (1:1) electrolyte. The discharge capacity decreased gradually with cycling, as evidenced by the increased cell resistance with cycling (Fig. 4.6(b)). The increased resistance was likely due to the solid electrolyte interphase (SEI) growth on the Li metal anode, which was related to the continuous decomposition of the electrolyte. Meanwhile, the cathode electrolyte interphase (CEI) grown on the NCM811 cathode would also increase cell resistance [24]. The initial Coulombic efficiency (ICE) of the Li|Celgard 2400|NCM811cell was 88.2%, while the Coulombic efficiency (CE) was stabilized at about 99.5 % since the second cycle (Fig. 4.6(c)). In contrast, the discharge capacity of the Li|polymer-in-LLZO|NCM811cell with a 1 M $LiPF_6$/EC: DEC (1:1) electrolyte decreased relatively rapidly with cycling (Fig. 4.6(d)). The EIS spectra showed that the cell resistance increased significantly with cycling (Fig. 4.6(e)). It was likely due to the reaction between LLZO and the liquid electrolyte, leading to the formation of Li_2CO_3, Li_2O, LiF, etc., and increasing electrochemical charge transfer resistance significantly [25, 26]. Although the ICE of the Li|polymer-in-LLZO|NCM811cell was 88.9% (Fig. 4.6(f)), the average CE was much lower than that of the Li|Celgard 2400|NCM811cell.

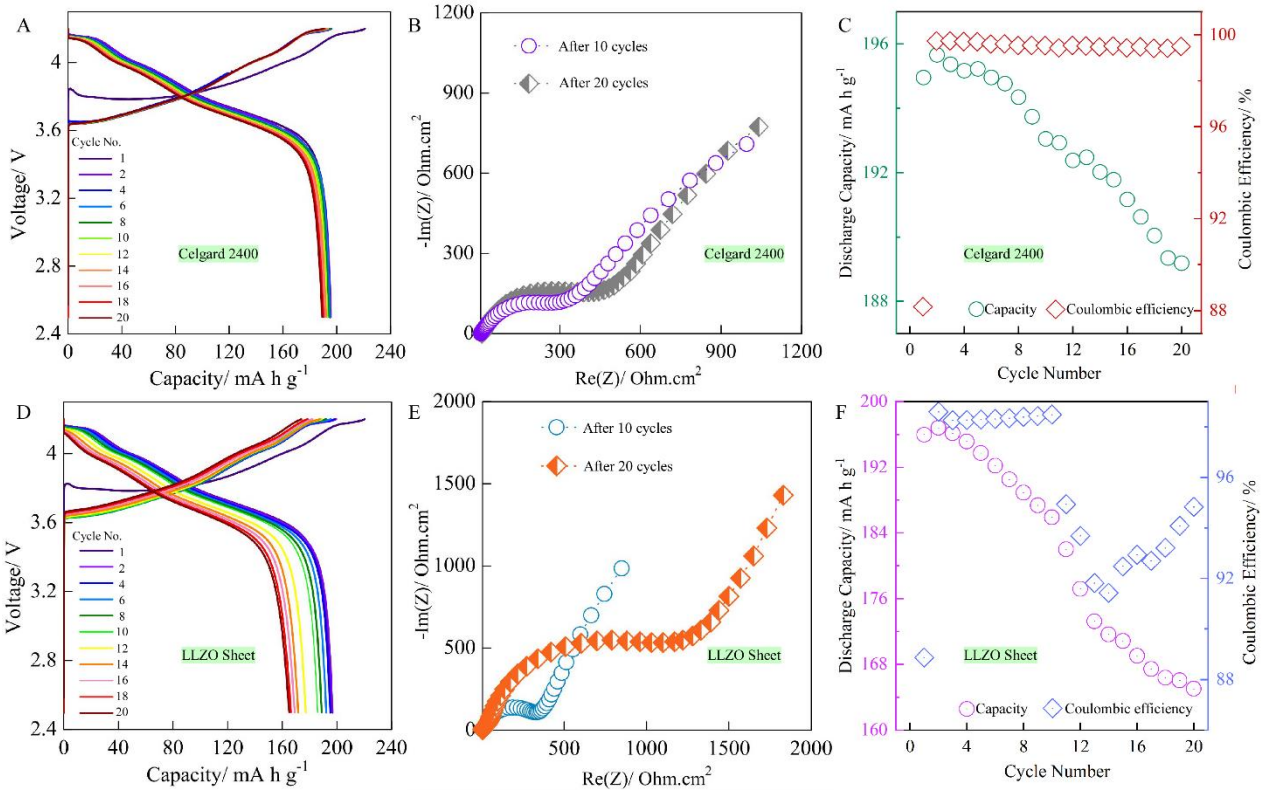

Fig. 4.6 Electrochemical performance of the polymer-in-LLZO separator at 30 ºC. (a) Galvanostatic cycling profile of the Li|Celgard 2400|NCM811cell with a 1 M $LiPF_6$/EC: DEC (1:1) electrolyte. The C-rate is 0.1 C, and the temperature is 30 ºC, (b) EIS spectra of the Li|Celgard 2400|NCM811cell, (c) Capacity retention and Coulombic efficiency of the Li|Celgard 2400|NCM811cell, (d) Galvanostatic cycling (0.1 C) profile of the Li|polymer-in-LLZO|NCM811cell with the 1 M $LiPF_6$/EC: DEC (1:1) electrolyte, (e) EIS spectra of the Li|polymer-in-LLZO|NCM811cell, (f) Capacity retention and Coulombic efficiency of the Li|polymer-in-LLZO|NCM811cell.

4.5 Conclusions

A polymer-in-LLZO thin-film separator was prepared by tape casting at room temperature. The thickness and porosity of the polymer-in-LLZO separator were about 75 μm and 50%, respectively. It showed better wettability with the commercial liquid electrolyte of 1 M $LiPF_6$/EC: DEC (1:1), higher thermal stability, and higher ionic conductivity than the PP separator Celgard 2400. However, its electrochemical performance in the NCM811|Li cell was not as good as Celgard 2400. The main reason was likely due to the reaction between LLZO and the 1 M $LiPF_6$/EC: DEC (1:1) electrolyte.

Further development is needed to improve the stability of the polymer-in-LLZO separator against commercial liquid electrolytes. Meanwhile, a 25 μm-think polymer-in-Al_2O_3 film was prepared similarly. However, its porosity was only about 24%, and the pores were isolated, making it more suitable as a good flexible electrical insulator for electronics rather than a separator for Li-ion batteries.

Reference

[1] Melin, H.E., M.A. Rajaeifar, A.Y. Ku, A. Kendall, G. Harper, O. Heidrich (2021), Global implications of the EU battery regulation, Science, 373: 384-387.

[2] Martinez-Cisneros, C., C. Antonelli, B. Levenfeld, A. Varez, J. Sanchez (2016), Evaluation of polyolefin-based macroporous separators for high temperature Li-ion batteries, Electrochimica Acta, 216: 68-78.

[3] Liu, J., Y. Liu, W. Yang, Q. Ren, F. Li, Z. Huang (2018), Lithium ion battery separator with high performance and high safety enabled by tri-layered SiO_2@ PI/m-PE/SiO_2@ PI nanofiber composite membrane, Journal of Power Sources, 396: 265-275.

[4] Jang, J., J. Oh, H. Jeong, W. Kang, C. Jo (2020), A review of functional separators for lithium metal battery applications, Materials, 13: 4625.

[5] Qiu, Z., S. Yuan, Z. Wang, L. Shi, J.H. Jo, S.T. Myung, J. Zhu (2020), Construction of silica-oxygen-borate hybrid networks on Al_2O_3-coated polyethylene separators realizing multifunction for high-performance lithium ion batteries, Journal of Power Sources, 472: 228445.

[6] Syzdek, J., M. Armand, M. Gizowska, M. Marcinek, E. Sasim, M. Szafran, W. Wieczorek (2009), Ceramic-in-polymer versus polymer-in-ceramic polymeric electrolytes—A novel approach, Journal of Power Sources, 194: 66-72.

[7] Augustin, S., V. Hennige, G. Hörpel, C. Hying (2002), Ceramic but flexible: new ceramic membrane foils for fuel cells and batteries, Desalination, 146: 23-28.

[8] Jiang, H., Y. Wu, J. Ma, Y. Liu, L. Wang, X. Yao, H. Xiang (2021), Ultrathin polymer-in-ceramic and ceramic-in-polymer bilayer composite solid electrolyte membrane for high-voltage lithium metal batteries, Journal of Membrane Science, 640: 119840.

[9] Chen, L., Y. Li, S.P. Li, L.Z. Fan, C.W. Nan, J.B. Goodenough (2018), PEO/garnet composite electrolytes for solid-state lithium batteries: From "ceramic-in-polymer" to "polymer-in-ceramic", Nano Energy, 46: 176-184.

[10] Murugan, R., V. Thangadurai, W. Weppner (2007), Fast lithium ion conduction in garnet-type $Li_7La_3Zr_2O_{12}$, Angewandte Chemie International Edition, 46: 7778-7781.

[11] Chan, C.K., T. Yang, J.M. Weller (2017), Nanostructured garnet-type $Li_7La_3Zr_2O_{12}$: synthesis, properties, and opportunities as electrolytes for Li-ion batteries, Electrochimica Acta, 253: 268-280.

[12] Subramanian, K., G.V. Alexander, K. Karthik, S. Patra, M. Indu, O. Sreejith, R. Viswanathan, J. Narayanasamy, R. Murugan (2021), A brief review of recent advances in garnet structured solid electrolyte based lithium metal batteries, Journal of Energy Storage, 33: 102157.

[13] Yu, S., R.D. Schmidt, R. Garcia-Mendez, E. Herbert, N.J. Dudney, J.B. Wolfenstine, J. Sakamoto, D.J. Siegel (2016), Elastic properties of the solid electrolyte $Li_7La_3Zr_2O_{12}$ (LLZO), Chemistry of Materials, 28: 197-206.

[14] Yu, X., A. Manthiram (2021), A review of composite polymer-ceramic electrolytes for lithium batteries, Energy Storage Materials, 34: 282-300.

[15] Parikh, D., T. Christensen, C.T. Hsieh, J. Li (2019), Elucidation of separator effect on energy density of Li-ion batteries, Journal of The Electrochemical Society, 166: A3377.

[16] Liu, Z., Y. Jiang, Q. Hu, S. Guo, L. Yu, Q. Li, Q. Liu, X. Hu (2021), Safer Lithium-Ion Batteries from the Separator Aspect: Development and Future Perspectives, Energy & Environmental Materials, 4: 336-362.

[17] Yang, Y., Y. Wu (2014), Tape-casted transparent alumina ceramic wafers, Journal of Materials Research, 29: 2312-2317.

[18] Stastny, P., Z. Chlup, K. Castkova, M. Trunec (2021), High strength alumina tapes prepared by gel-tape casting method, Ceramics International, 47: 6988-6995.

[19] Cheng, E.J., M. Liu, Y. Li, T. Abe, K. Kanamura (2022), Effects of porosity and ionic liquid impregnation on ionic conductivity of garnet-based flexible sheet electrolytes, Journal of Power Sources, 517: 230705.

[20] Cheng, E.J., T. Kimura, M. Shoji, H. Ueda, H. Munakata, K. Kanamura (2020), Ceramic-based flexible sheet electrolyte for Li batteries, ACS Applied Materials & Interfaces, 12: 10382-10388.

[21] Yamada, H., T. Ito, S.P. Kammampata, V. Thangadurai (2020), Toward understanding the reactivity of garnet-type solid electrolytes with H_2O/CO_2 in a glovebox using X-ray photoelectron spectroscopy and electrochemical methods, ACS applied materials & interfaces, 12: 36119-36127.

[22] Sharafi, A., E. Kazyak, A.L. Davis, S. Yu, T. Thompson, D.J. Siegel, N.P. Dasgupta, J. Sakamoto (2017), Surface chemistry mechanism of ultra-low interfacial resistance in the solid-state electrolyte $Li_7La_3Zr_2O_{12}$, Chemistry of Materials, 29: 7961-7968.

[23] Huggins, R., Advanced batteries: materials science aspects, Springer Science & Business Media2008.

[24] Fan, X., C. Wang (2021), High-voltage liquid electrolytes for Li batteries: progress and perspectives, Chemical Society Reviews.

[25] Cheng, E.J., M. Shoji, T. Abe, K. Kanamura (2022), Ionic liquid-containing cathodes empowering ceramic solid electrolytes, Iscience, 25: 103896.

[26] Liu, J., X. Gao, G.O. Hartley, G.J. Rees, C. Gong, F.H. Richter, J. Janek, Y. Xia, A.W. Robertson, L.R. Johnson (2020), The interface between $Li_{6.5}La_3Zr_{1.5}Ta_{0.5}O_{12}$ and liquid electrolyte, Joule, 4: 101-108.

Chapter 5 Preparation of quasi-solid-state composite cathode

5.1 Abstract

Although ceramic solid electrolytes, such as $Li_7La_3Zr_2O_{12}$ (LLZO), are promising candidates to replace conventional liquid electrolytes for developing safe and high-energy-density solid-state Li-metal batteries, the large interfacial resistance between cathodes and ceramic solid electrolytes severely limits their practical application. Here we developed an ionic liquid (IL)-containing while non-fluidic quasi-solid-state $LiCoO_2$ (LCO) composite cathode, which can maintain good contact with an Al-doped LLZO (Al-LLZO) ceramic electrolyte. The interfacial resistance between LCO and Al-LLZO has significantly decreased accordingly. Quasi-solid-state Li/Al-LLZO/LCO cells demonstrated relatively high-capacity retention of about 80% after 100 cycles at 60 °C. The capacity decay was mainly due to the instability of the IL. Nevertheless, IL therapy offers a simple and practical approach to addressing the interfacial resistance issue in ceramic-based solid-state Li batteries. Identifying a suitable IL is critical for developing quasi-solid-state Li-metal batteries with a ceramic solid electrolyte.

5.2 Introduction

Owing to the unmatched energy density, rechargeable Li-ion batteries have dominated the portable electronics market for three decades since their first commercialization by Sony in 1991 [1]. However, the emerging electric vehicle (EV) industry is concerned with maximizing the driving range and improving vehicle safety [2-3]. Advanced batteries are critical for EVs and essential in integrating renewable energy resources, such as wind and solar energies, into the electric power grid to supplement the growing energy demand worldwide. Since a Li metal anode has an ultrahigh theoretical specific capacity of 3860 mA h g^{-1} (about 10 times higher than that of a graphite anode) and the most negative redox potential of -3.04 V *vs*. standard hydrogen electrode

(SHE), Li-metal batteries have regained tremendous research interest recently as promising next-generation energy storage devices [4].

However, the practical use of Li metal anode is challenging because of uncontrollable Li dendrite growth and severe side reactions between Li metal and conventional liquid electrolytes. Li metal was first reported to be used as an anode material in the TiS_2-Li rechargeable battery in 1976 by Stanley Whittingham but was abandoned after that due to severe Li dendrite growth [5], which not only caused rapid capacity decay but also posed an explosion hazard. Unlike liquid electrolytes, solid electrolytes have the potential to physically suppress the initiation and propagation of Li dendrite growth because they have relatively high elastic and shear moduli [6-8]. Though many solid electrolytes exhibit fast-ion conductivity (e.g., 10^{-3} S cm^{-1} at 25 °C), few are stable against Li metal. The garnet-type solid electrolyte, LLZO, is widely regarded as a promising solid electrolyte due to its high ionic conductivity and chemical stability against Li metal [9-10]. Although sulfide solid electrolytes, such as Li_2S-P_2S_5, usually have higher ionic conductivities than LLZO, they must be handled in air-free conditions because hydrolysis of sulfide electrolytes by water vapor in air generates smelly and toxic H_2S gas [11]. In comparison, LLZO is relatively stable in air, odorless, and non-flammable.

Nonetheless, it is difficult to form good interfacial contact between LLZO and electrode materials because high-temperature sintered LLZO is rigid and brittle (Vickers hardness: ~6.3 GPa) [7, 12-13]. This results in high interfacial resistance, preventing the practical use of LLZO as a promising solid electrolyte [14-15]. A tremendous research effort has been devoted to reducing the high interfacial resistance in solid-state Li metal batteries with an LLZO electrolyte. For example, ultra-low interfacial resistance, as low as 1 Ω cm^2, could be achieved by introducing a thin Au, Ag, ZnO, or Al_2O_3 interlayer into the LLZO/Li interface [16-20]. Good contact between

LLZO and Li metal can also be achieved by high pressure and heat treatment [21-23], because Li metal is soft and has a relatively low melting point of 180.5 °C. In contrast, much less effort has been devoted to reducing the interfacial resistance between LLZO and the cathode materials. Although good interfacial bonding between LLZO and LCO could be achieved by co-sintering [24], LCO is likely to decompose at temperatures greater than 900 °C [25], and Li loss and various side reactions are also expected to occur at high temperatures.

A convenient and effective way to construct a conformal interface for fast Li-ion transport is to introduce a small amount of liquid electrolyte to wet the cathode/solid electrolyte interface [26-27]. Since room temperature ILs are highly conductive, thermally stable, almost non-volatile, and non-flammable, they are ideal candidates for wetting the cathode/solid electrolyte interface [28]. For example, LCO/Li cells with a quasi-solid-state IL-LLZO electrolyte demonstrated a high initial discharge capacity of 130 mA h g^{-1} and high-capacity retention of 99% after 150 cycles [29]. However, the quasi-solid-state IL-LLZO electrolyte was fragile and difficult to handle. Similarly, an IL can be introduced into the cathode to form a quasi-solid-state composite cathode. A conventional cathode slurry usually consists of an active material (e.g., LCO), a polymer binder (e.g., polyvinylidene difluoride (PVDF)), a conductive agent (e.g., acetylene black (AB)), and a solvent (e.g., N-methyl-2-pyrrolidone (NMP)). After the evaporation of NMP, the physical contact between an LCO cathode and an LLZO electrolyte would mainly be point-to-point contact, as illustrated in Figure 5.1(a). However, the cathode/solid electrolyte interface can be wetted by a small amount of IL, which can be introduced into the cathode during slurry casting (Fig. 5.1(b)). Adding a small amount of IL into the cathode slurry during cathode preparation will only slightly change the rheological behavior of the cathode slurry but without changing the existing battery manufacturing infrastructure. To our knowledge, few works have explored the potential of an IL-

containing composite cathode for developing solid-state Li metal batteries [19, 30-32].

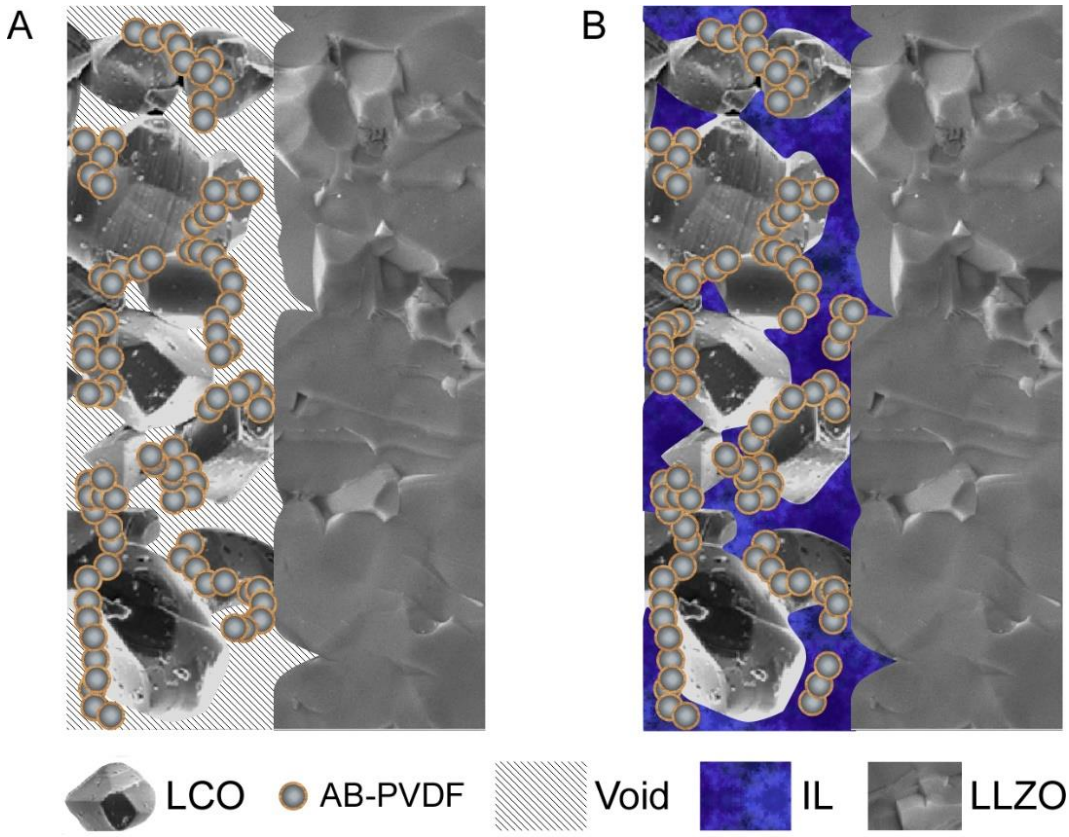

Figure 5.1. Illustration of an LCO cathode with and without an IL. (a) without an IL, (b) with an IL. The IL wets the LCO/LLZO interface.

Our research has attempted to address the primary challenge of the cathode/solid electrolyte interfacial resistance in garnet-based solid-state Li-metal batteries. This paper presents an alternative strategy for reducing the cathode/solid electrolyte interfacial resistance by developing an IL-containing quasi-solid-state composite cathode. Introducing an IL into the LCO cathode effectively reduced the LCO/Al-LLZO interfacial resistance. The effects of IL type and content on the electrochemical behavior of the quasi-solid-state LCO cathode were systematically studied. We showed that IL therapy was a convenient and effective way to reduce the cathode/solid electrolyte interfacial resistance. It is also highly compatible with the existing battery manufacturing process.

5.3 Results and Discussion

5.3.1 Electrochemical properties of two selected ILs and the Al-LLZO pellet

Two ILs were used to develop the IL-containing quasi-solid-state composite LCO cathode. One was a solvate IL, Li(G4)FSI, designated as GF, which was prepared by dissolving lithium bis(fluorosulfonyl)imide (LiFSI) in equimolar tetraethylene glycol dimethyl ether (G4) [27, 33]. Another one was a conventional IL, 1 mol dm^{-3} LiTFSI/EMI-TFSI, designated as ET, which was prepared by dissolving lithium bis(trifluoromethylsulfonyl)imide (LiTFSI) in 1-ethyl-3-methylimidazolium bis(trifluoromethylsulfonyl)imide (EMI-TFSI). As shown in Figure 5.2, the electrochemical stability of GF, ET, and the Al-LLZO pellet was studied by linear sweep voltammetry (LSV) and cyclic voltammetry (CV). The ionic conductivity in the temperature range of 30-80 °C was measured by electrochemical impedance spectroscopy (EIS). An Au foil was used as the working electrode (WE), and a Li foil was used as the counter electrode (CE) as well as the reference electrode (RE) for the LSV and CV measurements.

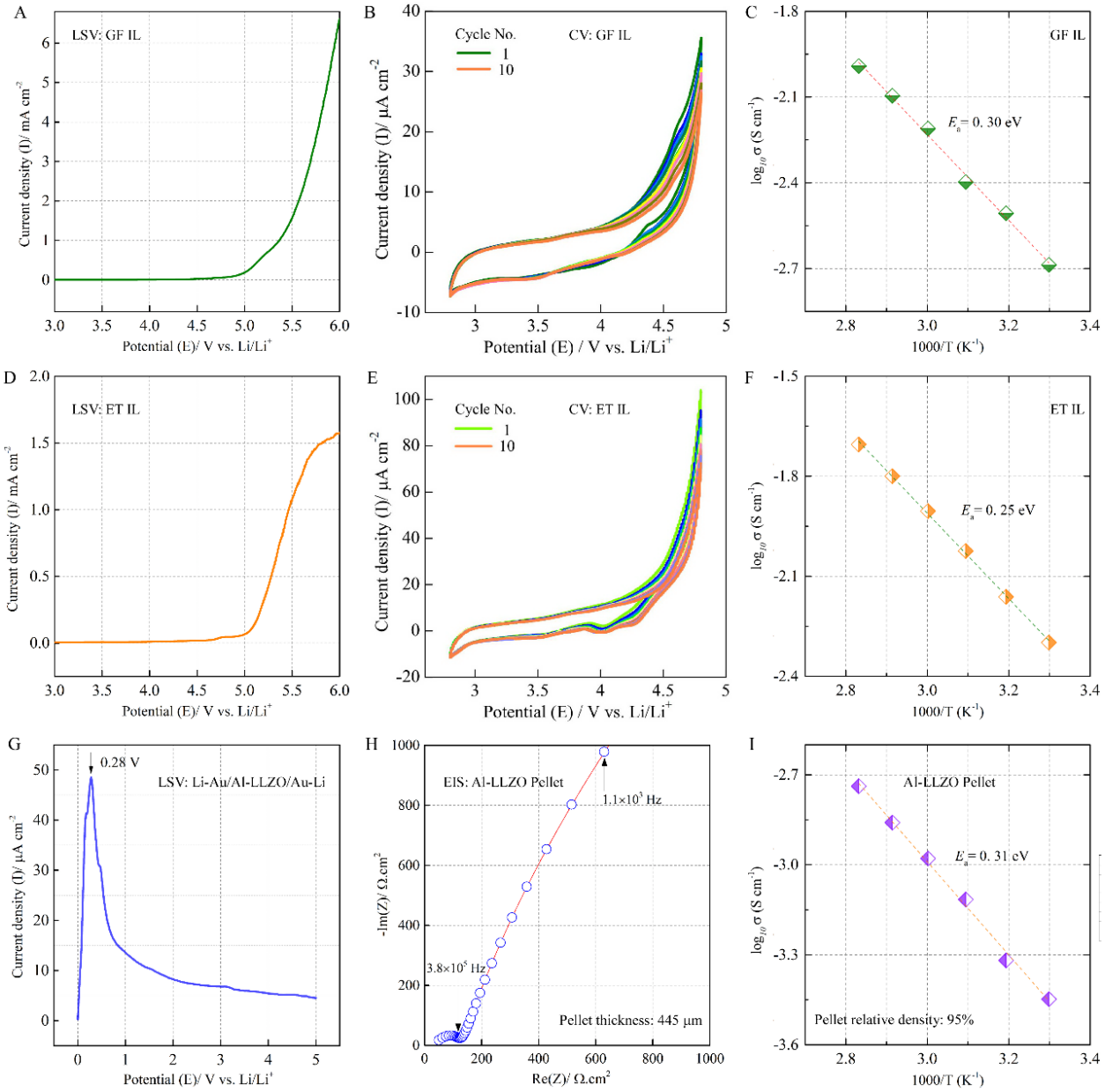

Figure 5.2. Electrochemical properties of the two selected ILs and the Al-LLZO pellet. (a) Linear sweep voltammogram of GF, (b) Cyclic voltammogram of GF, (c) Arrhenius conductivity of GF, (d) Linear sweep voltammogram of ET, (e) Cyclic voltammogram of ET, (f) Arrhenius conductivity of ET. An Au foil was used as the WE, and a Li foil was used as both the CE and the RE. A highly porous polyimide film (PI) was used as the separator. The scan rates for the LSV and CV measurements were 1 mV s^{-1}, (g) Linear sweep voltammogram of a Li/Al-LLZO/Li symmetric

cell at a scan rate of 1 mV min^{-1}, (h) EIS spectrum of the Al-LLZO pellet at 30 °C, (i) Arrhenius conductivity of the Al-LLZO pellet. All the CV and LSV measurements were carried out at 30 °C.

GF showed good anodic stability up to 4.5 V vs. Li/Li^+ because the anodic current was almost negligible (less than 0.025 mA cm^{-2}) at potentials below 4.5 V vs. Li/Li^+ (Figure 5.2(a)). The drastic increase of the current density at potentials above 5.0 V vs. Li/Li^+ indicated strong oxidation of GF. As shown in Figure 5.2(b), no noticeable redox peaks are observed from the CV curves in the potential range of 2.8–4.8 V vs. Li/Li^+, proving that GF has a relatively wide electrochemical window. The ionic conductivity of GF was 2.1 $\times 10^{-3}$ S cm^{-1} at 30 °C and 6.2 $\times 10^{-3}$ S cm^{-1} at 60 °C. In general, the ionic conductivity of a liquid electrolyte will decrease when its salt concentration is greater than 1 mol dm^{-3} because of a rapid increase in viscosity [34]. The salt concentration in GF was as high as 4.5 mol dm^{-3}. As a comparison, the ionic conductivity of the commercial liquid electrolyte, 1 mol dm^{-3} $LiPF_6$/EC: DMC (v:v=1:1), was about 1.1 $\times$ 10^{-2} S cm^{-1} at 30 °C, much higher than that of GF. The temperature dependence of the ionic conductivity was fitted with the Arrhenius equation:

$$\sigma(T) = \sigma_0 \exp[-E_a/(RT)] \qquad (5\text{-}1)$$

where σ is the ionic conductivity, σ_0 is the pre-exponential factor (a constant with the same unit as σ), T is the absolute temperature, E_a is the activation energy, and R is the universal gas constant. The activation energy of GF was estimated to be 0.3 eV (Figure 5.2(c)).

On the other hand, a noticeable anodic current increase was observed in the LSV curve of ET at potentials slightly above 4.0 V vs. Li/Li^+, and a sharp rise in the current density occurred at potentials above 5.0 V vs. Li/Li^+ (Figure 5.2(d)). In addition, broad reduction peaks were observed in the CV curves at potentials slightly above 4.0 V vs. Li/Li^+ (Figure 5.2(e)). Thus, ET has a narrower electrochemical window than GF. The ionic conductivity of ET was 5.0 $\times 10^{-3}$ S cm^{-1} at

30 °C and 1.2 $\times 10^{-2}$ S cm^{-1} at 60 °C. The activation energy of ET was measured to be 0.25 eV (Figure 5.2(f)), lower than that of GF. Figure 5.2(g) shows the LSV profile of a Li/Al-LLZO/Li symmetric cell in the potential range of 0–5.0 V vs. Li/Li^+. A thin Au interlayer was introduced into the Li/Al-LLZO interface to reduce the interfacial resistance. Li stripping occurred at 0.28 V vs. Li/Li^+, and no other oxidation peaks were observed up to 5.0 V vs. Li/Li^+. The ionic conductivity of the Al-LLZO pellet was 3.6 $\times 10^{-4}$ S cm^{-1} at 30 °C (Figure 5.2(h)) and 1.0 $\times 10^{-3}$ S cm^{-1} at 60 °C. The activation energy of the Al-LLZO pellet was 0.31 eV (Figure 5.2(i)), which was relatively high due to the low relative density of the pellet (95%). The dependence of ionic conductivity of GF, ET, and the Al-LLZO pellet as a function of temperature was presented in Tables 5 S1-S3.

5.3.2 Improvement of interfacial contact between LCO and Al-LLZO by an IL

A conventional LCO cathode slurry was prepared by mixing an LCO powder, an AB conductive agent, and a PVDF powder in NMP. GF or ET was directly added into the conventional LCO slurry to make an IL-containing composite LCO slurry. The experimental procedure is shown in Figure. 5S1. Figure 5.3(a) shows an optical image of the IL-containing composite LCO cathode, which was directly cast onto the Al-LLZO pellet. The composite LCO cathode is quasi-solid and shows no fluidity. A cross-sectional SEM micrograph of the composite cathode is shown in Figure 5.3(b), where LCO particles are firmly embedded in a quasi-solid-state matrix consisting of GF, AB, and PVDF.

In contrast, voids and cracks are observed at the LCO/matrix interface region in a conventional LCO cathode, as indicated by the arrowheads in Figure 5.3(c). Figure 5.3(d) presents a cross-sectional SEM micrograph of the interface region between the quasi-solid-state LCO cathode and the Al-LLZO pellet. The LCO cathode layer was about 30 μm thick and formed intimate contact with the Al-LLZO pellet. Figure 5.3(e) presents a cross-sectional SEM micrograph of the interface

region between the conventional LCO cathode and the Al-LLZO pellet, where more voids are observed. Thus, introducing an IL could reduce the interfacial resistance between LCO and Al-LLZO and the internal resistance of the LCO cathode. Moreover, the interaction between GF and LCO was proved by differential scanning calorimetry (DSC) (Figure 5S2).

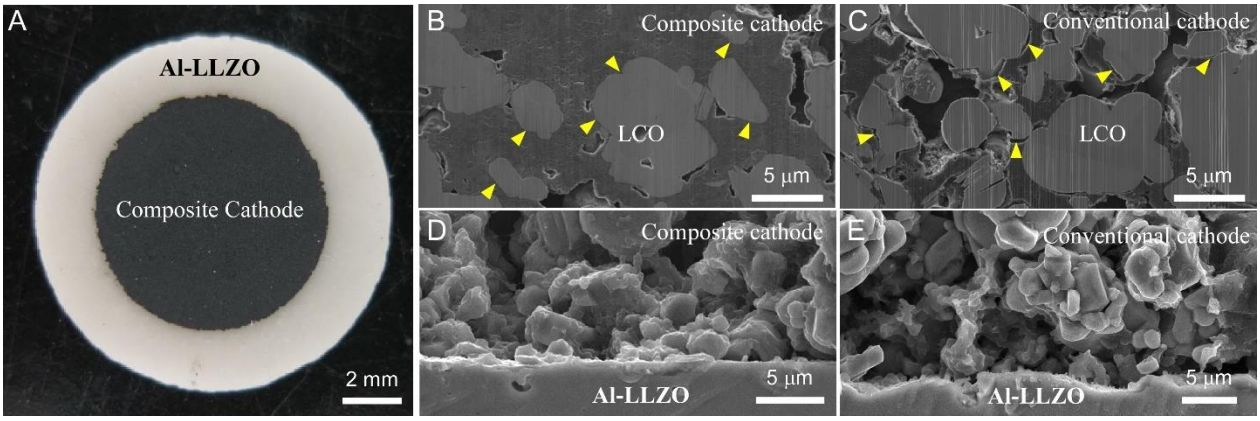

Figure 5.3. Optical and SEM images of the quasi-solid-state cathode and a conventional LCO cathode. (a) Optical image of the quasi-solid-state LCO cathode, where GF was 9.1 wt%, (b) Cross-sectional SEM micrograph of the quasi-solid-state LCO cathode, (c) Cross-sectional SEM micrograph of a conventional LCO cathode (without IL), (d) SEM micrograph of the interface region between the quasi-solid-state LCO cathode and the Al-LLZO pellet, (e) SEM micrograph of the interface region between the conventional LCO cathode and the Al-LLZO pellet. All the cross-sections were prepared by focused ion beam (FIB) milling.

5.3.3 Cycling performance of the GF-containing LCO cathode

The weight ratio of LCO: AB: PVDF: GF in the GF-containing LCO composite cathode was 92: 4: 4: *x,* where x = 0, 5, 10, 20, or 50. Accordingly, the assembled coin cells were termed GF-0, GF-5, GF-10, GF-20, and GF-50. The IL contents in the quasi-solid-state LCO cathodes in both weight and volume percentages are listed in Table 5S4. All-solid-state Li/Al-LLZO/LCO batteries cannot be reversibly charged and discharged, whereas quasi-solid-state Li/Al-LLZO/LCO batteries can.

As shown in Figure 5.4(a), the all-solid-state Li/Al-LLZO/LCO cell (x =0) reaches the cut-off voltage of 4.2 V in seconds, and no discharge occurs. This was likely due to the large interfacial resistance between the conventional LCO cathode and the Al-LLZO pellet because the anode-side interfacial resistance between Al-LLZO and Li could be reduced to as low as a few Ω cm^2 by introducing a thin Au interlayer or simply removing the common LLZO surface contaminants, such as Li_2CO_3 [17, 21, 35-36]. To reduce the cathode-side interfacial resistance, the concept of an IL-containing quasi-solid-state cathode is thus explored, and the cell configuration is illustrated in Figure 5.4(b). The GF-containing (x=5) quasi-solid-state LCO cathode can be reversibly charged and discharged (Figure 5.4(c)). The initial discharge capacity was 81.6 mA h g^{-1}, which decreased rapidly with cycling. Although the Coulombic efficiency (CE) increased upon cycling (greater than 98% after the 5^{th} cycle), the discharge capacity was only 7.8 mA h g^{-1} after 50 cycles (Figure 5.4(d)). The initial discharge capacity increased to 132.2 mA h g^{-1} at x=10 (Figure 5.4(e)), likely due to a further reduced interfacial resistance at the cathode side. Like the case of x=5, although the average CE was greater than 98%, the discharge capacity decreased quickly and was only 5.9 mA h g^{-1} after 50 cycles (Figure 5.4(f)). At x=50, the cyclability increased significantly (Figure 5.4(g)), and an average CE greater than 99% was maintained after 100 cycles (Figure 5.4(h)). However, it should be noted that the initial discharge capacity was relatively low (92.4 mA h g^{-1}), and it degraded rapidly after 50 cycles. This was likely due to the thermal instability of GF because it was electrochemically stable up to 4.5 V vs. Li/Li^+. Besides, although the solid-state LCO/Al-LLZO interface could be thoroughly wetted with excessive IL, electron transport would be blocked to some extent because the IL was electrically insulating. In addition, particle agglomeration was also likely to occur, which further reduced the utilization of LCO.

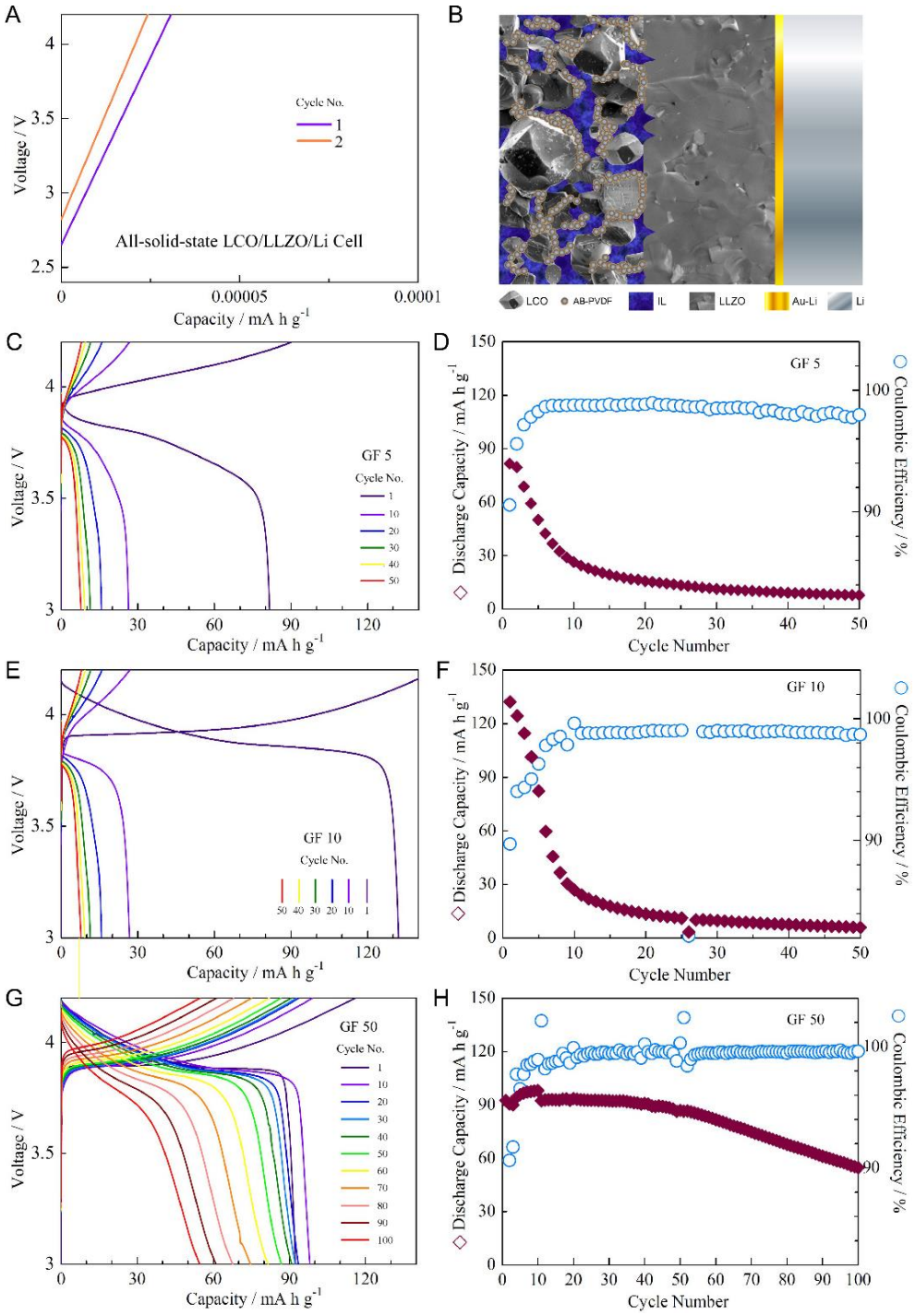

Figure 5.4. Electrochemical behavior of quasi-solid-state Li/Al-LLZO/LCO cells with different GF contents. (a) *x*=0 (all-solid-state), (b) Illustration of the configuration of the quasi-solid-state Li/Al-LLZO/LCO cell, (c) and (d) Electrochemical behavior of cell GF 5 (*x*=5), (e) and (f)

Electrochemical behavior of cell GF 10 (x=10), and (g) and (h) Electrochemical behavior of cell GF 50 (x=50). The C-rate is 0.025 C, and the cycling temperature is 60 °C.

5.3.4 Composition analysis of GF after prolonged cycling at 60 °C

One major reason for GF cell degradation was likely GF's thermal instability. The discoloration of GF evidenced this after prolonged cycling at 60 °C. Fourier-transform infrared spectroscopy (FTIR) was used to analyze the composition change of GF after cycling at 60 °C. Pristine GF was a transparent liquid, while it changed to a yellowish gel after cycling (insets in Figure 5.5). Almost all the vibrational modes identified in the transmission FTIR spectrum of pristine GF are present in the spectrum of cycled GF (Figure 5). For example, the strongest band at around 1185 cm^{-1} is assigned to the stretching mode of the SO_2 unit. In addition, some new features were observed, likely related to GF's decomposition products. The additional bands at about 3350 and 1600 cm^{-1} were assigned to water, which was probably introduced during cathode preparation. The additional bands at about 3140, 1140, 790, and 660 cm^{-1} were assigned to CH, SO_2, SF, and SNS units, respectively [37]. Since GF was electrochemically stable up to 4.5 V vs. Li/Li^+ (Figure 5.2(a)), it was probably thermally decomposed during the prolonged cycling at 60 °C. The thermal decomposition temperature of LiFSI was 66.9 °C [38], only slightly higher than the cell cycling temperature. As a result, the cell's internal temperature could exceed the thermal decomposition temperature of LiFSI during the prolonged cycling test because of heat accumulation.

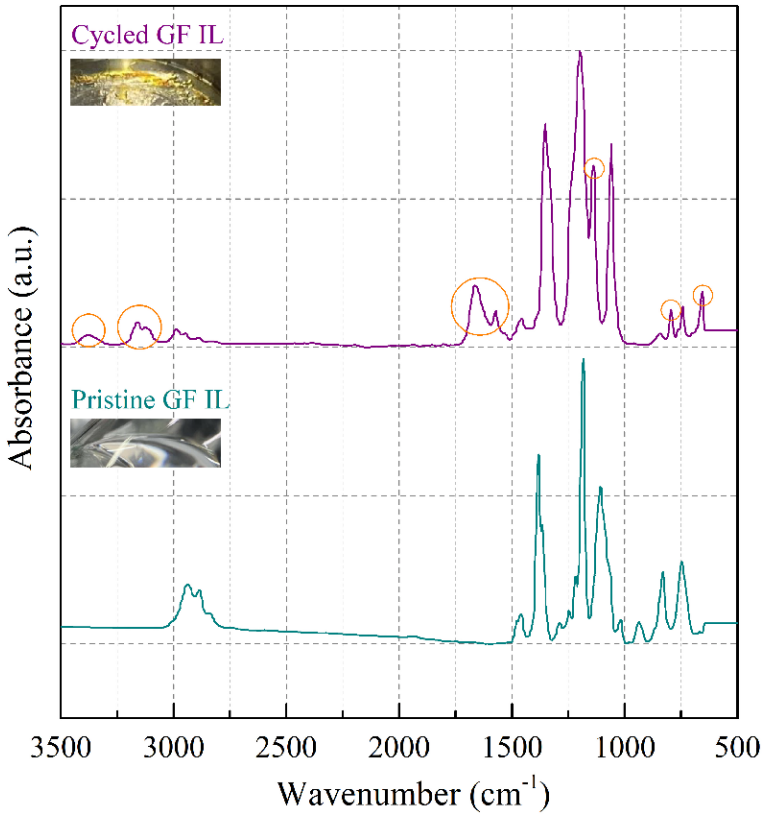

Figure 5.5. FTIR analysis of the composition change of GF after cycling. The insets are optical images of GF before (transparent) and after (yellowish) prolonged cycling at 60 °C.

5.3.5 Cycling performance of the ET-containing LCO cathode

The performance of the quasi-solid-state LCO cathode was not only dependent on the IL content but also dependent on the IL type. Figure 5.6 shows the galvanostatic cycling results of the ET-containing quasi-solid-state Li/Al-LLZO/LCO cells. The weight ratio of LCO: AB: PVDF: ET in the ET-containing LCO cathode was also 92: 4: 4: *x,* where *x*=4.3, 8.5, 12.8, 17, or 21.3. Similarly, the assembled coin cells were accordingly termed ET-4.3, ET-8.5, ET-12.8, ET-17, and ET-21.3. When *x*=4.3, the initial discharge capacity was 72.1 mA h g^{-1}, which decreased rapidly to 30.8 mA h g^{-1} after 20 cycles, and was only 10.5 mA h g^{-1} after 100 cycles (Figure 5.6(a)). However, a stable CE of about 100% was maintained after 100 cycles (Figure 5.6(b)). The discharge capacity

improved significantly with increasing IL content. When x=8.5, the initial discharge capacity reached 135.5 mA h g^{-1}. However, it decreased quickly to 111.7 mA h g^{-1} after the first 10 cycles and was 100.7 mA h g^{-1} after 100 cycles (Figure 5.6(c)). A high CE of about 100% for over 100 cycles was also achieved at x=8.5 (Figure 5.6(d)). The cyclability was further improved at x =12.8 (Figure 5.6(e)). The discharge capacity was greater than 108.9 mA h g^{-1} after 100 cycles, and the CE increased upon cycling and reached about 100% after 20 cycles (Figure 5.6(f)). In addition, the overpotential of the quasi-solid-state Li/Al-LLZO/LCO cell decreased with increasing IL content when $x \leq 12.8$. Further increasing the IL content resulted in a decrease in cell performance. Figure 5.6(g) (x=17) shows that the discharge capacity decreased continuously from an initial value of 129.3 to 68.1 mA h g^{-1} after 100 cycles. However, the CE was maintained at about 100% after 20 cycles (Figure 5.6(h)).

As discussed above, in the case of GF, excessive IL could block electron transport and cause particle agglomeration in the quasi-solid-state LCO cathode. The adverse effect of excessive IL became more apparent when x=21.3 (Figure 5.6(i)). The discharge capacity decreased rapidly from an initial value of 124.1 mA h g-1 to only 19.0 mA h g-1 after 100 cycles. Significant fluctuations of the CE were also observed (Figure 5.6(j)). Moreover, the cell overpotential increased with increasing IL content when $x \geqslant 12.8$. The ET-containing LCO cathode showed a much better cycling performance than the GF-containing LCO cathode, probably because ET had higher thermal stability and ionic conductivity than GF. However, ET would decompose electrochemically at potentials above 4.0 V vs. Li/Li^{+}.

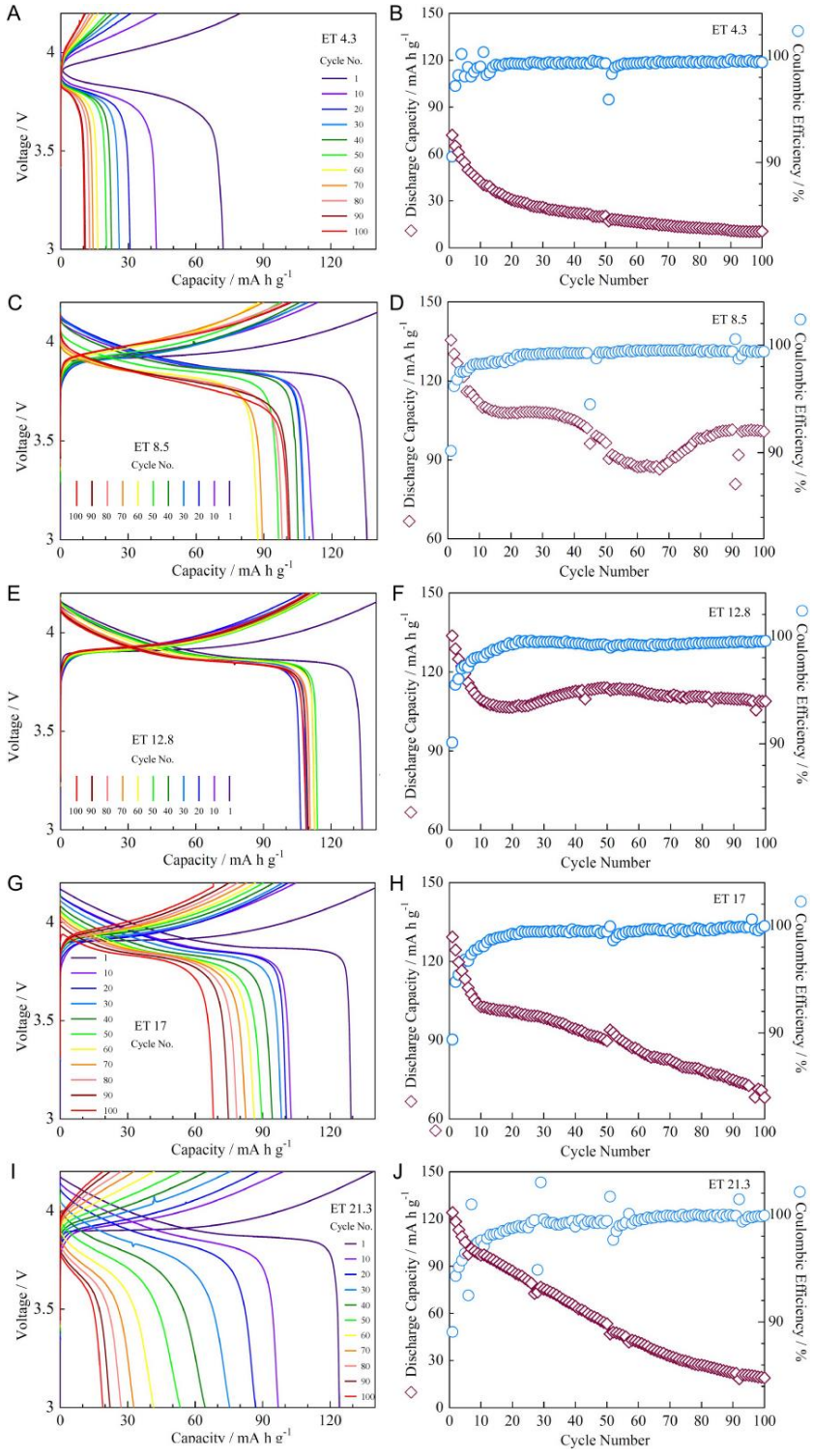

Figure 5.6. Electrochemical behavior of quasi-solid-state Li/Al-LLZO/LCO cells with different ET contents. (a) and (b) ET 4.3 (x=4.3), (c) and (d) ET 8.5 (x=8.5), (e) and (f) ET 12.8 (x=12.8), (g)

and (h) ET 17 (x=17), and (i) and (j) ET 21.3 (x=21.3). The C-rate is 0.025 C, and the cycling temperature is 60 °C.

5.3.6 EIS analysis of the quasi-solid-state Li/Al-LLZO/LCO cell

To better understand the effect of IL on the performance of the quasi-solid-state Li/Al-LLZO/LCO cell, EIS analysis was carried out (Figure 7). Each spectrum generally consists of two semi-circles, a smaller one in the high-frequency region (≥1MHz) (not readily visible), corresponding to the resistance of Al-LLZO ($R_{LLZO,}$ including both the grain boundary resistance R_{gb} and the bulk resistance R_b), and a larger one in the low-frequency region (<1MHz), corresponding to the charge transfer resistance R_{ct}. For the GF-containing Li/Al-LLZO/LCO cells, the overall resistance ($R_{overall}$) decreased significantly from about 1660 Ω cm^2 at x=5 to about 320 Ω cm^2 at x=50 (Figure 7(a)). The area-specific resistance (ASR) was defined as,

$$ASR = A \times R \qquad (5\text{-}2)$$

where A is the effective current collecting area and R is the measured resistance. The $R_{overall}$ of the all-solid-state Li/Al-LLZO/LCO cell was measured to be higher than 500,000 Ω cm^2. Considering that the anode-side interfacial resistance between Al-LLZO and Li was only about a few to several hundred Ω cm^2 [18, 21, 35, 39], the R_{ct} was dominated by the cathode-side interfacial resistance between LCO and Al-LLZO. IL therapy effectively reduced the interfacial resistance between LCO and Al-LLZO. After 50 cycles, a substantial increase in $R_{overall}$ from about 750 to 2230 Ω cm^2 was observed for x =10. In comparison, there was almost no change in $R_{overall}$ for x=5 and x=50 (Figures 5.7(a) and (b)), probably because GF was either too little (x =5) or too much (x=50) in the composite LCO cathode.

The EIS spectra of the ET-containing Li/Al-LLZO/LCO cells are shown in Figures 5.7(c) and (d). The EIS data were modeled using a simplified equivalent circuit (inset in Figure 5.7(d)), where

Rct represented the sum of the interfacial resistance from both the cathode and anode sides. The Roverall was about 830 Ω cm^2 at x= 4.3, which decreased to about 560 Ω cm^2 at x=12.8. However, the Roverall increased slightly with further increased ET content (Figure 5.7(c)). After 100 cycles, the Roverall increased noticeably for all cells (Figure 5.7(d)). The evolution of the Roverall was correlated well with cell performance (Figure 5.6).

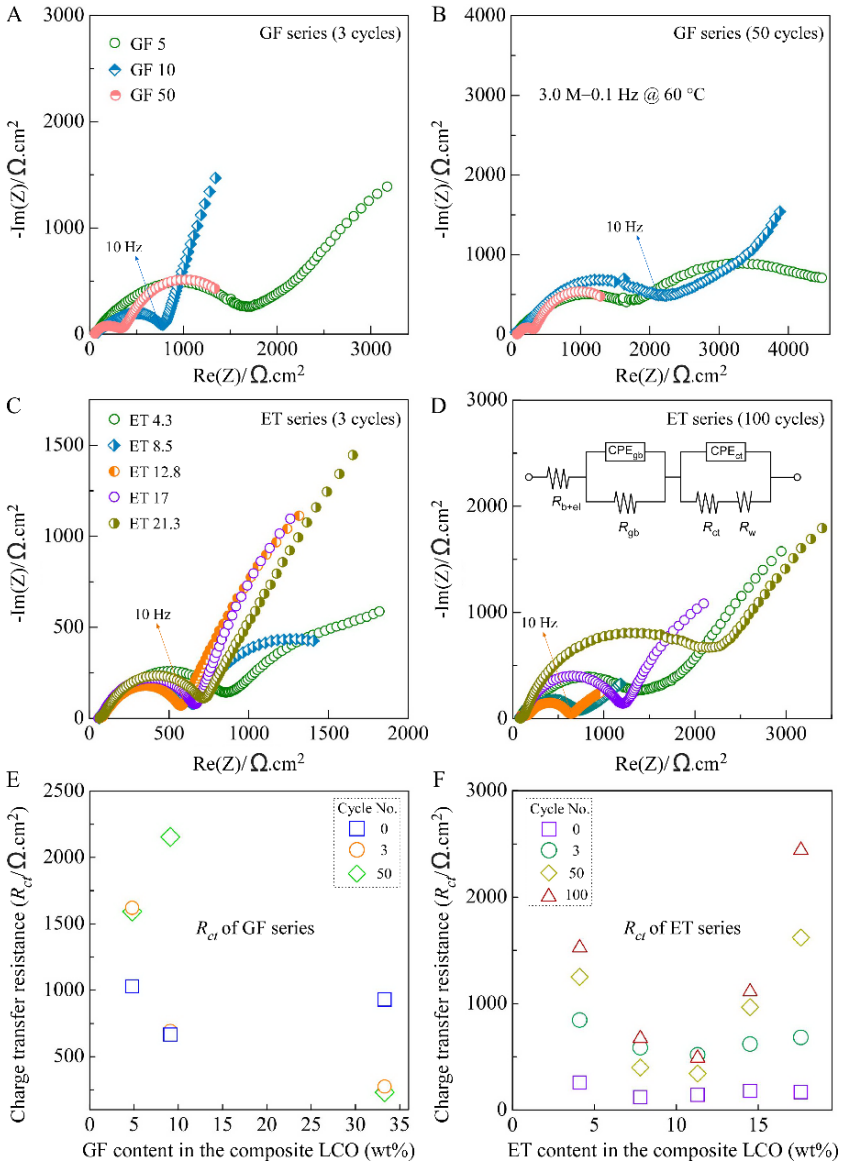

Figure 5.7. Impedance evolution of quasi-solid-state Li/Al-LLZO/LCO cells at 60 °C as a function of IL type, content, and cycle number. (a) EIS spectra of the GF-containing Li/Al-LLZO/LCO cell

after three cycles, (b) EIS spectra of the GF-containing Li/Al-LLZO/LCO cell after 50 cycles, (c) EIS spectra of the ET-containing Li/Al-LLZO/LCO cell after three cycles, (d) EIS spectra of the ET-containing Li/Al-LLZO/LCO cell after 50 cycles, (e) R_{ct} of the GF-containing Li/Al-LLZO/LCO cell and (f) R_{ct} of the ET-containing Li/Al-LLZO/LCO cell.

As plotted in Figures 5.7(e) and (f), the R_{ct} of the GF cell is 600-1000 Ω cm^2 before cycling, while that of the ET cells is 120-250 Ω cm^2. After cycling, the R_{ct} increased significantly in almost all the cases, irrespective of the IL type and content, indicating that decomposition of the ILs or interfacial side reactions should have occurred. Nevertheless, ET was more suitable than GF for preparing the IL-containing quasi-solid-state LCO cathode. As a result, more detailed research was conducted on the stability analysis of the Al-LLZO pellet and the LCO active material against ET.

5.3.7 Stability study of Al-LLZO against ET by XPS

Since the IL-containing LCO cathode/Al-LLZO pellet interface could be divided into two distinct solid/liquid interfaces, i.e., LCO/IL and IL/Al-LLZO, the stability of the cathode-side interfaces was thus dependent on the stability of LCO and Al-LLZO against the IL. Figure 5.8 shows the X-ray photoelectron spectroscopy (XPS) analysis results of Al-LLZO in different conditions: as-polished (pristine), soaked in a 1 mol dm^{-3} $LiPF_6$/EC: DMC (v: v=1:1) (LP30) electrolyte for 200 h, soaked in ET for 200 h, and galvanostatically cycled for 100 cycles at 60°C. Adventitious carbon (centered at 248.8 eV in C 1s) and carbonate (289. 7 eV in C 1s) were observed on the Al-LLZO pellet polished in an Ar-filled glove box. As reported previously, surface contaminants, such as Li_2CO_3, would occur quickly, even in an Ar atmosphere [36]. Apparent enrichment in C-O species (286.5 eV in C 1s) indicated that a reaction between Al-LLZO and LP30 occurred, which was also observed by Liu et al. [40]. On the other hand, almost no carbonate signal

was observed in both the C 1s and O 1s spectra (Figure 5S3) of the ET-soaked Al-LLZO pellet, and the amount of the C-O species was relatively low, suggesting that Al-LLZO was relatively stable against ET. However, the presence of carbon (248.8 eV in C 1s) on the Al-LLZO surface increased significantly after 100 cycles at 60°C, probably due to the electrochemical decomposition of ET or reactions between Al-LLZO and ET.

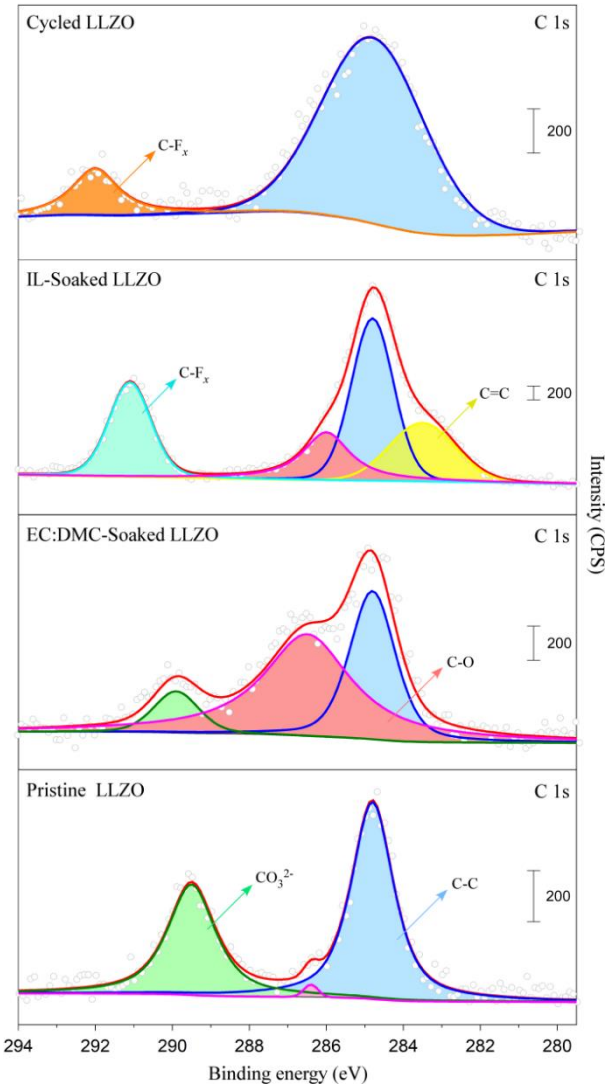

Figure 5.8. XPS analysis of the surface chemistry (C 1s) of the Al-LLZO pellet in different conditions. As-polished (pristine), soaked in 1 mol dm^{-3} $LiPF_6$/EC-DMC (v:v=1:1) (LP30) for 200 h, soaked in ET for 200 h, and galvanostatically cycled for 100 cycles at 60°C.

5.3.8 Stability study of LCO against ET by TEM

The stability of LCO against ET was investigated using TEM. As shown in Figure 5.9(a), the pristine LCO particle has a crystalline appearance, which is revealed by the high-resolution TEM image shown in Figure 5.9(b). The well-defined layered structure with an interplanar spacing of about 0.23 nm is indexed to be the (006) crystal plane of LCO. No additional or amorphous surface layer is observed. A TEM micrograph of the quasi-solid-state composite LCO cathode before cycling is shown in Figure 5.9(c), from which the LCO particles are embedded in a PVDF polymer matrix with a brighter contrast. An enlargement of the boxed area without PVDF is shown in Figure 5.9(d), where an amorphous cathode electrolyte interphase (CEI) layer of about 17.5 nm in thickness is observed, suggesting that reactions occurred at the IL/LCO interface. Cracking of cycled LCO particles was observed (Figure 5.9(e)), indicating that stress build-up in the quasi-solid-state battery was severe during prolonged cycling. A high-resolution TEM image of the boxed area without any PVDF is shown in Figure 5.9(f), where the thickness of the CEI layer has increased significantly from about 17.5 to 43.5 nm. The continuous growth of the CEI layer would lead to the increase of R_{ct}. In addition, the outermost part of the CEI layer (about 8.9 nm thick) with a darker contrast showed a more crystalline structure, likely related to the transfer of some heavy elements.

5.3.9 Components of the CEI layer analyzed by XPS

XPS analysis was carried out to understand the reasons for the continuous growth of the CEI layer on the LCO surface. As shown in Figure 5.10, the appearance of the peak assigned to CoO_x at 530.3 eV suggests the decomposition of LCO [41]. The appearance of the peak assigned to the Li-F bond at 686.0 eV indicates the decomposition of the LiTFSI salt in ET [42]. Also, carbonaceous species, such as C-C and C-H, were identified in the CEI layer. Thus, the CEI layer

on LCO consisted of inorganic and organic compounds that were likely the decomposition products of LCO and ET.

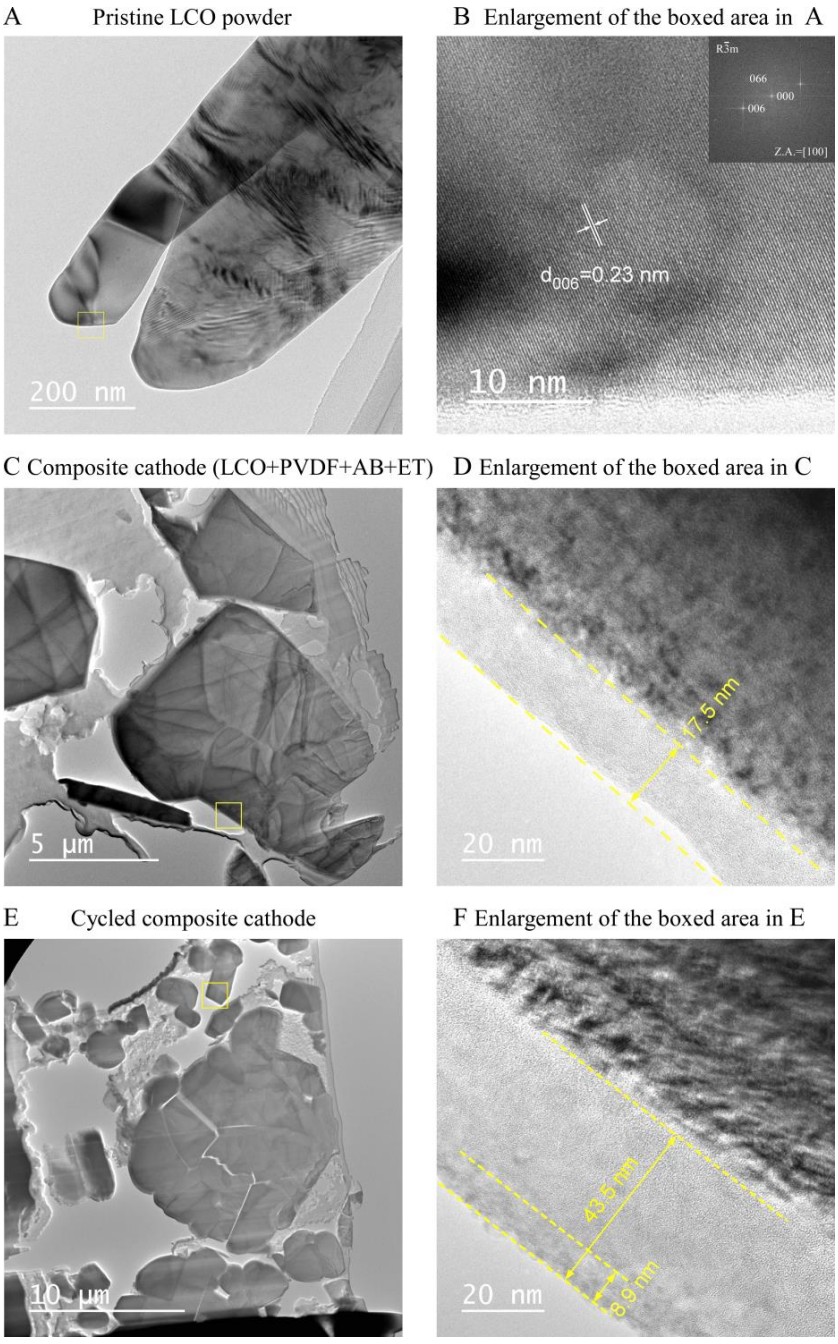

Figure 5.9. Bright-field TEM micrographs of the LCO active material. (a) and (b) Pristine LCO powder, (c) and (d) ET-containing quasi-solid-state LCO cathode before cycling, (e) and (f) ET-

containing quasi-solid-state LCO cathode after 100 cycles at 60°C. The inset in (b) is a fast Fourier transform (FFT) pattern of the high-resolution TEM image.

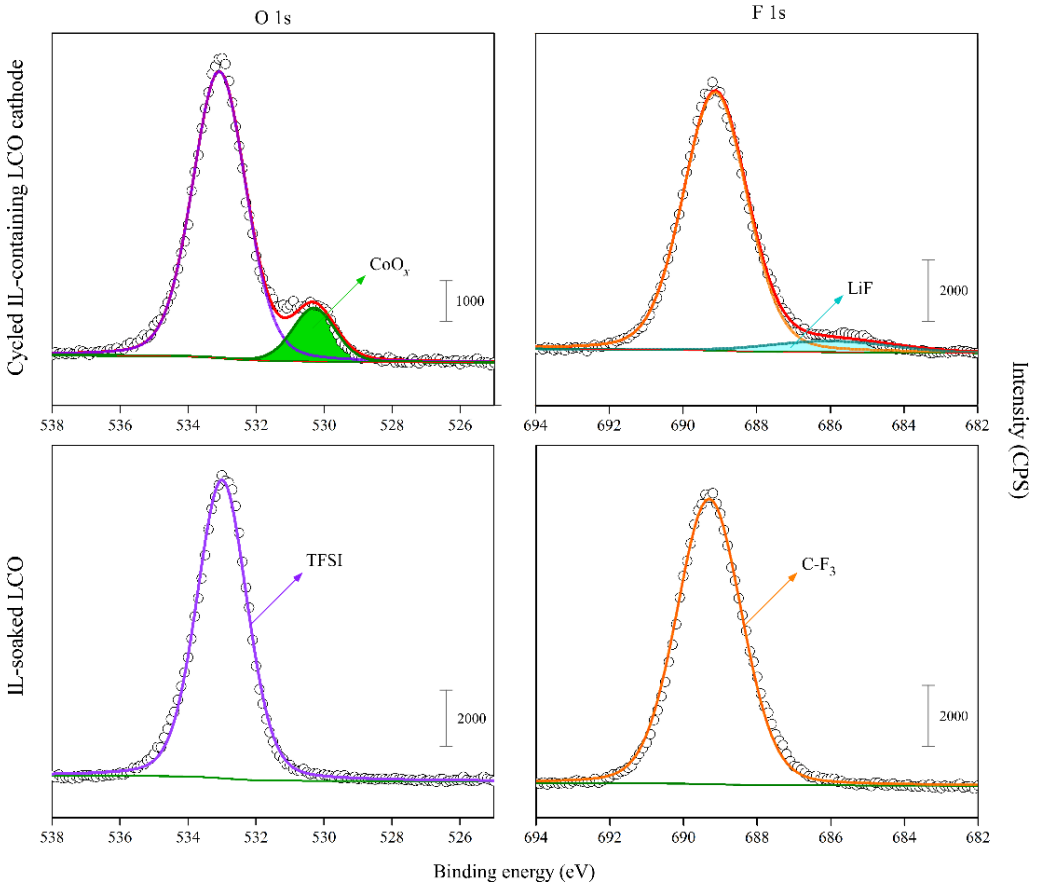

Figure 5.10. XPS analysis of the components of the CEI layer formed on the LCO surface in different conditions. Soaked in ET for 200 h and Cycled at 60°C for 100 cycles.

5.3.10 Failure mechanisms of the quasi-solid-state Li/Al-LLZO/LCO cell

Failure mechanisms of the quasi-solid-state Li/Al-LLZO/LCO cell are illustrated in Figure 5.11. First, GF was thermally decomposed after prolonged cycling at 60 °C (Figure 5.11(a)), as indicated by the FTIR analysis, although it was electrochemically stable up to 4.5 V vs. Li/Li$^+$. On the other hand, ET became electrochemically oxidized at potentials slightly above 4.0 V vs. Li/Li$^+$, as evidenced by the LSV and CV analysis. The instabilities of the ILs were the main reason for the

decay of the quasi-solid-state Li metal batteries. Also, GF might dissociate or desolvate because of the nanoconfinement effects from the nanoporous carbon black and the chain-like PVDF binder (Figures 5.11(b) and (c)) [43-44]. Since the interaction between the tetraglyme and Li^+ ion was relatively weak, the chelate complex was intrinsically unstable [45]. The cracking of LCO particles was also revealed by TEM analysis, which was likely due to stress accumulation in the quasi-solid-state battery and fatigue of LCO during prolonged cycling (Figure 5.11(d)). As illustrated in Figure 5.11(e), particle agglomeration in ET was also confirmed by dynamic light scattering (DLS) analysis (Figure 5S4). This decreased the utilization of the cathode active material. The continuous growth of the CEI layer on LCO was another reason for the gradual decay of the cell capacity (Figure 5.11(f)). The EIS, XPS, and TEM analysis confirmed the growth of the CEI layer with cycling, which was likely related to the reactions between ET and LCO, as indicated by the TEM results. Meanwhile, the reaction between LLZO and ET was confirmed by XPS analysis. Possible reactions between Li metal and the ILs could also be one of the reasons for the capacity decay of the IL-containing Li/Al-LLZO/LCO battery (Figure 5.11 (g)). Similarly, reactions between the ILs and the Al current collector, i.e., corrosion [46], would occur (Figure 5.11(h)). Broad redox peaks were observed in the CV profiles of GF when an Al foil was used as the working electrode (Figure 5S5), likely due to the corrosion of Al in GF. The charge transfer pathway between LCO and the Al current collector would be blocked to some extent when the IL was excessive because the electron-conductive carbon black particles would be isolated by the excessive IL, which was electronically insulating. (Figure 5.11(i)).

Despite the shortcomings of the quasi-solid-state composite LCO cathode, there are strategies to improve its performance. First, the search for a more suitable IL is essential. Second, coating the cathode active material and the solid electrolyte with a Li-ion conductive material, such as $LiNbO_3$

or $LiTaO_3$, can be a feasible way to improve their stability against the ILs [47].

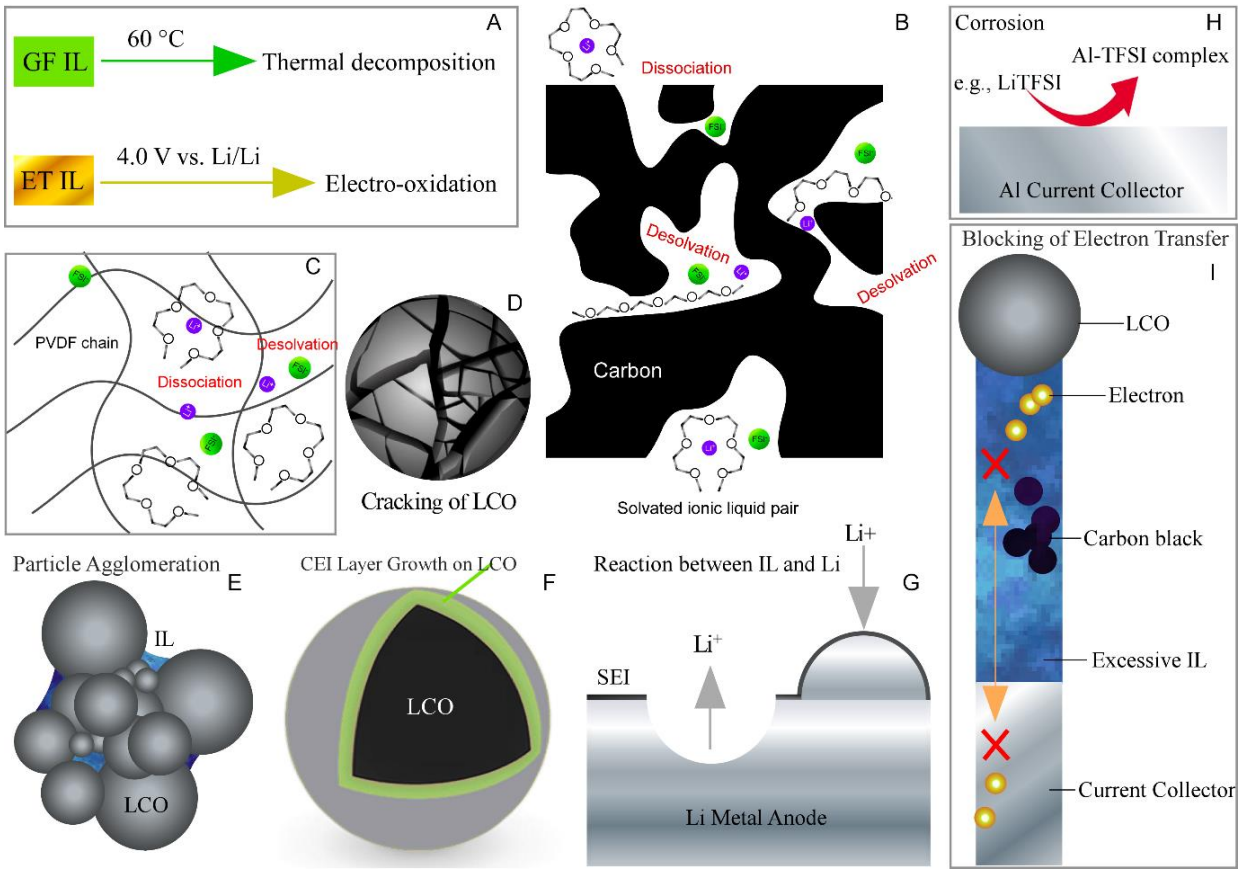

Figure 5.11. Illustration of failure mechanisms of the quasi-solid-state LCO cathode. (a) Thermal decomposition or electron-oxidation of the ILs, (b) and (c) Dissociation or desolvation of GF in carbon black and PVDF binder, (d) Cracking of LCO caused by stress accumulation and fatigue, (e) Agglomeration of LCO (or AB) particles, (f) Growth of the CEI layer on LCO because of reactions between LCO and the IL, (g) Possible reaction between Li metal and the ILs, (h) Corrosion of Al current collector in the ILs and (i) Blocking of electron transport by excessive IL.

5.4 Conclusion

This paper presents an alternative strategy for reducing the interfacial resistance between cathodes and solid electrolytes through IL therapy. An IL-containing and non-fluidic LCO

composite cathode was developed, and the LCO/Al-LLZO interfacial resistance was reduced effectively from more than 500,000 to about 100 Ω cm^2. The optimal content of the IL in the quasi-solid-state composite LCO cathode was found to be about 11 wt%. Quasi-solid-state Li/Al-LLZO/LCO cells achieved relatively high-capacity retention of about 80% after 100 cycles at 60 °C. The cell capacity decay was mainly due to thermal or electrochemical instability of the IL. There were also stability issues of LCO and Al-LLZO against the IL. Thus, searching for a suitable IL is critical for developing and maturing garnet-based quasi-solid-state Li metal batteries.

5.5 Limitations of the Study

The two ionic liquids (ILs) used in this study, i.e., the solvate equimolar Li(G4)FSI and the conventional 1 mol dm^{-3} LiTFSI/EMI-TFSI, are either thermally unstable above 60 °C or become electrochemically oxidized at potentials above 4.0 V vs. Li/Li^+. Also, it should be noted that the viscosities of the two ILs at room temperature are relatively high. Thus, identifying a suitable IL is critical for further developing the quasi-solid-state composite $LiCoO_2$ cathode. In addition, the relative density of the Al-doped LLZO pellet is relatively low, about 95%, because it was prepared by pressureless sintering. Better battery performance is expected if a denser or a Ta-doped LLZO pellet (with a higher ionic conductivity) is used.

5.6 Method details

5.6.1 Preparation of Al-LLZO pellets

Al-doped LLZO powder was prepared by a solid-state reaction method [48]. $LiOH{\cdot}H_2O$, $La(OH)_3$, and ZrO_2 powders were mixed by planetary ball-milling and were calcined at 900 °C for 15 h. After mixing with a γ-Al_2O_3 powder, the calcined powder was pelletized and sintered at 900 °C for 3 h and then at 1200 °C for 24 h. The molar ratio of the starting materials of $LiOH{\cdot}H_2O$,

$La(OH)_3$, ZrO_2, and γ-Al_2O_3 was 6.9: 3.0 : 2.0: 0.125.

5.6.2 Fabrication of quasi-solid-state Li/Al-LLZO/LCO coin cells

The IL-containing LCO slurries were cast onto the cylinder-shaped Al-LLZO pellets (12 mm in diameter and 1 mm in thickness) and then dried at 80 °C in a vacuum for 12 h. The loading of the active material was about 6.0 mg cm^{-2}. One base surface of the pellets was coated with a thin gold layer, which would alloy with Li metal at heating (80 °C) to reduce the anode-side interfacial resistance. The quasi-solid-state LCO/Al-LLZO/Au trilayered structure was paired with a Li foil to make a full cell. All the CR2032-type coin cells were assembled in an Ar-filled glove box.

5.6.3 Materials characterization

The crystal structure of the high-temperature sintered Al-LLZO pellet was analyzed by X-ray diffraction (XRD, Rigaku SmartLab) (Figure S6). Micro-sized pores were observed on the cross-sectional surface of the Al-LLZO pellet (Figure S7). The relative density of the Al-LLZO pellet was about 95%. Cross-sections of the Al-LLZO/LCO bilayer structure were prepared with focused ion beam (FIB) milling and were analyzed using a scanning electron microscope (SEM, JSM-6490A). The particle size in the LCO slurry was measured by dynamic light scattering (DLS, Partica mini LA-350). The morphological evolution of the LCO surface was studied using an analytical scanning transmission electron microscope (STEM, JEM-ARM200F). Transmission and attenuated total reflection (ATR) Fourier-transform infrared spectroscopy (FTIR) was used to analyze the composition change of the IL after cycling at 60 ° C. The surface chemistry of Al-LLZO was analyzed with an X-ray photoelectron spectrometer (XPS, PHI 5000 VersaProbe II).

5.6.4 Electrochemical measurements

AC electrochemical impedance spectroscopy was performed in the frequency range from 3 MHz to 0.1 Hz at 60 °C (EIS, Biologic SP-300). The amplitude of the perturbation was 10 mV. Galvanostatic cycling of the quasi-solid-state Li/Al-LLZO/LCO cell was carried out at 60 °C with a constant current density of 20 μA cm^{-2}, corresponding to 1/40 C (0.025 C). The cut-off voltage range was 3.0 to 4.2 V.

Supplemental information

Table 5 S1 Ionic conductivity of the Li(G4)FSI solvate IL (designated as GF), Related to Figure 2.

Temperature (°C)	Ionic conductivity (10^{-3} S cm^{-1})
30	2.1
40	3.1
50	4.0
60	6.2
70	8.0
80	10.2

Table 5 S2 Ionic conductivity of the 1 mol dm^{-3} LiTFSI/EMI-TFSI (designated as ET), Related to Figure 5.2.

Temperature (°C)	Ionic conductivity (10^{-3} S cm^{-1})
30	5.0
40	6.9
50	9.5
60	12.5
70	15.9
80	19.7

Table 5 S3 Ionic conductivity of the Al-doped LLZO pellet, Related to Figure 5.2.

Temperature (°C)	Ionic conductivity (10^{-4} S cm^{-1})
30	3.6
40	4.8
50	7.7
60	10.5
70	13.8
80	18.3

Table 5 S4 IL content in the quasi-solid-state LCO cathode, Related to Figures 5.4 and 6.

Equimolar Li(G4)FSI solvate IL (designated as GF) series			
x	Wt%	Vol%	Cell
0	0	0	All-solid-state
5	4.8	14.6	GF 5
10	9.1	25.5	GF 10
50	33.3	63.1	GF 50
1 mol dm^{-3} LiTFSI/EMI-TFSI conventional IL (designated as ET) series			
4.3	4.1	11.1	ET 4.3
8.5	7.8	19.8	ET 8.5
12.8	11.3	27.1	ET 12.8
17	14.5	33.1	ET 17
21.3	17.6	38.2	ET 21.3

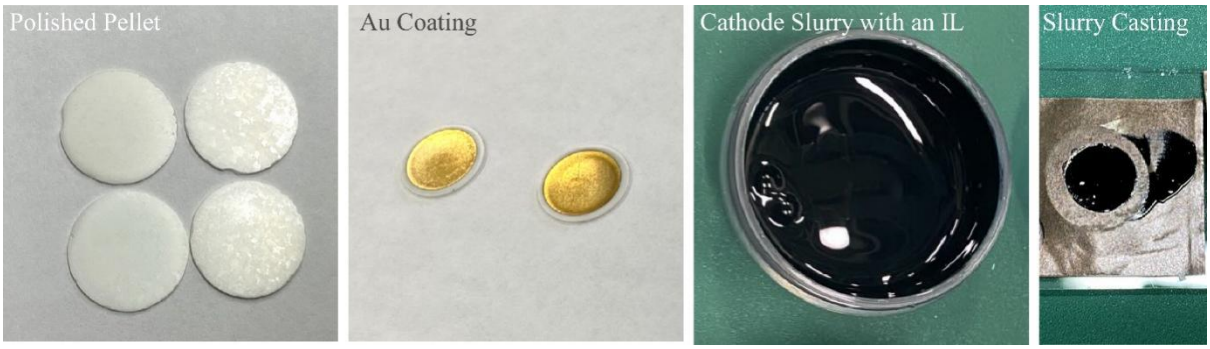

Figure 5 S1. The procedure of casting the quasi-solid-state LCO cathode slurry onto the Al-LLZO pellet's surface, Related to Figure 5.3.

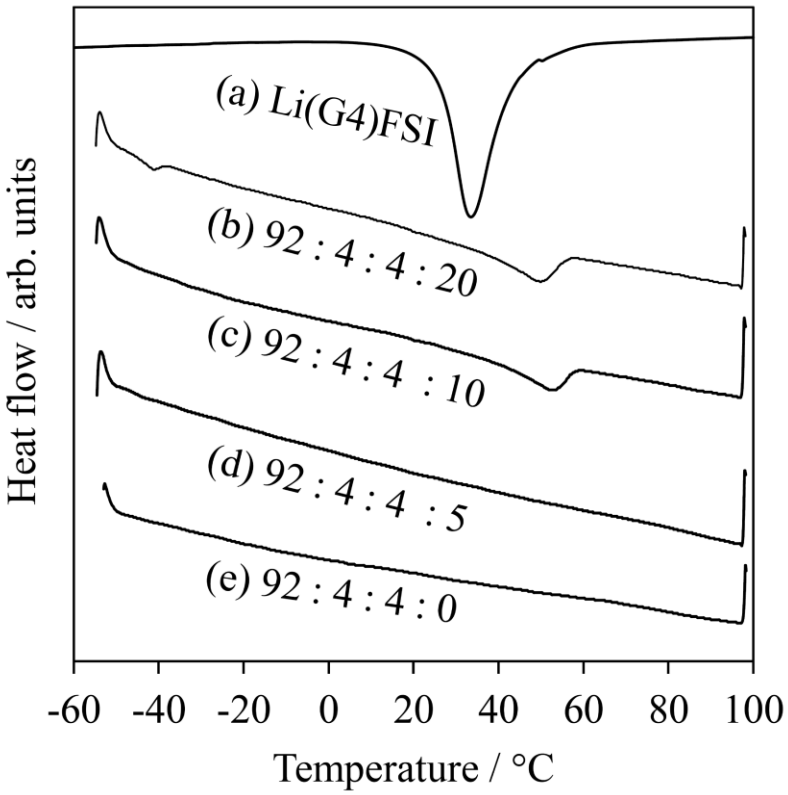

Figure 5 S2. DSC profiles of the quasi-solid-state LCO cathode with different GF contents. The weight ratio of LCO: AB: PVDF: GF in the quasi-solid-state LCO cathode was 92: 4: 4: *x* (w/w). (a) Pure Li(G4)FSI (GF), (b) *x*=20, (c) *x*=10, (d) *x=5*, and (e) *x*=0, Related to Figure 5.3.

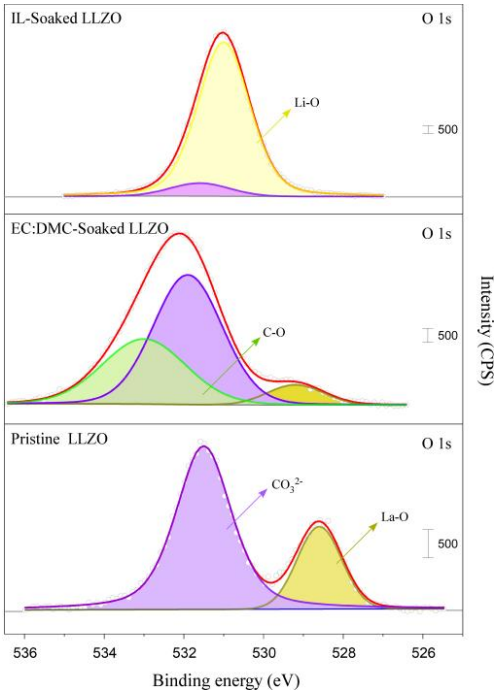

Figure 5 S3. Analysis of the surface chemistry (O 1s) of the Al-LLZO pellet in different conditions. As-polished (pristine), soaked in 1 mol dm^{-3} $LiPF_6$/EC-DMC (v:v=1:1) (LP30) for 200 h, and soaked in the conventional ET IL for 200 h, Related to Figure 8.

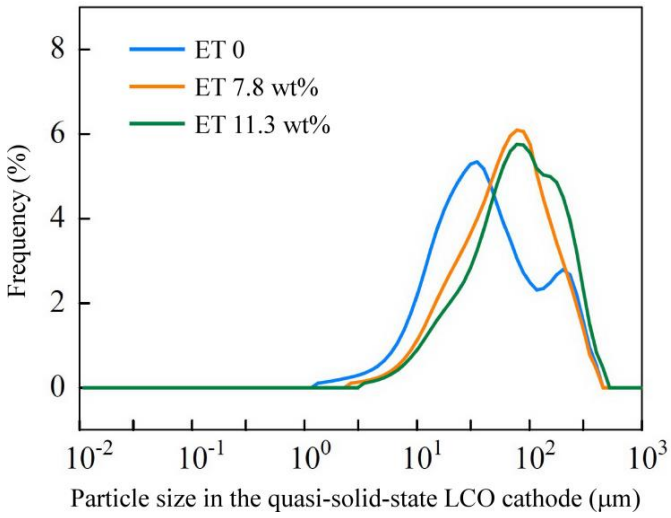

Figure 5 S4. DLS analysis of the particle size in the quasi-solid-state LCO cathode as a function of the IL content. The IL here is the conventional 1 mol dm^{-3} LiTFSI/EMI-TFSI, and its content in

the quasi-solid-state LCO cathode was 0, 7.8 wt%, and 11.3 wt%, respectively. The particle size in the quasi-solid-state LCO cathode increases with increasing IL content, Related to Figure 11.

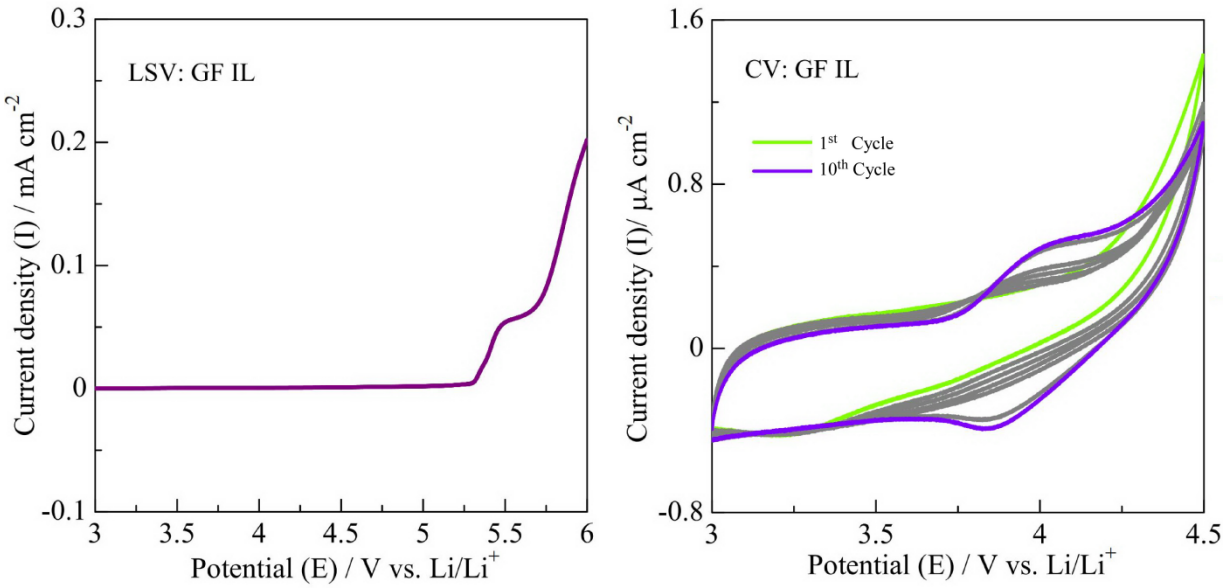

Figure 5 S5. Electrochemical stability analysis of the solvate GF IL at 25 °C. (a) Linear sweep voltammogram, (b) Cyclic voltammogram. The scan rates for LSV and CV were 1 mV S^{-1}. An Al foil was used as the working electrode (WE), and a Li foil was used as the counter electrode (CE) as well as the reference electrode (RE). A highly porous polyimide film (PI) was used as the separator. Broad redox peaks are observed at about 3.8 V and 4.0 V *vs*. Li/Li^+ in the CV profiles, and the processes look reversible. They are likely related to impurity phases on the surface of the Al working electrode or a slow corrosion process of the Al working electrode in the IL, Related to Figure 5.11.

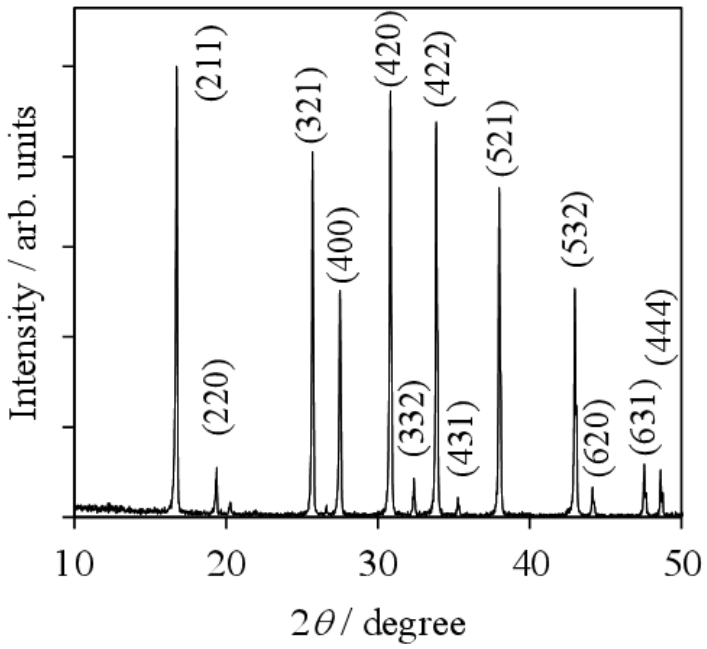

Figure 5 S6. XRD profile of the 1000 ℃ sintered Al-LLZO pellet. It indicates that the high temperature-sintered Al-LLZO pellet has a cubic structure, Related to Figure 5.2.

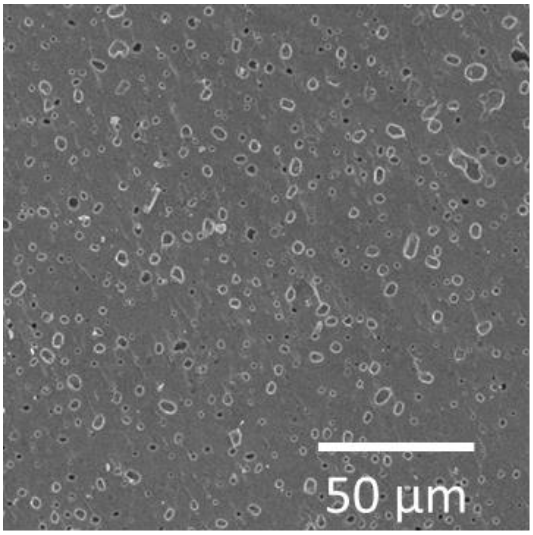

Figure 5 S7. A cross-sectional SEM micrograph of the 1000 ℃ sintered Al-LLZO pellet. Micropores are observed, and the relative density of the Al-LLZO pellet is about 95%, Related to Figure 5.2.

Reference

[1] A. Yoshino, The Birth of the Lithium-Ion Battery, Angewandte Chemie International Edition 51(24) (2012) 5798-5800.

[2] R. Van Noorden, The rechargeable revolution: A better battery, Nature News 507(7490) (2014) 26-28.

[3] G. Cui, Reasonable design of high-energy-density solid-state lithium-metal batteries, Matter 2(4) (2020) 805-815.

[4] C. Fang, X. Wang, Y.S. Meng, Key issues hindering a practical lithium-metal anode, Trends in Chemistry 1(2) (2019) 152-158.

[5] M.S. Whittingham, Electrical energy storage and intercalation chemistry, Science 192(4244) (1976) 1126-1127.

[6] C. Monroe, J. Newman, The impact of elastic deformation on deposition kinetics at lithium/polymer interfaces, Journal of The Electrochemical Society 152(2) (2005) A396.

[7] S. Yu, R.D. Schmidt, R. Garcia-Mendez, E. Herbert, N.J. Dudney, J.B. Wolfenstine, J. Sakamoto, D.J. Siegel, Elastic properties of the solid electrolyte $Li_7La_3Zr_2O_{12}$ (LLZO), Chemistry of Materials 28(1) (2016) 197-206.

[8] T. Krauskopf, F.H. Richter, W.G. Zeier, J. Janek, Physicochemical concepts of the lithium metal anode in solid-state batteries, Chemical Reviews 120(15) (2020) 7745-7794.

[9] R. Murugan, V. Thangadurai, W. Weppner, Fast lithium ion conduction in garnet-type $Li_7La_3Zr_2O_{12}$, Angewandte Chemie International Edition 46(41) (2007) 7778-7781.

[10] N. Zhao, W. Khokhar, Z. Bi, C. Shi, X. Guo, L.Z. Fan, C.W. Nan, Solid garnet batteries, Joule 3(5) (2019) 1190-1199.

[11] M. Tatsumisago, M. Nagao, A. Hayashi, Recent development of sulfide solid electrolytes and interfacial modification for all-solid-state rechargeable lithium batteries, Journal of Asian Ceramic Societies 1(1) (2013) 17-25.

[12] T. Famprikis, P. Canepa, J.A. Dawson, M.S. Islam, C. Masquelier, Fundamentals of inorganic solid-state electrolytes for batteries, Nature Materials 18(12) (2019) 1278-1291.

[13] J.E. Ni, E.D. Case, J.S. Sakamoto, E. Rangasamy, J.B. Wolfenstine, Room temperature elastic moduli and Vickers hardness of hot-pressed LLZO cubic garnet, Journal of Materials Science 47(23) (2012) 7978-7985.

[14] K.J. Kim, M. Balaish, M. Wadaguchi, L. Kong, J.L. Rupp, Solid-State Li–Metal Batteries: Challenges and Horizons of Oxide and Sulfide Solid Electrolytes and Their Interfaces, Advanced Energy Materials 11(1) (2021) 2002689.

[15] D. Wang, C. Zhu, Y. Fu, X. Sun, Y. Yang, Interfaces in Garnet-Based All-Solid-State Lithium Batteries, Advanced Energy Materials 10(39) (2020) 2001318.

[16] X. Han, Y. Gong, K.K. Fu, X. He, G.T. Hitz, J. Dai, A. Pearse, B. Liu, H. Wang, G. Rubloff, Negating interfacial impedance in garnet-based solid-state Li metal batteries, Nature Materials 16(5) (2017) 572-579.

[17] J. Wakasugi, H. Munakata, K. Kanamura, Effect of gold layer on interface resistance between lithium metal anode and $Li_{6.25}Al_{0.25}La_3Zr_2O_{12}$ solid electrolyte, Journal of The Electrochemical Society 164(6) (2017) A1022-A1025.

[18] C. Tsai, V. Roddatis, V. Chandran, Q. Ma, S. Uhlenbruck, M. Bram, P. Heitjans, O. Guillon, $Li_7La_3Zr_2O_{12}$ interface modification for Li dendrite prevention, ACS Applied Materials & Interfaces 8(16) (2016) 10617-10626.

[19] W. Feng, X. Dong, P. Li, Y. Wang, Y. Xia, Interfacial modification of Li/Garnet electrolyte by a lithiophilic and breathing interlayer, Journal of Power Sources 419 (2019) 91-98.

[20] C. Wang, Y. Gong, B. Liu, K. Fu, Y. Yao, E. Hitz, Y. Li, J. Dai, S. Xu, W. Luo, Conformal, nanoscale ZnO surface modification of garnet-based solid-state electrolyte for lithium metal anodes, Nano Letters 17(1) (2017) 565-571.

[21] R. Inada, S. Yasuda, H. Hosokawa, M. Saito, T. Tojo, Y. Sakurai, Formation and stability of interface between garnet-type Ta-doped $Li_7La_3Zr_2O_{12}$ solid electrolyte and lithium metal electrode, Batteries 4(2) (2018) 26.

[22] H. Zheng, S. Wu, R. Tian, Z. Xu, H. Zhu, H. Duan, H. Liu, Intrinsic Lithiophilicity of Li–Garnet Electrolytes Enabling High-Rate Lithium Cycling, Advanced Functional Materials (2019) 1906189.

[23] M.J. Wang, R. Choudhury, J. Sakamoto, Characterizing the Li-Solid-Electrolyte Interface Dynamics as a Function of Stack Pressure and Current Density, Joule 3(9) (2019) 2165-2178.

[24] S. Ohta, J. Seki, Y. Yagi, Y. Kihira, T. Tani, T. Asaoka, Co-sinterable lithium garnet-type oxide electrolyte with cathode for all-solid-state lithium ion battery, Journal of Power Sources 265 (2014) 40-44.

[25] E.J. Cheng, N.J. Taylor, J. Wolfenstine, J. Sakamoto, Elastic properties of lithium cobalt oxide ($LiCoO_2$), Journal of Asian Ceramic Societies 5(2) (2017) 113-117.

[26] C.Z. Zhao, B.C. Zhao, C. Yan, X.Q. Zhang, J.Q. Huang, Y. Mo, X. Xu, H. Li, Q. Zhang, Liquid phase therapy to solid electrolyte–electrode interface in solid-state Li metal batteries: a review, Energy Storage Materials 24 (2020) 75-84.

[27] E.J. Cheng, T. Kimura, M. Shoji, H. Ueda, H. Munakata, K. Kanamura, Ceramic-based flexible sheet electrolyte for Li batteries, ACS Applied Materials & Interfaces 12(9) (2020) 10382-10388.

[28] M. Watanabe, M.L. Thomas, S. Zhang, K. Ueno, T. Yasuda, K. Dokko, Application of ionic liquids to energy storage and conversion materials and devices, Chemical Reviews 117(10) (2017) 7190-7239.

[29] H.W. Kim, P. Manikandan, Y.J. Lim, J.H. Kim, S.. Nam, Y. Kim, Hybrid solid electrolyte with the combination of $Li_7La_3Zr_2O_{12}$ ceramic and ionic liquid for high voltage pseudo-solid-state Li-ion batteries, Journal of Materials Chemistry A 4(43) (2016) 17025-17032.

[30] W. Huang, Z. Bi, N. Zhao, Q. Sun, X. Guo, Chemical interface engineering of solid garnet batteries for long-life and high-rate performance, Chemical Engineering Journal 424 (2021) 130423.

[31] S. Sugata, N. Saito, A. Watanabe, K. Watanabe, J.-D. Kim, K. Kitagawa, Y. Suzuki, I. Honma, Quasi-solid-state lithium batteries using bulk-size transparent $Li_7La_3Zr_2O_{12}$ electrolytes, Solid State Ionics 319 (2018) 285-290.

[32] L. Liu, X. Qi, Q. Ma, X. Rong, Y.-S. Hu, Z. Zhou, H. Li, X. Huang, L. Chen, Toothpaste-like electrode: A novel approach to optimize the interface for solid-state sodium-ion batteries with ultralong cycle life, ACS Applied Materials & Interfaces 8(48) (2016) 32631-32636.

[33] S. Tsuzuki, W. Shinoda, M. Matsugami, Y. Umebayashi, K. Ueno, T. Mandai, S. Seki, K. Dokko, M. Watanabe, Structures of $[Li(glyme)]^+$ complexes and their interactions with anions in equimolar mixtures of glymes and Li [TFSA]: analysis by molecular dynamics simulations, Physical Chemistry Chemical Physics 17(1) (2015) 126-129.

[34] Y. Yamada, Concentrated battery electrolytes: Developing new functions by manipulating the coordination states, Bulletin of the Chemical Society of Japan 93(1) (2020) 109-118.

[35] A. Sharafi, E. Kazyak, A.L. Davis, S. Yu, T. Thompson, D.J. Siegel, N.P. Dasgupta, J. Sakamoto, Surface chemistry mechanism of ultra-low interfacial resistance in the solid-state electrolyte $Li_7La_3Zr_2O_{12}$, Chemistry of Materials 29(18) (2017) 7961-7968.

[36] H. Yamada, T. Ito, S.P. Kammampata, V. Thangadurai, Toward Understanding the Reactivity of Garnet-Type Solid Electrolytes with H_2O/CO_2 in a Glovebox Using X-ray Photoelectron Spectroscopy and Electrochemical Methods, ACS Applied Materials & Interfaces 12(32) (2020) 36119-36127.

[37] M. Kerner, N. Plylahan, J. Scheers, P. Johansson, Thermal stability and decomposition of lithium bis (fluorosulfonyl) imide (LiFSI) salts, RSC Advances 6(28) (2016) 23327-23334.

[38] K. Kubota, T. Nohira, T. Goto, R. Hagiwara, Novel inorganic ionic liquids possessing low melting temperatures and wide electrochemical windows: Binary mixtures of alkali bis (fluorosulfonyl) amides, Electrochemistry Communications 10(12) (2008) 1886-1888.

[39] N.J. Taylor, S. Stangeland-Molo, C.G. Haslam, A. Sharafi, T. Thompson, M. Wang, R. Garcia-Mendez, J. Sakamoto, Demonstration of high current densities and extended cycling in the garnet $Li_7La_3Zr_2O_{12}$ solid electrolyte, Journal of Power Sources 396 (2018) 314-318.

[40] J. Liu, X. Gao, G.O. Hartley, G.J. Rees, C. Gong, F.H. Richter, J. Janek, Y. Xia, A.W. Robertson, L.R. Johnson, The interface between $Li_{6.5}La_3Zr_{1.5}Ta_{0.5}O_{12}$ and liquid electrolyte, Joule 4(1) (2020) 101-108.

[41] L. Dahéron, R. Dedryvère, H. Martinez, M. Ménétrier, C. Denage, C. Delmas, D. Gonbeau, Electron transfer mechanisms upon lithium deintercalation from $LiCoO_2$ to CoO_2 investigated by XPS, Chemistry of Materials 20(2) (2008) 583-590.

[42] C.J. Jafta, X.-G. Sun, G.M. Veith, G.V. Jensen, S.M. Mahurin, M.P. Paranthaman, S. Dai, C.A. Bridges, Probing microstructure and electrolyte concentration dependent cell chemistry via operando small angle neutron scattering, Energy & Environmental Science 12(6) (2019) 1866-1877.

[43] F. Borghi, C. Piazzoni, M. Ghidelli, P. Milani, A. Podestà, Nanoconfinement of ionic liquid into porous carbon electrodes, The Journal of Physical Chemistry C 125(2) (2021) 1292-1303.

[44] E.J. Cheng, M. Liu, Y. Li, T. Abe, K. Kanamura, Effects of porosity and ionic liquid impregnation on ionic conductivity of garnet-based flexible sheet electrolytes, Journal of Power Sources 517 (2022) 230705.

[45] T. Mandai, K. Yoshida, K. Ueno, K. Dokko, M. Watanabe, Criteria for solvate ionic liquids, Physical Chemistry Chemical Physics 16(19) (2014) 8761-8772.

[46] T. Ma, G.-L. Xu, Y. Li, L. Wang, X. He, J. Zheng, J. Liu, M.H. Engelhard, P. Zapol, L.A. Curtiss, Revisiting the corrosion of the aluminum current collector in lithium-ion batteries, The Journal of Physical Chemistry Letters 8(5) (2017) 1072-1077.

[47] Y. Wang, Q. Zhang, Z.C. Xue, L. Yang, J. Wang, F. Meng, Q. Li, H. Pan, J.N. Zhang, Z. Jiang, An In Situ Formed Surface Coating Layer Enabling $LiCoO_2$ with Stable 4.6 V High-Voltage Cycle Performances, Advanced Energy Materials 10(28) (2020) 2001413.

[48] M. Kotobuki, K. Kanamura, Y. Sato, T. Yoshida, Fabrication of all-solid-state lithium battery with lithium metal anode using Al_2O_3-added $Li_7La_3Zr_2O_{12}$ solid electrolyte, Journal of Power Sources 196(18) (2011) 7750-7754.

Chapter 6 Preparation of all-solid-state Li metal batteries by aerosol deposition

6.1 Abstract

High-energy-density and safe rechargeable batteries are key components to realizing a low-carbon society. All-solid-state Li-metal batteries have the potential to achieve both high safety and high energy densities. However, the large interfacial resistance between solid electrolytes and cathodes is the major challenge for developing all-solid-state Li-metal batteries. Here we deposited a Li-rich layered metal oxide $Li_{1.2}Mn_{0.54}Ni_{0.13}Co_{0.13}O_2$ (LMNC) thin film (6 μm thick) on an Al-doped $Li_7La_3Zr_2O_{12}$ (LLZO) substrate at room temperature by aerosol deposition. The LMNC particles were coated with Li_3BO_3 (LBO), which acted as a binder to hold LMNC and LLZO together at heating. As a result, good interfacial contact was achieved between LMNC and LLZO. Yet reactions between LMNC and LBO would occur at heat treatment temperatures above 600 °C. The highest discharge capacity of the all-solid-state Li/LLZO/LBO-LMNC cell at 0.1 C and 60 °C was 223 mAh g^{-1}. The main reason for the cell capacity decay was the cracking of the LBO-LMNC cathode layer during cycling. Searching for a more suitable binder material with a high fracture toughness is crucial for further developing aerosol-deposited LLZO-based all-solid-state Li metal batteries.

6.2 Introduction

Carbon dioxide (CO_2) is the primary greenhouse gas emitted through human activities, such as the combustion of petroleum, natural gas, and coal, for energy and transportation. In 2021, transport accounted for 37% of CO_2 emissions from end-use sectors [1]. As a result, a crucial step in tackling the climate emergency is reducing transportation emissions, which can be realized by replacing gasoline cars with electric vehicles (EVs).

However, the EV industry is concerned with maximizing vehicle driving range and safety. The driving range is a direct function of the discharge capacity of the EV battery pack. As a result, Li-rich layered cathode materials, such as LMNC, are of great interest because of their high discharge capacity of above 250 mA h g^{-1} and high operating voltage [2, 3]. LMNC consists of two layered cathodes in a solid solution form of $xLi_2MnO_3 \cdot (1-x)LiMO_2$, where M represents a transition metal, e.g., Co) [4, 5]. The crystal structure of LMNC is illustrated in Figure 1 [6], where oxygen atoms are in the octahedral sites of the alternating layers of Li and transition metals (Mn, Ni, and Co). In addition to mileage, safety is also a significant challenge for EVs. State-of-the-art Li-ion batteries with conventional liquid electrolytes are potentially dangerous because the liquid electrolytes are generally highly flammable, posing a risk of fire and explosion.

On the other hand, all-solid-state Li metal batteries have the potential to achieve both high safety and high energy densities and thus have attracted tremendous research interest. Nevertheless, among various solid-state fast-ion conductors, few are stable against Li metal, which is widely regarded as the ultimate anode material. The garnet-type oxide, LLZO, shows relatively high chemical and electrochemical stabilities against metallic Li and is considered one of the most promising solid electrolytes.

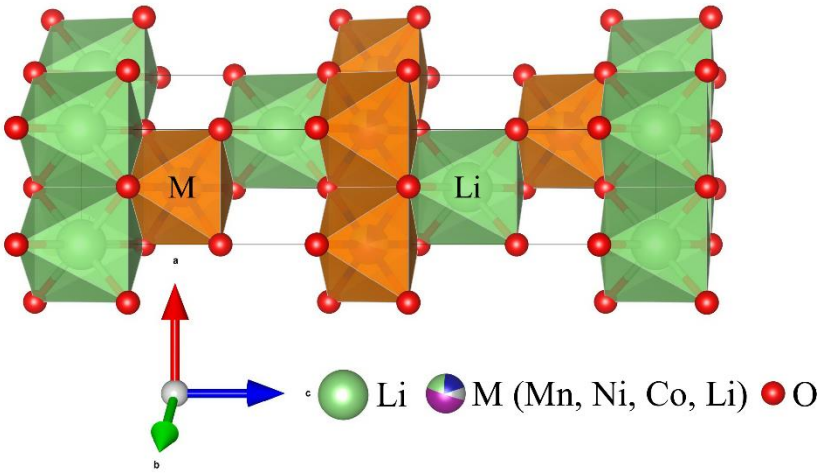

Figure 6.1 Crystal structure of $Li_{1.2}Mn_{0.54}Ni_{0.13}Co_{0.13}O_2$ (LMNC)

However, forming good interfacial contact between LLZO and the electrode materials is challenging because LLZO has a high elastic modulus [7]. The high interfacial resistance presents a significant barrier to developing all-solid-state Li-metal batteries. A great effort has been made to decrease the interfacial resistance between LLZO and the Li metal anode [8, 9]. For instance, the LLZO/Li interfacial resistance can be effectively reduced by introducing a thin Au or Al_2O_3 interlayer [10, 11]. Good contact between LLZO and Li metal can also be achieved by high pressure and heating because Li metal is ductile and has a relatively low melting point of 180.5 °C [12, 13].

In contrast, much less effort has been devoted to reducing the interfacial resistance between LLZO and the cathode materials [14]. Although it is possible to achieve good interfacial contact between cathodes and ceramic solid electrolytes by co-sintering, high sintering temperatures may cause chemical decomposition of the cathode materials [15, 16]. Developing ionic liquid-containing cathodes was a convenient and effective way to reduce the cathode/solid electrolyte interfacial resistance [17, 18]. Polymer-in-LLZO flexible sheet electrolytes were also proposed to optimize the physical contact between solid electrolytes and cathode materials [19, 20]. Nevertheless, introducing a liquid electrolyte or applying a polymer-based flexible electrolyte to

reduce the interfacial resistance will compromise battery safety [21]. For example, the most widely used poly(ethylene oxide) solid-state polymer electrolyte (PEO) is flammable [22, 23]. Thermally soldering cathodes and solid electrolytes with a low-melting-point solid electrolyte was a relatively new approach to mitigating interfacial resistance [21]. Aerosol deposition (AD) is a room-temperature coating technology used to deposit cathode films on ceramic electrolytes [24, 25]. An illustration of the AD system is shown in Figure 2**A**. Accelerated particles are cracked and deformed when hitting the ceramic substrate (Figures 2**B** and **C**). The high surface energy generated from particle fracture or plastic deformation is likely to be the driving force for the densification of small particles at room temperature [26]. However, ceramic-based all-solid-state Li metal batteries prepared by AD almost cannot work and degrade rapidly with cycling, most likely due to the poor interfacial contact and the further degradation of the electrode-solid electrolyte interface [27]. The stresses generated by the insertion and extraction of Li-ions into and out of the cathode materials can result in the cracking of the interface. As a result, further interface engineering is needed to reduce the large interfacial resistance and maintain the integrity of the cathode-solid electrolyte interface created by AD. For example, the deposited cathode layer and the ceramic electrolyte can be joined together with a low-melting-point solid electrolyte binder at heating (Figure 2**D**).

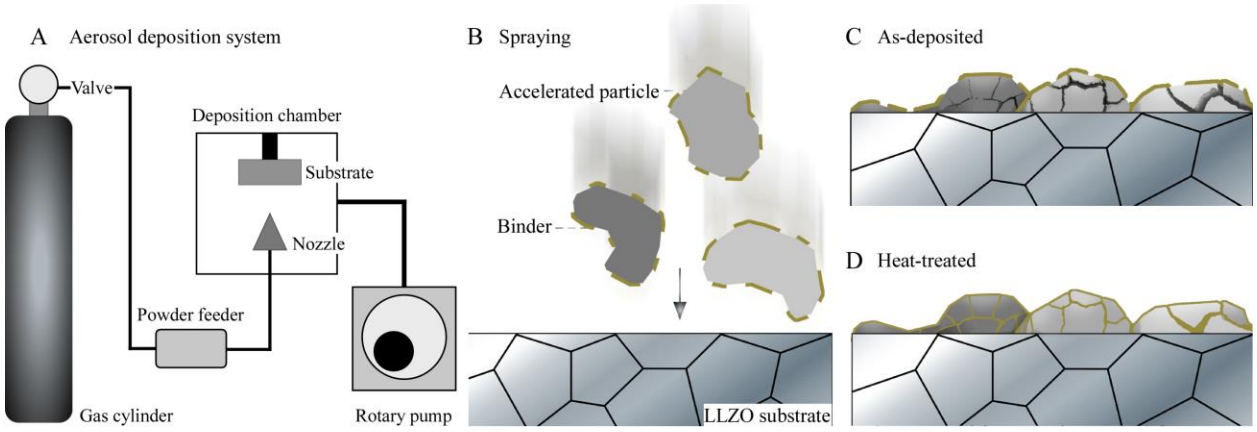

Figure 6.2 Illustration of the AD process. (**A**) Illustration of the AD system, (**B**) Accelerated binder-coated cathode particles hitting onto an LLZO substrate, (**C**) As-deposited cathode layer, where the particles are cracked and deformed, (**D**) Heat-treated cathode layer, where a low-melting-point binder material fills the cracks and voids upon sintering or melting.

Here an LBO-LMNC cathode film was deposited on an Al-doped LLZO substrate at room temperature by AD. Upon heating, the cracks of the deposited LMNC particles and the voids between the LMNC cathode layer and the LLZO substrate were filled by LBO, a mechanically soft solid electrolyte with a relatively low melting point of around 700 °C [28]. All-solid-state Li/LLZO/LBO-LMNC cells were assembled, and the electrochemical performance was evaluated.

6.3 Experiment

6.3.1 Synthesis of Li_3BO_3 (LBO)

The LBO powder was synthesized by heating mixtures of Li_2CO_3 (99.0%, FUJIFILM Wako Pure Chemical Corporation, Japan) and B_2O_3 (95%, Kanto Chemical Co., Inc., Japan) in a molar ratio of 3:1 at 600 °C for 10 h in air. The LBO powder was further pulverized to reduce the particle size and the crystallinity by ball milling (400 rpm, 10 min milling followed by a 20 min pause to

avoid overheating, repeated 99 times). Figure S1 shows the XRD pattern of the synthesized LBO powder.

6.3.2 Synthesis of $Li_{1.2}Mn_{0.54}Ni_{0.13}Co_{0.13}O_2$ (LMNC)

The LMNC powder was synthesized through a co-precipitation process in combination with a solid-state reaction [29, 30]. The first step was synthesizing an Mn-Ni-Co hydroxide precursor through a co-precipitation process. Starting materials of $Mn(NO_3)_2 \cdot 6H_2O$ (98%, FUJIFILM Wako Pure Chemical Corp.), $Ni(NO_3)_2 \cdot 6H_2O$ (98%, FUJIFILM Wako Pure Chemical Corp.), $Co(NO_3) \cdot 6H_2O$ (98%, FUJIFILM Wako Pure Chemical Corp.) were dissolved in water to form a solution, which was added dropwise to a 0.5 mol dm^{-3} $LiOH \cdot H_2O$ basic solution. The precipitate was carefully filtered, washed with distilled water, and dried at 120 °C for 12 h. The second step was synthesizing LMNC from a solid-state reaction between the precipitate and $LiOH \cdot H_2O$. After drying, the precipitate was mixed with a stoichiometric amount of $LiOH \cdot H_2O$ (99%, FUJIFILM Wako Pure Chemical Corp.) and calcined at 500 °C for 4 h and then at 900 °C for 8 h in air.

6.3.3 Synthesis of Al-LLZO

The Al-doped LLZO powder was prepared by a solid-state reaction method. Starting materials of $LiOH \cdot H_2O$, $La(OH)_3$, and ZrO_2 powders were mixed by ball-milling and calcined at 900 °C for 15 h. After mixing with a nano-sized γ-Al_2O_3 powder, the calcined powder was compacted and sintered at 900 °C for 3 h and then at 1200 °C for 24 h in air. The molar ratio of $LiOH \cdot H_2O$, $La(OH)_3$, ZrO_2, and γ-Al_2O_3 was 6.9: 3.0 : 2.0: 0.125. The XRD pattern of the synthesized Al-doped LLZO pellet shows a cubic structure of Ia-3d (Figure S2) [31].

6.3.4 Aerosol Deposition

The LBO and LMNC powders in mass ratios of 0:10, 1:9, and 2:8 were ball-milled at 400 rpm for 30 min, following calcination in the temperature range of 400-700 °C for 2 h in air. The LBO-coated LMNC was transferred into the deposition chamber, which was evacuated by a rotary pump to 80 Pa. The diameter of the nozzle hole was 1 mm, and the deposition area on the LLZO substrat1e was about 0.785 cm^2. The distance between the LLZO substrate and the nozzle was 40 mm. The Ar gas pressure was set to 0.6 MPa. The amount of LBO-LMNC deposited on the LLZO substrate was determined from the weight increase of the LLZO substrate after deposition.

6.3.5 Materials characterization

The crystal structures were analyzed by X-ray diffraction (XRD, Cu Kα radiation, Rigaku SmartLab). The step size was 0.01°, and the scanning speed was 1°/min. The X-ray diffractometer was operated at 40 kV and 40 mA. The microstructure was analyzed by a scanning electron microscope (SEM, JSM-6490A, JEOL). The accelerating voltage was 15 kV, and the working distance was 10 mm. The particle size of the synthesized LMNC powder was measured by dynamic light scattering (DLS, DLS-8000 series, Otsuka Electronics Co., Ltd.). The density of the Al-doped LLZO was determined by measuring its weight and dimensions. The crystal structure of LMNC was illustrated using VESTA [32].

6.3.6 Electrochemical measurements

AC electrochemical impedance spectroscopy (EIS) was performed in the frequency range from 3 MHz to 0.1 Hz at 30-60 °C (Biologic SP-300, France). The amplitude of the perturbation was 10 mV. The EIS spectrum of the Al-doped LLZO pellet is shown in Fig. S3**A**, and the Arrhenius plot in Fig. S3**B**. CR2032 coin cells were assembled to evaluate the effect of the LBO coating on the discharge capacity of the LMNC cathode. The anode was a Li metal disc (600 μm thick, Honjo

Metal CO., Ltd.), and the liquid electrolyte was 1 mol dm^{-3} $LiPF_6$/EC: DMC (1:1). Galvanostatic cycling of the all-solid-state Li/LLZO/LBO-LMNC cells was carried out at 0.1 C and 60 • ‹C with a cut-off voltage range of 2.0-4.8 V. The surface of the LBO-LMNC cathode layer facing an Al current collector was coated with a thin Au layer for electron transfer. The configuration of the Li/LLZO/LBO-LMNC cell is illustrated in Fig. S4**A**. A UFO-shaped battery testing apparatus was designed and built for the cycling test, as shown in Fig. S4**B**. The EIS data were fitted to equivalent electrical circuit models using the EC-Lab software (Biologic, France).

6.4 Results and discussions

6.4.1 Synthesized LMNC powder

The synthesized LMNC powder showed a crystalline structure with $R\bar{3}m$ symmetry, as confirmed by X-ray diffraction (Figure 6.3**A**) [33]. No impurity phase was identified. The main diffraction peaks were assigned to the layered component of $LiMO_2$ (M= Mn, Ni, Co), while the weak bumps between 21° and 23° were assigned to the Li_2MnO_3 component (space group: C2/m) in the transition metal layers [34, 35]. The particle size was about 0.2-5 µm (Figure 6.3**B**), and the average particle diameter was measured to be around 2.3 µm (Figure 6.3**C**), located in the range of optimal particle size for AD, 0.1 to 10 µm.

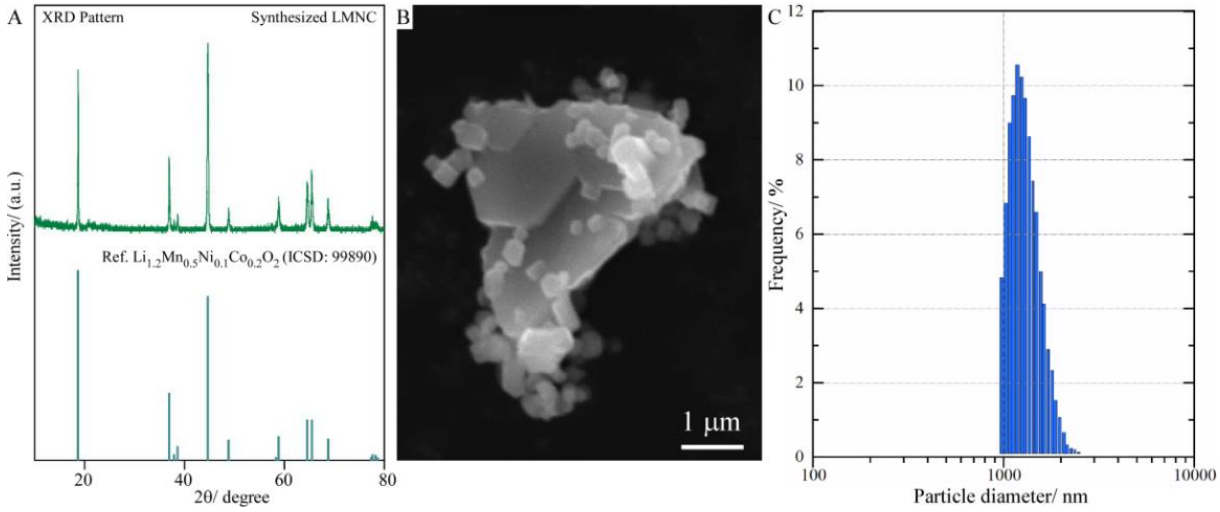

Figure 6.3 As-synthesized LMNC powder. (**A**) The XRD pattern of the synthesized LMNC powder, (**B**) An SEM micrograph of the LMNC powder, (**C**) Particle size distribution

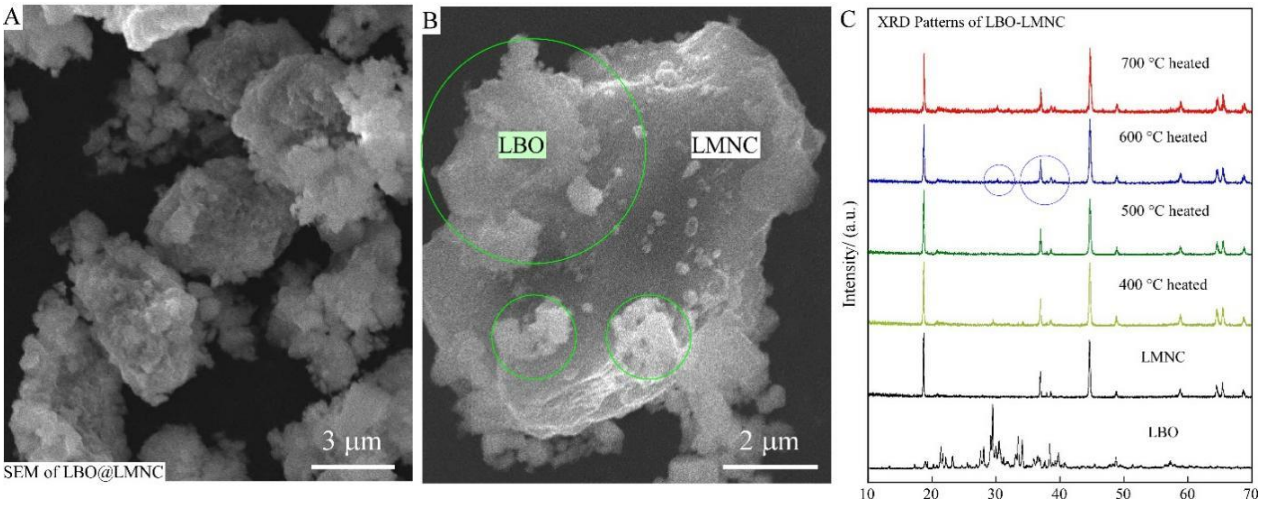

Figure 6.4 (**A**) LBO-coated LMNC. (**A**) An SEM micrograph of the LBO-coated LMNC powder (The mass ratio between LBO and LMNC is 2:8), (**B**) A high-resolution SEM micrograph showing the amorphous-like LBO attached to the surface of an LMNC particle, (**C**) XRD patterns of the LBO-LMNC powders heat-treated at different temperatures. For the XRD measurements, the mass ratio between LBO and LMNC is changed to 1:1 here to increase the peak intensity of LBO for analysis because the degree of crystallinity of LBO is relatively low.

6.4.2 Microstructure and phase of the synthesized LBO-coated LMNC

The LBO powder was synthesized through a solid-state reaction between lithium carbonate (Li_2CO_3) and boron trioxide (B_2O_3):

$$3Li_2CO_3 + B_2O_3 = 2Li_3BO_3 + 3CO_2 \qquad (6\text{-}1)$$

The synthesized LBO and LMNC powders were mixed by ball-milling and heated in air to obtain an LBO-coated LMNC cathode material (Figure 4**A**). The pulverized LBO powder was amorphous-like (Figure 4**B**) and attached to the surface of the LMNC particle. As indicated by the

XRD analysis, the crystallinity of the LBO powder was relatively low (Figure 4**C**). As indicated by the dashed lines, additional peaks around 30° and 39° were observed in the XRD pattern of the 600 °C heat-treated LBO-LMNC powder. Moreover, the peak intensities increased when the heat treatment temperature rose to 700 °C. Thus, the optimized co-sintering temperature should be less than 600 °C to avoid a reaction between LBO and LMNC.

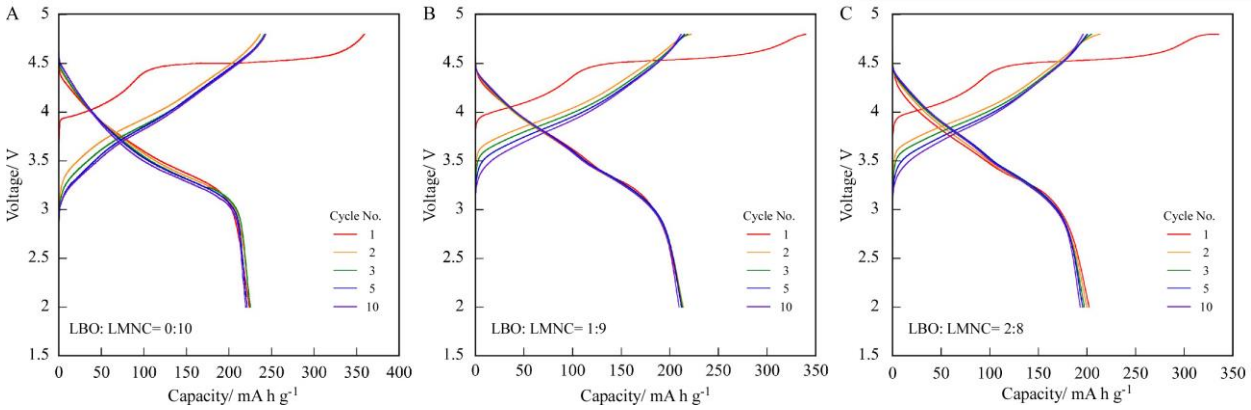

Figure 6.5 Galvanostatic cycling profiles of the Li/LBO-LMNC cells with a liquid electrolyte of 1 mol dm^{-3} $LiPF_6$/EC: DMC (1:1) at 0.1 C and 30 °C. (**A**) LMNC without LBO coating, (**B**) LBO: LMNC= 1:9 (Mass ratio), (**C**) LBO: LMNC= 2:8. The LMNC active material loading is in the range of 1.6-2.4 mg cm^{-2}.

6.4.3 Cycling performance of the LBO-coated LMNC cathode in liquid cells

Figure 6.5 shows the galvanostatic cycling profiles of the Li/LBO-LMNC cells with a liquid electrolyte of 1 mol dm^{-3} $LiPF_6$/EC: DMC (1:1) at 0.1 C and 30 °C. The irreversible loss of the first-charging plateau at about 4.5 V was suggested to be associated with oxygen (O^{2-}) redox and corresponding phase transition [35, 36]. After discharging, the distorted oxygen sublattice could not recover fully to the pristine state, thereby decreasing the structural stability and the discharge capacity. Nevertheless, the initial discharge capacity of the LMNC cathode still reached 248 mA h

g^{-1}, which increased to the highest value of 260 mA h g^{-1} in the third cycle. The initial discharge capacity of LMNC decreased slightly to 220 mA h g^{-1} when coated with 10 wt% LBO (Fig. 5**B**) and further decreased to 200 mA h g^{-1} when coated with 20% LBO (Fig. 5**C**). The decrease in capacity can be explained by the fact that the ionic conductivity of LBO (about 10^{-6} S cm^{-1} at 25 °C) is much lower than that of the liquid electrolyte (about 10^{-2} S cm^{-1} at 25 °C). As a result, the kinetics of Li-ion transfer and diffusion would be retarded by the LBO coating, although the LMNC cathode was not fully covered by LBO.

Nevertheless, the results showed that the discharge capacity of LMNC was only slightly decreased when coated with a moderate amount of LBO. Besides, the LBO-coated LMNC could be a promising cathode material for all-solid-state Li metal batteries with ceramic solid electrolytes because LBO could function as a binder to hold LMNC and the ceramic solid electrolyte together at heating.

6.4.4 Cycling performance of an all-solid-state Li/LLZO/LBO-LMNC cell

An SEM cross-sectional micrograph of the high-temperature sintered Al-doped LLZO pellet is shown in Fig. 6**A**, where a few pores are observed. The relative density of the Al-doped LLZO pellet was estimated to be 95%. Fig. 6**B** shows an SEM cross-section of the LBO-LMNC/LLZO interface area, where almost no voids or cracks can be observed in the LBO-LMNC cathode layer. The cathode layer, about 6 μm in thickness, was deposited onto the LLZO substrate by AD at room temperature, following heat treatment at 500 °C for 2 h in air. Although the LBO-LMNC cathode shrank slightly after heat treatment because of the sintering of LBO, it still maintained good contact with the LLZO substrate. The galvanostatic cycling profile of the Li/LLZO/LBO-LMNC all-solid-state cell at 0.1 C and 60 °C is shown in Fig. 6**C**. The initial discharge capacity was 200 mA h g^{-1}, which increased to the highest value of 223 mA h g^{-1} in the second cycle. In general, rapid capacity

fading was observed with cycling, and the capacity retention was 92 % after 10 cycles (Fig. 7**C**). However, this result still represents one of the best results reported for aerosol-deposited all-solid-state Li metal batteries with ceramic electrolytes [13, 24, 37].

In contrast, it was difficult to charge and discharge the LBO-free Li/LLZO/LMNC cell, suggesting that the LBO coating was critical for the functioning of the aerosol-deposited all-solid-state cell. Nevertheless, the cell capacity fading was significant with cycling, mainly due to the cracking of the LBO-LMNC cathode layer, as indicated by the arrowheads in Fig. 6**D**. The cracks were primarily concentrated in the LBO-LMNC cathode layer and close to the cathode/solid electrolyte interface. On the other hand, no apparent cracks were observed in the LBO-LMNC cathode layer before cycling (Figure 6**B**). In addition, local contact loss between the LBO-LMNC cathode and the LLZO electrolyte was also observed. The cracking and contact loss were believed to be caused by the volume variation of the LMNC cathode during cycling. Thus, identifying a more suitable solid-electrolyte binder with a high fracture toughness to withstand the volume change of the cathode active material is critical for further developing the aerosol-deposited LLZO-based all-solid-state Li metal batteries.

An SEM cross-sectional micrograph of the high-temperature sintered Al-doped LLZO pellet is shown in Figure 6**A**, where a few pores are observed. The relative density of the Al-doped LLZO pellet was estimated to be 95%. Figure 6.6**B** shows an SEM cross-section of the LBO-LMNC/LLZO interface area, where almost no voids or cracks can be observed. The LBO-LMNC cathode layer (about 6 μm in thickness) was deposited onto the LLZO substrate by AD at room temperature, following heat treatment at 500 °C for 2 h in air. Although the LBO-LMNC cathode shrank slightly after heat treatment because of the difference in coefficient of thermal expansion (CTE) between LBO-LMNC and LLZO, it maintained good contact with the LLZO substrate.

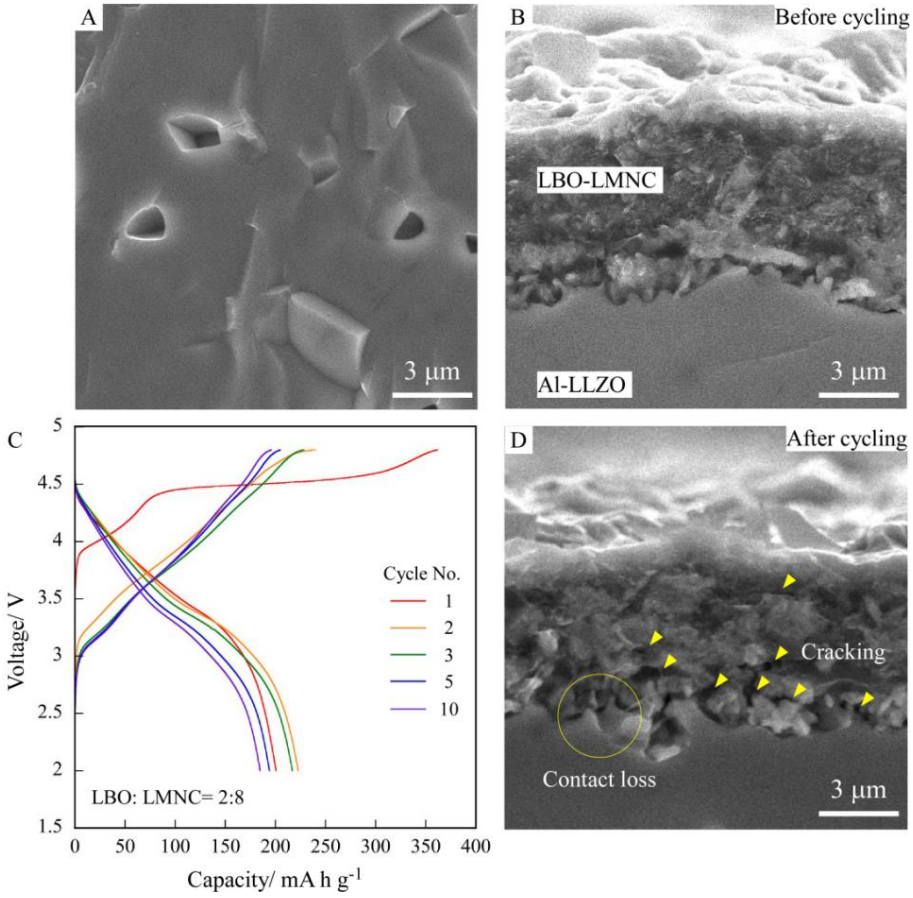

Figure 6.6 SEM cross-sectional micrographs of the high-temperature sintered Al-doped LLZO pellet (**A**) and the LBO-LMNC/LLZO interface regional (**B**). The mass ratio between LBO and LMNC is 2:8.

6.5 Conclusions

A 6 μm-thick LBO-LMNC cathode thin film was deposited on an Al-doped LLZO substrate at room temperature by aerosol disposition. LBO functioned as a Li-ion-conducting binder that filled the cracks and the voids between the LMNC cathode layer and the LLZO ceramic electrolyte at heating. However, reactions between LMNC and LBO occurred at temperatures above 600 °C. The highest discharge capacity of the all-solid-state Li/LLZO/LBO-LMNC cell at 0.1 C and 60 °C reached 223 mAh g^{-1}. Although the cell capacity retention was only 92 % after 10 cycles, the result still represents one of the best reported for all-solid-state Li metal batteries with ceramic electrolytes. The cell capacity degradation was mainly caused by the cracking of the LBO-LMNC cathode layer during cycling. Nevertheless, the LBO coating was necessary for the functioning of the all-solid-state Li/LLZO/LBO-LMNC cell. Identifying a more suitable coating material is crucial for further improving the cyclability of the high-voltage all-solid-state Li metal batteries prepared by AD.

6.7 Supplementary Information

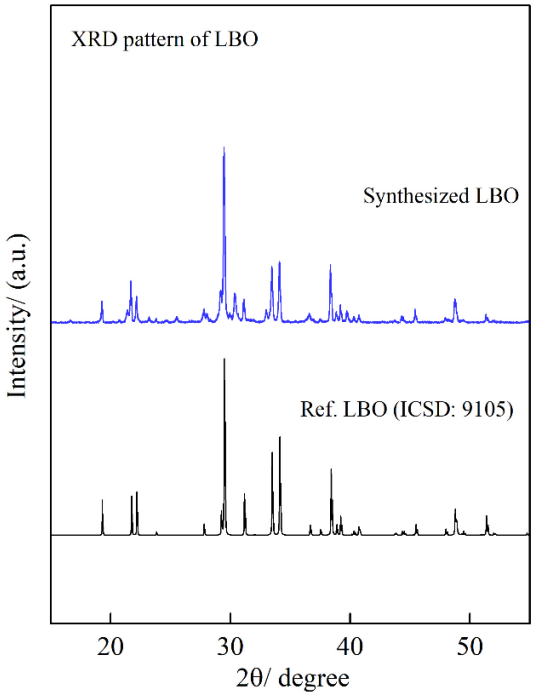

Figure 6 S1 XRD pattern of the synthesized LBO powder, which has a crystalline structure and an average particle size of less than 1.0 μm.

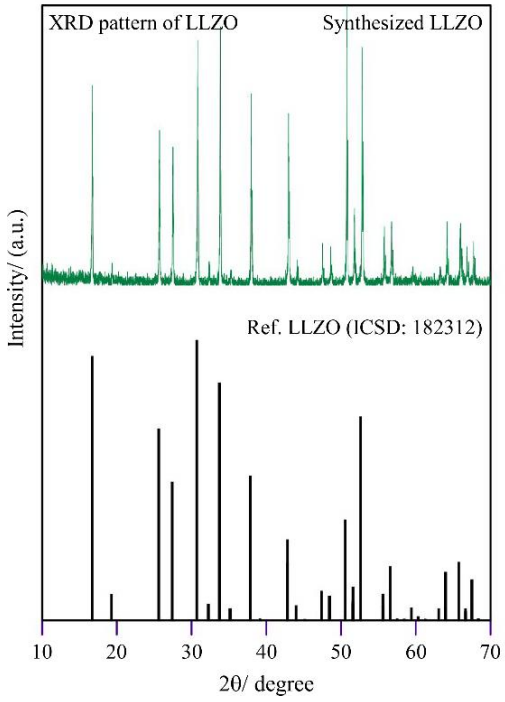

Figure 6 S2 XRD pattern of the prepared Al-doped LLZO pellet, which has a cubic structure.

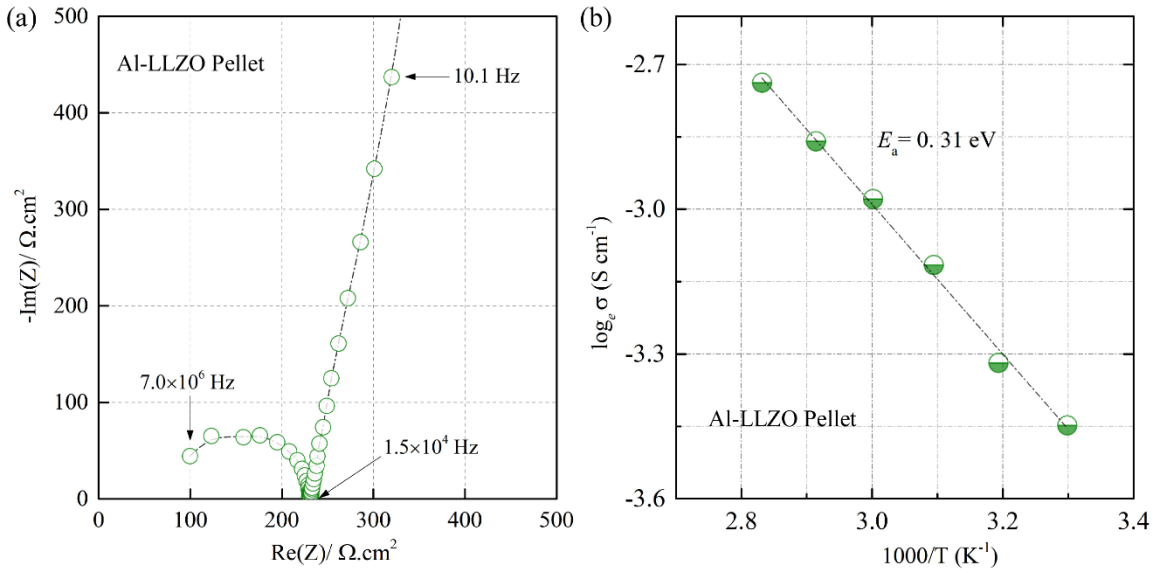

Figure 6 S3 (**A**) EIS spectrum of the synthesized Al-doped LLZO pellet measured at 25-30°C from 3 MHz to 0.1 Hz. The pellets' thickness was 400-500 μm, and the ionic conductivity was about 3.6×10^{-4} S cm^{-1} at 30 °C, (**B**) Arrhenius conductivity of the Al-doped LLZO pellet.

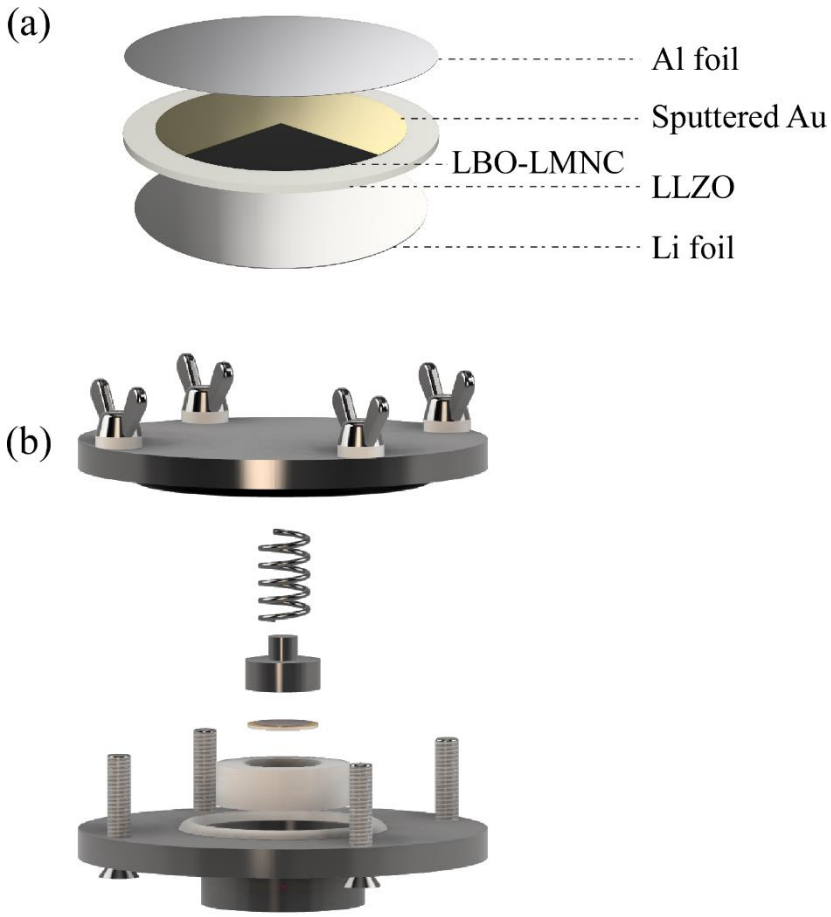

Figure 6 S4 (a) Configuration of the Li/Al-doped LLZO/LBO-LMNC cell, (b) A UFO-shaped battery apparatus designed and built for the cycling test.

Reference

[1] IEA, Paris, https://www.iea.org/topics/transport

[2] M.M. Thackeray, C.S. Johnson, J.T. Vaughey, N. Li, S.A. Hackney, Advances in manganese-oxide 'composite' electrodes for lithium-ion batteries, Journal of Materials Chemistry 15(23) (2005) 2257-2267.

[3] L. Ming, B. Zhang, Y. Cao, J.F. Zhang, C.H. Wang, X.W. Wang, H. Li, Effect of Nb and F co-doping on $Li_{1.2}Mn_{0.54}Ni_{0.13}Co_{0.13}O_2$ cathode material for high-performance lithium-ion batteries, Frontiers in chemistry 6 (2018) 76.

[4] J.S. Kim, C. Johnson, M. Thackeray, Layered $x LiMO_2 \cdot (1-x) Li_2M'O_3$ electrodes for lithium batteries: a study of 0.95 LiMn0. 5Ni0. 5O2· 0.05 Li2TiO3, Electrochemistry communications 4(3) (2002) 205-209.

[5] M. Thackeray, S.H. Kang, C. Johnson, J. Vaughey, S. Hackney, Comments on the structural complexity of lithium-rich $Li_{1+x}M_{1-x}O_2$ electrodes (M= Mn, Ni, Co) for lithium batteries, Electrochemistry Communications 8(9) (2006) 1531-1538.

[6] K.S. Park, M.H. Cho, S.J. Jin, K.S. Nahm, Y. Hong, Effect of Li ion in transition metal sites on electrochemical behavior of layered lithium manganese oxides solid solutions, Solid State Ionics 171(1-2) (2004) 141-146.

[7] S. Yu, R.D. Schmidt, R. Garcia-Mendez, E. Herbert, N.J. Dudney, J.B. Wolfenstine, J. Sakamoto, D.J. Siegel, Elastic properties of the solid electrolyte $Li_7La_3Zr_2O_{12}$ (LLZO), Chemistry of Materials 28(1) (2016) 197-206.

[8] A. Sharafi, E. Kazyak, A.L. Davis, S. Yu, T. Thompson, D.J. Siegel, N.P. Dasgupta, J. Sakamoto, Surface chemistry mechanism of ultra-low interfacial resistance in the solid-state electrolyte $Li_7La_3Zr_2O_{12}$, Chemistry of Materials 29(18) (2017) 7961-7968.

[9] X. Xiang, Y. Zhang, H. Wang, C. Wei, F. Chen, Q. Shen, Improving the Interfacial Contact between $Li_7La_3Zr_2O_{12}$ and Lithium Anode by Depositing a Film of Silver, Journal of The Electrochemical Society 168(6) (2021) 060515.

[10] X. Han, Y. Gong, K.K. Fu, X. He, G.T. Hitz, J. Dai, A. Pearse, B. Liu, H. Wang, G. Rubloff, Negating interfacial impedance in garnet-based solid-state Li metal batteries, Nature Materials 16(5) (2017) 572.

[11] C.L. Tsai, V. Roddatis, C.V. Chandran, Q. Ma, S. Uhlenbruck, M. Bram, P. Heitjans, O. Guillon, $Li_7La_3Zr_2O_{12}$ interface modification for Li dendrite prevention, ACS applied materials & interfaces 8(16) (2016) 10617-10626.

[12] H. Zheng, S. Wu, R. Tian, Z. Xu, H. Zhu, H. Duan, H. Liu, Intrinsic lithiophilicity of Li–garnet electrolytes enabling high-rate lithium cycling, Advanced Functional Materials 30(6) (2020) 1906189.

[13] R. Inada, S. Yasuda, H. Hosokawa, M. Saito, T. Tojo, Y. Sakurai, Formation and stability of interface between garnet-type Ta-doped $Li_7La_3Zr_2O_{12}$ solid electrolyte and lithium metal electrode, Batteries 4(2) (2018) 26.

[14] W. Huang, Z. Bi, N. Zhao, Q. Sun, X. Guo, Chemical interface engineering of solid garnet batteries for long-life and high-rate performance, Chemical Engineering Journal 424 (2021) 130423.

[15] K.J. Kim, J.L. Rupp, All ceramic cathode composite design and manufacturing towards low interfacial resistance for garnet-based solid-state lithium batteries, Energy & Environmental Science 13(12) (2020) 4930-4945.

[16] E.J. Cheng, N.J. Taylor, J. Wolfenstine, J. Sakamoto, Elastic properties of lithium cobalt oxide ($LiCoO_2$), Journal of Asian Ceramic Societies 5(2) (2017) 113-117.

[17] C.Z. Zhao, B.C. Zhao, C. Yan, X.Q. Zhang, J.Q. Huang, Y. Mo, X. Xu, H. Li, Q. Zhang, Liquid phase therapy to solid electrolyte–electrode interface in solid-state Li metal batteries: a review, Energy Storage Materials 24 (2020) 75-84.

[18] E.J. Cheng, M. Shoji, T. Abe, K. Kanamura, Ionic liquid-containing cathodes empowering ceramic solid electrolytes, Iscience 25(3) (2022) 103896.

[19] E.J. Cheng, T. Kimura, M. Shoji, H. Ueda, H. Munakata, K. Kanamura, Ceramic-based flexible sheet electrolyte for Li batteries, ACS Applied Materials & Interfaces 12(9) (2020) 10382-10388.

[20] E.J. Cheng, M. Liu, Y. Li, T. Abe, K. Kanamura, Effects of porosity and ionic liquid impregnation on ionic conductivity of garnet-based flexible sheet electrolytes, Journal of Power Sources 517 (2022) 230705.

[21] F. Han, J. Yue, C. Chen, N. Zhao, X. Fan, Z. Ma, T. Gao, F. Wang, X. Guo, C. Wang, Interphase engineering enabled all-ceramic lithium battery, Joule 2(3) (2018) 497-508.

[22] L. Han, C. Liao, X. Mu, N. Wu, Z. Xu, J. Wang, L. Song, Y. Kan, Y. Hu, Flame-Retardant ADP/PEO Solid Polymer Electrolyte for Dendrite-Free and Long-Life Lithium Battery by Generating Al, P-rich SEI Layer, Nano Letters 21(10) (2021) 4447-4453.

[23] X. Liu, C. Zhang, S. Gao, S. Cai, Q. Wang, J. Liu, Z. Liu, A novel polyphosphonate flame-retardant additive towards safety-reinforced all-solid-state polymer electrolyte, Materials Chemistry and Physics 239 (2020) 122014.

[24] S. Iwasaki, T. Hamanaka, T. Yamakawa, W.C. West, K. Yamamoto, M. Motoyama, T. Hirayama, Y. Iriyama, Preparation of thick-film $LiNi_{1/3}Co_{1/3}Mn_{1/3}O_2$ electrodes by aerosol deposition and its application to all-solid-state batteries, Journal of Power Sources 272 (2014) 1086-1090.

[25] M. Sakakura, Y. Suzuki, T. Yamamoto, Y. Yamamoto, M. Motoyama, Y. Iriyama, Low-Resistive $LiCoO_2/Li_{1.3}Al_{0.3}Ti_2(PO_4)_3$ Interface Formation by Low-Temperature Annealing Using Aerosol Deposition, Energy Technology 9(5) (2021) 2001059.

[26] J. Akedo, Aerosol deposition of ceramic thick films at room temperature: densification mechanism of ceramic layers, Journal of the American Ceramic Society 89(6) (2006) 1834-1839.

[27] T. Kato, S. Iwasaki, Y. Ishii, M. Motoyama, W.C. West, Y. Yamamoto, Y. Iriyama, Preparation of thick-film electrode-solid electrolyte composites on $Li_7La_3Zr_2O_{12}$ and their electrochemical properties, Journal of Power Sources 303 (2016) 65-72.

[28] M. Shoji, H. Munakata, K. Kanamura, Fabrication of all-solid-state lithium-ion cells using three-dimensionally structured solid electrolyte $Li_7La_3Zr_2O_{12}$ pellets, Frontiers in Energy Research 4 (2016) 32.

[29] C.S. Johnson, N. Li, C. Lefief, J.T. Vaughey, M.M. Thackeray, Synthesis, Characterization and Electrochemistry of Lithium Battery Electrodes: $x\mathrm{Li_2MnO_3}\cdot(1-x)\mathrm{LiMn_{0.333}Ni_{0.333}Co_{0.333}O_2}$ ($0\leq x\leq 0.7$), Chem. Mater. 20 (2008) 6095–6106.

[30] N. Ishida, R. Nishigami, N. Kitamura, Y. Idemoto, Crystal structure analysis and electrochemical properties of chemically delithiated $\mathrm{Li_{0.13}Mn_{0.54}Ni_{0.13}Co_{0.13}O_{2-\delta}}$ as cathode material for rechargeable mg batteries, Chemistry Letters 46(10) (2017) 1508-1511.

[31] R. Wagner, G.n.J. Redhammer, D. Rettenwander, A. Senyshyn, W. Schmidt, M. Wilkening, G. Amthauer, Crystal structure of garnet-related Li-ion conductor $\mathrm{Li_{7-3x}Ga}x\mathrm{La_3Zr_2O_{12}}$: fast Li-ion conduction caused by a different cubic modification, Chemistry of Materials 28(6) (2016) 1861-1871.

[32] K. Momma, F. Izumi, VESTA 3 for three-dimensional visualization of crystal, volumetric and morphology data, Journal of applied crystallography 44(6) (2011) 1272-1276.

[33] N. Ishida, R. Nishigami, M. Matsui, T. Mandai, K. Kanamura, N. Kitamura, Y. Idemoto, Revisiting Delithiated $\mathrm{Li_{1.2}Mn_{0.54}Ni_{0.13}Co_{0.13}O_2}$: Structural Analysis and Cathode Properties in Magnesium Rechargeable Battery Applications, Electrochemistry (2021) 21-00038.

[34] C. Johnson, J. Kim, C. Lefief, N. Li, J. Vaughey, M. Thackeray, The significance of the $\mathrm{Li_2MnO_3}$ component in 'composite' $x\mathrm{Li_2MnO_3}\cdot(1-x)\ \mathrm{LiMn_{0.5}Ni_{0.5}O_2}$ electrodes, Electrochemistry Communications 6(10) (2004) 1085-1091.

[35] L. Li, B. Song, Y. Chang, H. Xia, J. Yang, K. Lee, L. Lu, Retarded phase transition by fluorine doping in Li-rich layered $\mathrm{Li_{1.2}Mn_{0.54}Ni_{0.13}Co_{0.13}O_2}$cathode material, Journal of Power Sources 283 (2015) 162-170.

[36] W. Song, M.A. Pérez-Osorio, J.J. Marie, E. Liberti, X. Luo, C. O'Leary, R.A. House, P.G. Bruce, P.D. Nellist, Direct imaging of oxygen shifts associated with the oxygen redox of Li-rich layered oxides, Joule (2022).

[37] E.J Cheng, Y. Kushida, T. Kimura, H. Munakata, T. Abe, K. Kanamura, Degradation mechanism of all-solid-state Li metal batteries studied by electrochemical impedance spectroscopy, ACS Appl. Mater. Interfaces, 14 (2022) 40881-40889.

Chapter 7 Degradation mechanism of all-solid-state Li metal batteries studied by electrochemical impedance spectroscopy

7.1 Abstract

Solid-state Li-metal batteries have the potential to achieve both high safety and high energy densities. Among various solid-state fast-ion conductors, the garnet-type $Li_7La_3Zr_2O_{12}$ (LLZO) is one of the few that are stable to Li metal. However, the large interfacial resistance between LLZO and cathode materials severely limits the practical application of LLZO. Here a $LiCoO_2$ (LCO) film was deposited onto an Al-doped LLZO substrate at room temperature by aerosol deposition, and a low interfacial resistance was achieved. The LCO particles were pre-coated by Li_3BO_3 (LBO), which melted to join the LCO particles to the LLZO substrate at heating. All-solid-state Li/LLZO/LBO-LCO cells could deliver an initial discharge capacity of 128 mAh g^{-1} at 0.2 C and 60 °C and demonstrated relatively high-capacity retention of 87% after 30 cycles. The cell degradation mechanism was studied by electrochemical impedance spectroscopy (EIS) and was found to be mainly related to the increase of the interfacial resistance between LBO and LCO. In-situ SEM analysis verified the hypothesis that the increase of the interfacial resistance was caused primarily by interfacial cracking upon cycling. This study demonstrated the capability of EIS as a powerful non-destructive in-situ technique to investigate the failure mechanisms of all-solid-state batteries.

7.2 Introduction

Increasing concerns about environmental pollution accelerate the development of electric vehicles (EVs), which are quickly taking over the automobile industry despite the pandemic [1]. In 2020, the global transportation sector was responsible for 24% of direct CO_2 emissions from fuel combustion [2]. As a result, reducing transportation emissions is crucial in tackling climate

emergencies. Replacing gasoline cars with EVs is expected to be indispensable in reaching net-zero emissions worldwide.

However, the EV industry is concerned with maximizing the driving range and improving vehicle safety. Buyers are often deterred by range anxiety because public charging stations are lacking. In addition, Li-ion batteries with liquid electrolytes are potentially dangerous as the liquid electrolytes are usually highly flammable. Recently all-solid-state Li metal batteries have regained tremendous research interest because of the discovery of some new solid-state fast-ion conductors, such as LLZO and $Li_{10}GeP_2S_{12}$ (LGPS) [3]. For example, the room temperature ionic conductivity of cubic LLZO is about 10^{-3} S cm^{-1} [4]. Moreover, LLZO is chemically and electrochemically stable against Li metal [5] with a very high theoretical specific capacity of 3860 mAh g^{-1} and the lowest redox potential of -3.04 V *vs*. a standard hydrogen electrode.

Nevertheless, it is difficult to form good interfacial contact between LLZO and the electrode materials because LLZO has a high elastic modulus [6], resulting in high interfacial resistance and preventing the practical application of LLZO as a promising solid electrolyte [7]. Recently, a great effort has been made to decrease the interfacial resistance between LLZO and the Li metal anode [8-9]. For instance, the LLZO/Li interfacial resistance can be effectively reduced by introducing a thin Au or Al_2O_3 interlayer [10-11]. Good contact between LLZO and Li metal can also be achieved by high pressure and heating because Li metal is ductile and has a relatively low melting point of 180.5 °C [12]. In contrast, much less effort has been devoted to reducing the interfacial resistance between LLZO and the cathode materials [13]. Although good interfacial bonding between LLZO and LCO can be achieved by co-sintering [14], LCO decomposes at temperatures greater than 900 °C [15]. A convenient way to decrease the interfacial resistance is to introduce a small amount of liquid electrolyte to wet the cathode/solid electrolyte interface.

Moreover, developing an ionic liquid-containing LCO cathode is an effective way to reduce the cathode/solid electrolyte interfacial resistance [16-17]. Polymer-in-LLZO flexible sheet electrolytes were also proposed to increase the physical contact between solid electrolytes and cathodes [18-19]. However, introducing a liquid electrolyte or applying a polymer-based electrolyte to reduce the interfacial resistance will compromise battery safety. As a result, Han et al. suggested a new approach to lower the interfacial resistance between LLZO and LCO by thermally soldering LCO and LLZO together through an in-situ-formed ceramic interlayer [20]. Aerosol deposition (AD) is a room-temperature ceramic coating technology that deposits cathode films on ceramic solid electrolytes [21-22]. An illustration of the AD system in this study is shown in Figure 7.1a. Accelerated cathode particles are cracked and deformed after hitting the ceramic substrate (Figures 7.1b and c). The high surface energy generated by particle fracture or plastic deformation is likely to be the driving force for the densification of the fine particles at room temperature [23]. However, ceramic-based all-solid-state Li metal batteries prepared by AD usually degrade rapidly with cycling, which is very likely due to the mechanical degradation of the electrode-solid electrolyte interface [24]. Since the cathode particles are mechanically bound to the ceramic solid electrolyte, and both the cathode and electrolyte materials are brittle, the stress generated by the expansion and contraction of LCO during cycling can lead to the cracking of the electrode-solid electrolyte interface. Thus, the electrode-solid electrolyte interface prepared by AD requires further engineering, such as thermally soldering LCO and LLZO together with Li_3BO_3 (LBO), a mechanically soft solid electrolyte with a relatively low melting point of about 700 °C [25].

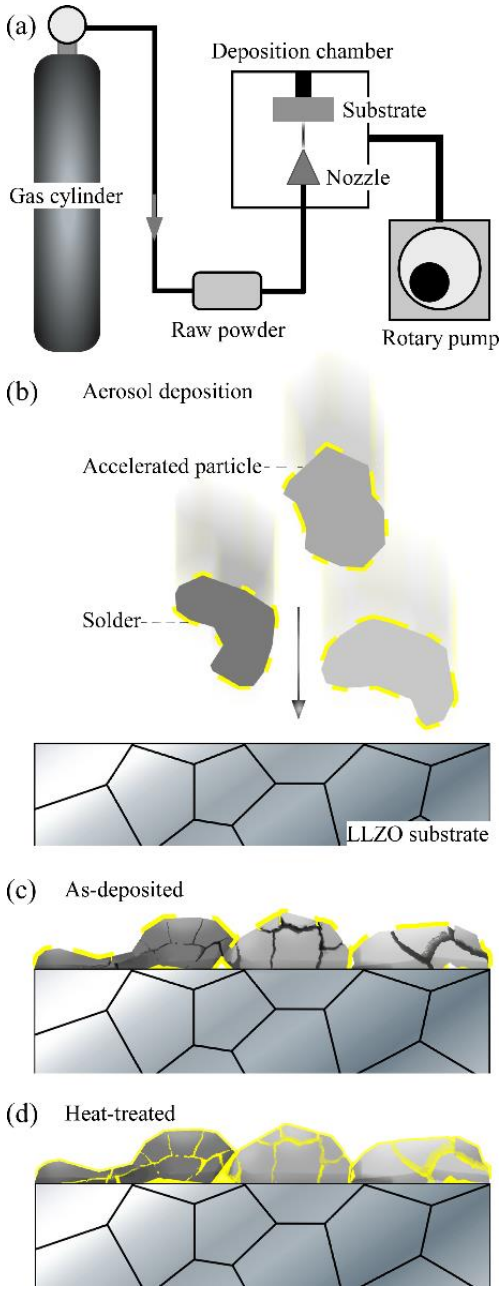

Figure 7.1 Illustration of the AD process. (a) The AD system, (b) Solder-coated cathode particles bombarding an LLZO substrate, (c) As-deposited cathode layer, where the particles are cracked and deformed, (d) Heat-treated cathode layer, where the void spaces are filled by the LBO solder after heating.

Here we deposited an LBO-LCO cathode film on an Al-doped LLZO substrate at room temperature by aerosol disposition (AD). Upon heating, the voids between the LCO particles and the voids between the LCO cathode layer and the LLZO substrate were filled by LBO, which was pre-coated on the LCO particles (Figure 7.1d). The all-solid-state Li/LLZO/LBO-LCO batteries showed relatively high-capacity retention above 87% after 30 cycles at 0.2 C and 60 °C, better than any previously reported results for aerosol-deposited all-solid-state Li metal batteries. We also attempted to study the cell degradation mechanism by EIS and found that the decrease in cell degradation was mainly related to the increase of the LBO/LCO interfacial resistance, which was most likely caused by electromechanical cracking of the interface during cycling.

7.3 Experiment

7.3.1 Synthesis of $LiCoO_2$ (LCO)

The LCO powder was synthesized through a sol-gel method using lithium acetate ($C_2H_3LiO_2$, 98.0%, FUJIFILM Wako Pure Chemical Corporation, Japan) and cobalt acetate tetrahydrate ($C_4H_6CoO_4$-$4H_2O$, 99.0%, FUJIFILM Wako Pure Chemical Corporation, Japan) as starting materials. The starting materials were dissolved in water to form a solution in which citric acid ($C_6H_8O_7$, 99.0%, Kanto Chemical Co., Inc., Japan) was added as a chelating agent for gelation. The solution was stirred at 80 °C for 1 h and dried to a solid mixture at 120 °C. The obtained solid mixture was calcined at 400 °C for 9 h in air, followed by sintering at 800 °C for 8 h in air to produce a crystalline LCO powder. The XRD pattern of the synthesized LCO powder is shown in Figure 7S1.

7.3.2 Synthesis of Li_3BO_3 (LBO)

The LBO powder was synthesized by heating mixtures of Li_2CO_3 (99.0%, FUJIFILM Wako Pure Chemical Corporation, Japan) and B_2O_3 (95%, Kanto Chemical Co., Inc., Japan) in a molar ratio of 3:1 at 600 °C for 10 h in air. The LBO powder was further pulverized (to reduce the average particle size to less than 1μm) by ball milling (400 rpm, 10 min milling followed by a 20 min pause to avoid overheating, repeated 99 times). Figure 7S2 shows the XRD pattern of the synthesized LBO powder.

7.3.3 Synthesis of Al-LLZO

The Al-doped LLZO powder was prepared by a solid-state reaction method. Starting materials of $LiOH{\cdot}H_2O$, $La(OH)_3$, and ZrO_2 powders were mixed by ball-milling and calcined at 900 °C for 15 h. After mixing with a γ-Al_2O_3 powder, the calcined powder was compacted and sintered at 900 °C for 3 h and then at 1200 °C for 24 h. The molar ratio of $LiOH{\cdot}H_2O$, $La(OH)_3$, ZrO_2, and γ-Al_2O_3 was 6.9: 3.0 : 2.0: 0.125. The XRD pattern of the synthesized Al-doped LLZO pellet shows a cubic structure (Figure 7S3). An optical image of the Al-doped LLZO pellet is shown in Figure 7S4a, and an SEM image of a fracture surface is shown in Figure 7S4b. The relative density of the LLZO pellet was about 95%, determined by measuring its weight and dimensions.

7.3.4 Aerosol Deposition

A mixture of the LBO and LCO powders in a mass ratio of 3:7 was ball-milled at 400 rpm for 30 min, following calcination at 800 °C for 2 h in air. The LBO-coated LCO was transferred into the deposition chamber, which was evacuated by a rotary pump to 80 Pa. The diameter of the nozzle hole was 1 mm, and the deposition area on the LLZO substrate was 0.785 cm^2. The distance between the LLZO substrate and the nozzle was 40 mm. The Ar gas pressure was set to 0.6 MPa.

The optimal particle size for AD was found to be about 0.1 to 10 μm. The amount of LBO-LCO deposited on the LLZO substrate was determined from the weight increase of the LLZO substrate after aerosol deposition. The LLZO substrate coated with the LBO-LCO composite cathode layer was further heated at 750 °C for 2 h in air to increase the interfacial contact between the LBO-LCO cathode and the LLZO substrate.

7.3.4 Materials characterization

The crystal structure was analyzed by X-ray diffraction (XRD, Rigaku SmartLab). The microstructure was analyzed by a scanning electron microscope (SEM, JSM-6490A). The element distribution at the LBO-LCO/LLZO interface was investigated by energy-dispersive X-ray spectroscopy (EDS). An in-situ electrochemical cell was designed for continuously monitoring the microstructure evolution of the cross-section of the LBO-LCO/LLZO interface region during cycling.

7.3.5 Electrochemical measurements

AC electrochemical impedance spectroscopy (EIS) was performed in the frequency range from 7 MHz to 0.1 Hz at 25-60 °C (Biologic SP-300, France). The amplitude of the perturbation was 10-50 mV. The EIS spectrum of the Al-doped LLZO pellet is shown in Figure 7S5a, and the Arrhenius plot is shown in Figure 7S5b. Galvanostatic cycling of the all-solid-state Li/Al-doped LLZO/LBO-LCO cells was carried out at 0.2 C and 60 °C with a cut-off voltage range of 2.8 to 4.3 V. The configuration of the all-solid-state cell is illustrated in Figure 7S6a. A UFO-shaped battery testing apparatus was designed and built for the cycling test, as shown in Figure 7S6b. The EIS data were fitted to equivalent electrical circuit models with the EC-Lab software.

7.4 Results and discussions

7.4.1 SEM micrograph of the LLZO/LBO-LCO interface area

An SEM image of the pristine LCO powder synthesized by a sol-gel method is shown in Figure 7.2a. The particle size is in the range of 0.5-3.0 μm, and the surface is clean. The LCO powder has a trigonal structure with $R\bar{3}m$ symmetry, as confirmed by X-ray diffraction (Figure 7S1). On the other hand, the LBO powder synthesized by a solid-state reaction shows a monoclinic structure with $P2_1/c$ symmetry (Figure 7S2). The LCO particle was coated by LBO (Figures 7.2b and c) through ball milling and heat treatment (800 °C). The mass ratio between LCO and LBO in the composite LCO-LBO cathode material is 7:3. It should be noted that LBO became amorphous-like after ball milling (Figures 7.2c and 7S7).

The LBO-LCO powder was deposited onto a cubic LLZO (Figure 7.S3) substrate by AD at room temperature. The interfacial contact between LBO-LCO and LLZO was further improved following heat treatment at 750 °C for 1 h (Figure 7.2d). The cubic LLZO with a relative density of about 95% was prepared by a solid-state reaction and pressureless sintering in air (Figure 7S4). The thickness of the deposited composite cathode layer is generally in the range of 4 to 8 μm, while it is also possible to deposit much thicker cathode films (e.g., a 25 μm-thick film, Figure 7S8) on LLZO by AD. Figures 2e and f show the energy-dispersive X-ray spectroscopy (EDS) mappings of oxygen and cobalt at the LBO-LCO|LLZO interface region, indicating good interfacial contact was achieved.

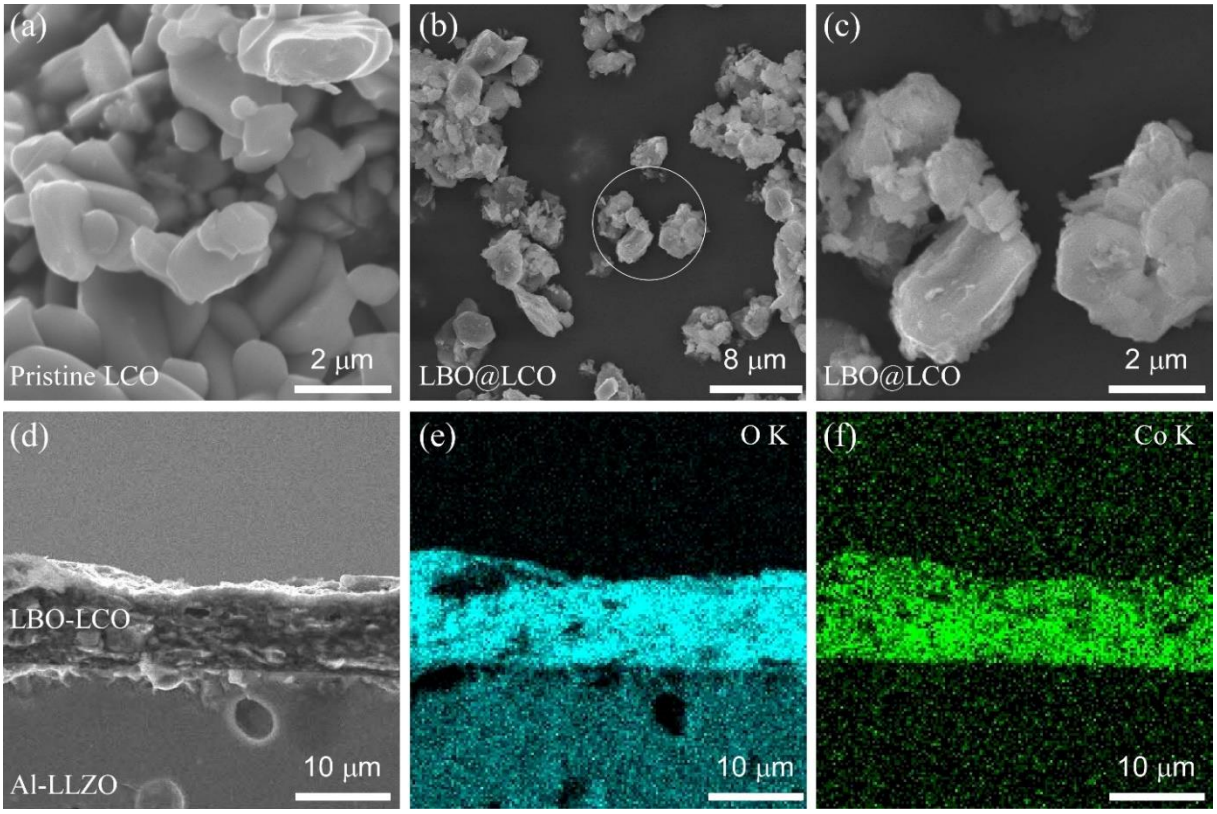

Figure 7.2 SEM micrographs of the LBO-LCO/LLZO interface. (a) As-synthesized LCO powder, (b) LBO-coated LCO powder, (c) High-resolution SEM image of the circled area in (b), (d) LBO-LCO cathode layer deposited on LLZO by AD at room temperature, following heat treatment at 750 °C for 1 h, (e) Element mapping of oxygen at the LBO-LCO/LLZO interface area, (f) Element mapping of cobalt at the LBO-LCO/LLZO interface area

7.4.2 Galvanostatic cycling profiles of the Li/LLZO/LBO-LCO cell

Figure 7.3 shows the galvanostatic cycling profiles of the Li/LLZO/LBO-LCO cells at 0.2 C and 60 °C. The cut-off voltage range was 2.8 to 4.3 V. As shown in Figure 7.3a, the ceramic-based all-solid-state cell delivered a high initial discharge capacity of 123 mAh g^{-1}. The LBO-LCO cathode layer was relatively thin (5.6 μm in thickness), and the corresponding loading of the LCO active material was about 1.1 mg cm^{-2}. The all-solid-state Li metal cell showed relatively high-

capacity retention of above 84% after 30 cycles (Figure 7.3b), better than any previously reported results for aerosol-deposited all-solid-state Li metal batteries with a ceramic electrolyte [21, 24, 26]. The cell performance was further improved when the thickness of the LBO-LCO cathode layer was decreased from 5.6 to 4.3 μm because of reduced overall cell resistance. The initial discharge capacity increased to 128 mAh g^{-1} (Figure 7.3c), and the capacity retention after 30 cycles increased to 87% (Figure 7.3d). The voltage profile of the all-solid-state cell at different current densities is shown in Figure 3e. The cell cycling performance was sensitive to current density, and well-defined plateaus were only observed at current densities less than 0.5 C. The discharge capacities were 126.3, 114.2, 95.1, 73.8, and 51.6 mA h g^{-1} when the current densities were 0.1 C, 0.2 C, 0.5 C, 1 C, and 2 C, respectively. However, the discharge capacity recovered promptly to 110.1mAh g^{-1} when the C rate returned to 0.1 C, indicating a relatively high cycling capability at various C rates. It is worth mentioning that the Li/LLZO/LBO-LCO cell cannot be reversibly cycled without LBO. The LBO coating was critical for the functioning of the all-solid-state cell.

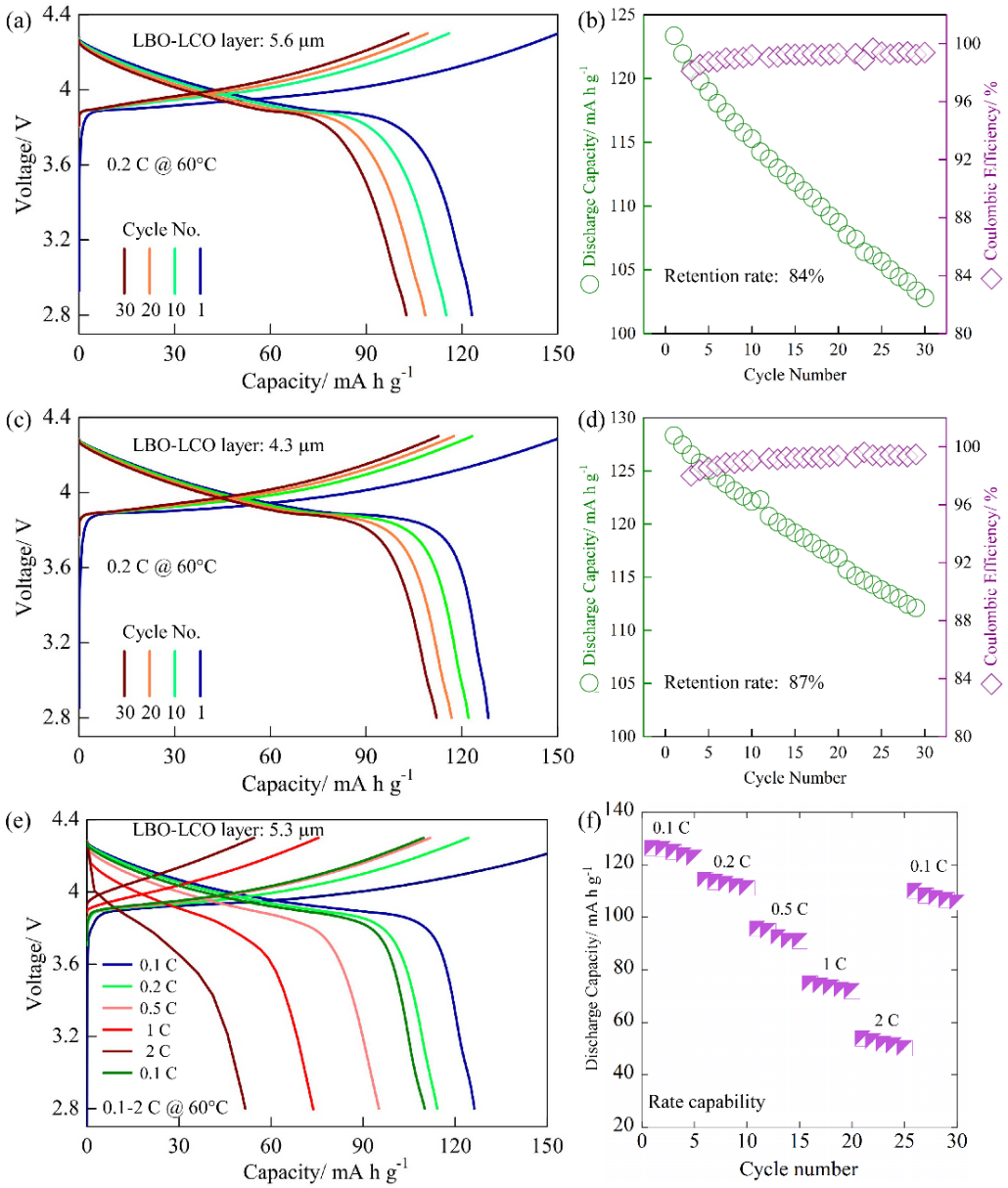

Figure 7.3 Galvanostatic cycling performance and rate capability of the Li/LLZO/LBO-LCO cell at 60 °C. (a) and (b) Cycling performance. The LBO-LCO cathode layer is 5.6 μm thick, and the LCO active material loading is 1.1 mg cm^{-2}, (c) and (d) Cycling performance. The LBO-LCO cathode layer is 4.3 μm thick, and the LCO active material loading is 0.84 mg cm^{-2}, (e) and (f) Rate capability. The LBO-LCO cathode layer is 4.3 μm thick, and the LCO active material loading is 1.0 mg cm^{-2}.

7.4.3 EIS analysis of the Li/LLZO/LBO-LCO cell

To understand the degradation mechanism of the all-solid-state Li/LLZO/LBO-LCO cell, EIS was performed at 10% state-of-charge (SOC) in the frequency range from 3 MHz to 0.1 Hz at 60 °C (Figure 7.4). The amplitude of the perturbation was 50 mV. The physical configuration of the all-solid-state Li/LLZO/LBO-LCO battery is illustrated in Figure 7.4a, where the Au interlayer is introduced to improve the interfacial contact between the battery components.

EIS is an electrochemical technique to measure a system's static or dynamic impedance by monitoring the current response as a function of the applied AC potential [27-28]. Regardless of galvanostatic or potentiostatic conditions, the *ac* signal is sinusoidal. The impedance Z (ω) is a frequency-dependent complex number [29-30]:

$$Z(\omega) = \frac{V}{I} = \frac{V_m}{I_m} e^{j\emptyset} = \frac{V_m}{I_m}[\cos(\emptyset) + jsin(\emptyset)] = Z_0 \cos(\emptyset) + jZ_0 \sin(\emptyset) \quad (7.1)$$

$$V = V_m \sin(\omega t) \quad (7.2)$$

$$I = I_m \sin(\omega t - \emptyset) \quad (7.3)$$

where j=$\sqrt{-1}$ is the imaginary unit, ω=$2\pi f$ is the angular frequency of the applied AC voltage, f *is* the AC frequency, V_m is the maximum value of V, and I_m is the maximum value of I. Typical impedance spectra consist of both resistive (R) and capacitive (C) components, and the resistance consists of both electronic and ionic resistance. The impedance data is commonly plotted in two ways: (i) a Nyquist plot that shows the resistance along the real or *x*-axis and negative reactance (such as capacitance) along the imaginary or *y*-axis; (ii) a Bode plot that shows the logarithm of the frequency along the *x*-axis, and the logarithm of the impedance Z along one *y*-axis and the phase shift along the second *y*-axis. The Nyquist plot is very sensitive to changes and useful for analyzing the possible reaction mechanisms in the electrochemical system. In contrast, the Bode

plot is advantageous for observing phase margins when the system becomes unstable because all information can be visible [29].

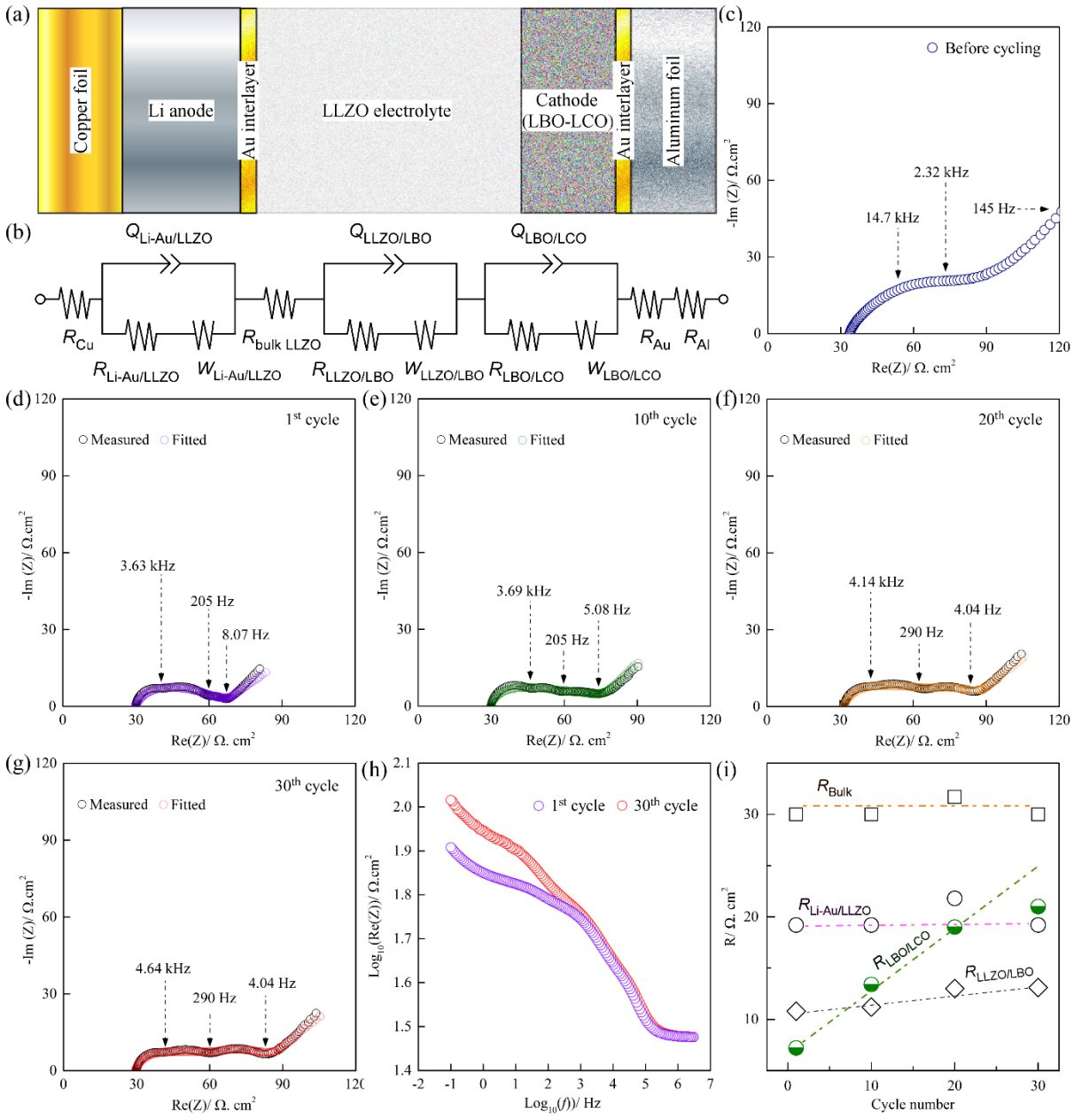

Figure 7.4 EIS analysis of the degradation mechanism of the Li/LLZO/LBO-LCO cell. (a) Illustration of the all-solid-state cell configuration, (b) An ideal equivalent electrical circuit of the cell, (c) EIS spectrum of the cell before cycling, (d-g) EIS spectra at 10 % of SOC during the 1st, 10th, 20th, and 30th charging processes, respectively, (h) Logarithm of the total impedance vs. the

logarithm of the frequency (the Bode plot is shown in Figure 7S9), (i) Evolution of the resistance components with cycling. In particular, the interfacial resistance between LBO and LCO ($R_{LBO/LCO}$) increased significantly with cycling.

An ideal equivalent electrical circuit of the Li/LLZO/LBO-LCO cell is shown in Figure 7.4b. Since the resistance of the current collectors, the Au interlayers, and the LLZO electrolyte bulk are free of correlation with capacitance or inductance, they can be combined into an overall bulk resistance of R_{bulk}. In addition, only one inclined tail about 45° to the x-axis at the low-frequency region represents a Warburg element, which describes a diffusion-controlled process. Similarly, all the Warburg resistances can be combined into an overall Warburg resistance of $W_{warburg}$ to minimize the equivalent circuit elements for practical impedance analysis. A simplified equivalent circuit is shown in Figure 7.5a. The Nyquist plot before cycling is shown in Figure 7.4c, which shows only a high-frequency distorted semicircle and a low-frequency tail characteristic. The total resistance of the cell was about 115 Ω, corresponding to an area-specific resistance (ASR) of 90 Ω.cm^2. After charging, the ASR decreased significantly to 65 Ω.cm^2 because of the reduced overall charge transfer resistance R_{ct} (Figure 7.4d). Thus, the interfacial contact between LBO-LCO and LLZO was improved after the initial charging process. In addition, three poorly resolved arcs are observed in the frequency domain from 3 MHz to 8 Hz, which can be assigned to the interfacial resistance between Li-Au and LLZO ($R_{Li\text{-}Au/LLZO}$), that between LLZO and LBO ($R_{LLZO/LBO}$) and that between LBO and LCO ($R_{LBO/LCO}$), respectively. This is because cubic LLZO has much higher ionic conductivity (about 10^{-4} S cm^{-1} @25 ℃) than LBO (about 10^{-6} S cm^{-1} @ 25 ℃). As a result, Li-ions are supposed to transport much faster through the Li-Au/LLZO interface than through the LBO/LCO interface. The arc at the high-frequency region, which corresponds to a simplified *RC* Randles equivalent circuit (a resistor and a capacitor in parallel), is the response of the Li-

Au/LLZO interface. On the other hand, the arc at the low-frequency region is the response of the LBO/LCO interface. The simulated spectrum based on the simplified equivalent electrical circuit (Figure 7.5a) agrees well with the measured spectrum. Similarly, the EIS spectra after 10 cycles, 20 cycles, and 30 cycles (as well as the corresponding simulated spectra) are shown in Figures 4e, f, and g, respectively. The overall ASR of the cell increased rapidly with cycling, which is also reflected in Figure 7.4h. In particular, the $R_{LBO/LCO}$ increased significantly with cycling, while the R_{bulk} and $R_{Li\text{-}Au/LLZO}$ (Figure 7S10) were almost unchanged after 30 cycles (Figure 7.4i). Besides, the $R_{LLZO/LBO}$ increased gradually with cycling. The increase of $R_{LBO/LCO}$ is very likely related to the electromechanical degradation of the LBO/LCO interface caused by the insertion and extraction of Li-ions into and from LCO:

$$LiCoO_2 \leftrightarrows CoO_2 + Li^+ + e^- \qquad (7.4)$$

Similarly, the increase of $R_{LLZO/LBO}$ is likely caused by electromechanical degradation of the LLZO/LBO interface. All the impedance parameters used for the equivalent electrical circuit modeling are listed in Table 7.1.

Table 7.1 Impedance parameters obtained by using the impedance fitting tool of ZFit available in EC-Lab. The value of the χ^2 distribution for the fitting is in the range of 0.9 to 3.0.

Element / Cycle	R_{bulk} ($\Omega.cm^2$)	$R_{Li\text{-}Au/LLZO}$ ($\Omega.cm^2$)	$R_{LLZO/LBO}$ ($\Omega.cm^2$)	$R_{LBO/LCO}$ ($\Omega.cm^2$)	$Q_{Li\text{-}Au/LLZO}$ ($F.s^{(n-1)}$)	$Q_{LLZO/LBO}$ ($F.s^{(n-1)}$)	$Q_{LBO/LCO}$ ($F.s^{(n-1)}$)	W_{warbug} ($\Omega.s^{-0.5}$)
1st	30.0	19.2	10.8	7.2	4E-06 n=0.7856	4E-05 n=0.8302	9E-04 n=0.8142	14.34
10th	30.0	19.2	11.2	13.4	3E-06 n=0.7911	4E-05 n=0.8219	8E-04 n=0.7494	17.08
20th	31.7	21.8	13.0	19.0	1E-03 n=0.6144	5E-05 n=0.7587	2E-06 n=0.8021	19.41
30th	30.0	19.2	13.1	21.0	1E-03 n=0.6692	2E-06 n=0.8611	1E-04 n=0.6160	21.27

Note: Q stands for constant phase element or CPE, used for modeling the behavior of a double layer that is an imperfect capacitor. For practical impedance analysis, R_{Cu}, $R_{bulk\ LLZO}$, $R_{Au,}$ and R_{Al} are combined into R_{bulk}. The Warburg resistances of $W_{Li\text{-}Au/LLZO}$, $W_{LLZO/LBO}$, and $W_{LBO/LCO}$ are combined into $W_{warburg}$, as shown in Figure 7.5a.

In-situ SEM was performed to verify the crack evolution mechanism discussed above. Simulation results based on the simplified electrical circuit shown in Figure 7.5a suggested that the interfacial cracking between LBO and LCO was the primary degradation mechanism of the Li/LLZO/LBO-LCO cell with cycling. The pre-existing cracks (Figure 7.5b) become larger and deeper after the initial charging (Figure 7.5c) and discharging (Figure 7.5d), as indicated by the arrowheads in Figures 7.5b-d. In addition, as expected, crack growth is more likely to occur at higher charging voltages. The crack in Figure 7.5e becomes slightly larger as the voltage increases from 3.5 to 4.2 V (Figures 7.5e-g).

On the other hand, no visible cracking was observed between the LBO/LLZO interface, probably because the degree of the interfacial cracking was less severe. Another possibility accounting for the increase of $R_{LLZO/LBO}$ might be due to the potential reaction between LBO and LLZO. Thus, identifying a more suitable solder material than LBO is critical for developing all-solid-state Li/LLZO/LCO batteries.

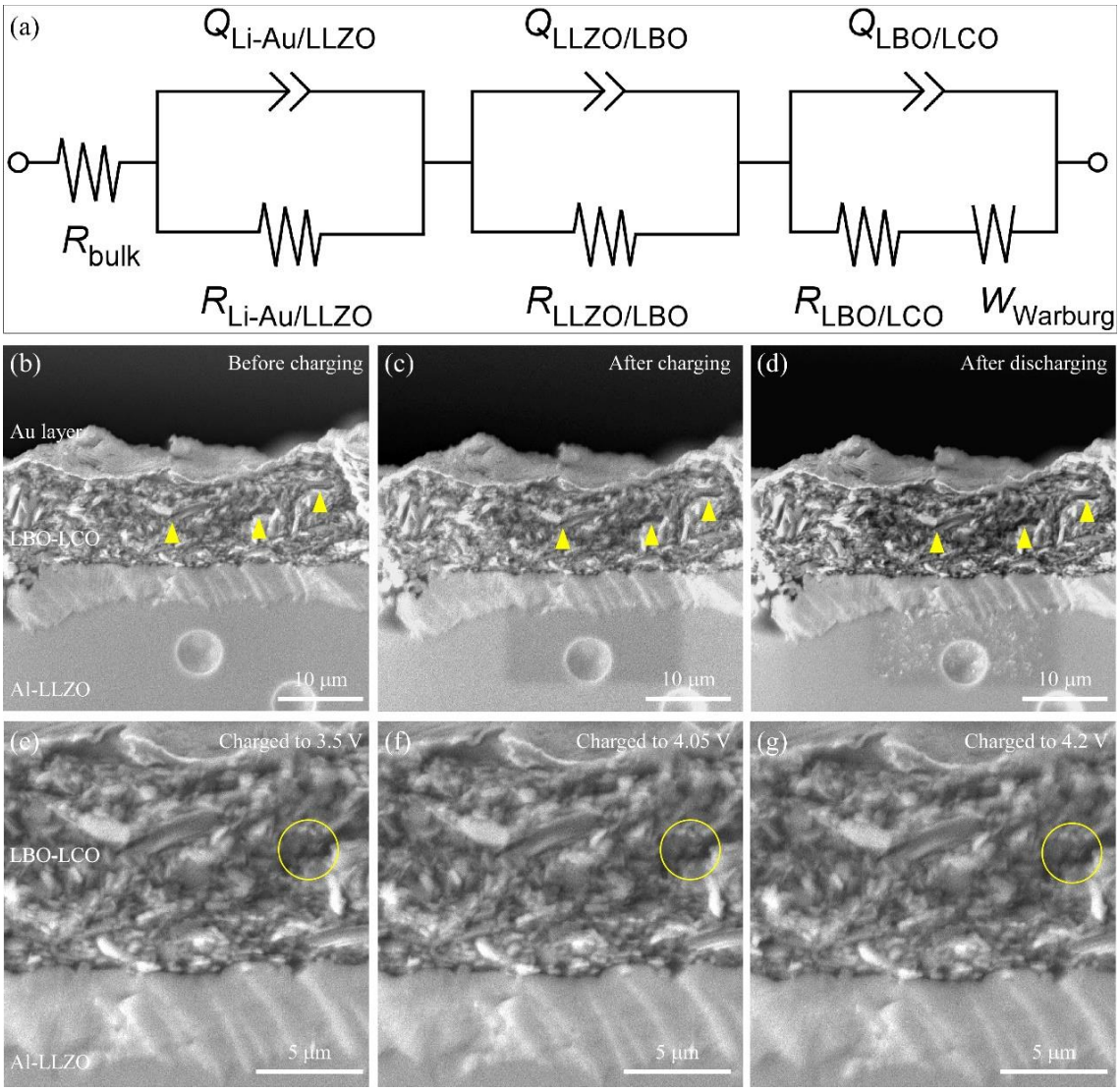

Figure 7.5 In-situ SEM analysis of the degradation mechanism of the Li/LBO-LCO/LLZO cell. (a) A simplified equivalent electrical circuit of the one shown in Figure 7.4b, (b), (c), and (d) Cross-sectional SEM images showing the crack evolution in the LBO-LCO/LLZO interface region before charging, after charging to 4. 2V and after discharging to 2.8 V, respectively, (e), (f), and (g) Cross-sectional SEM images showing the crack evolution in the LBO-LCO/LLZO interface region after charging to 3.5 V, 4.05 V, and 4.2 V, respectively.

7.5 Conclusions

All-solid-state Li/LLZO/LBO-LCO cells were prepared by aerosol deposition, and the cell degradation mechanism was investigated by electrochemical impedance spectroscopy. LBO-LCO cathode films were deposited onto an Al-doped LLZO ceramic substrate at room temperature. LCO, the active material, was 70 wt% in the LBO-LCO cathode layer, while LBO functioned as a Li^+-conducting solder that joined the LCO particles to the LLZO substrate at heating. The LBO coating was critical for the functioning of the all-solid-state Li/LLZO/LBO-LCO cell. The all-solid-state Li/LLZO/LBO-LCO cell delivered a high initial discharge capacity of 128 mAh g^{-1} at 0.2 C and 60 °C. Moreover, it demonstrated high-capacity retention of 87% after 30 cycles, possibly representing the best available results for all-solid-state Li metal batteries with ceramic oxide electrolytes.

Based on the EIS analysis results, the cell degradation was mainly due to the increased LBO/LCO interfacial resistance. In-situ SEM analysis further confirmed the hypothesis that the interfacial cracking of the LBO/LCO interface was the main reason for the cell degradation upon cycling. Electrochemical impedance spectroscopy has been demonstrated here to be a powerful non-destructive in-situ technique that can monitor a battery's impedance evolution at different stages and provide insights into the cell failure mechanism.

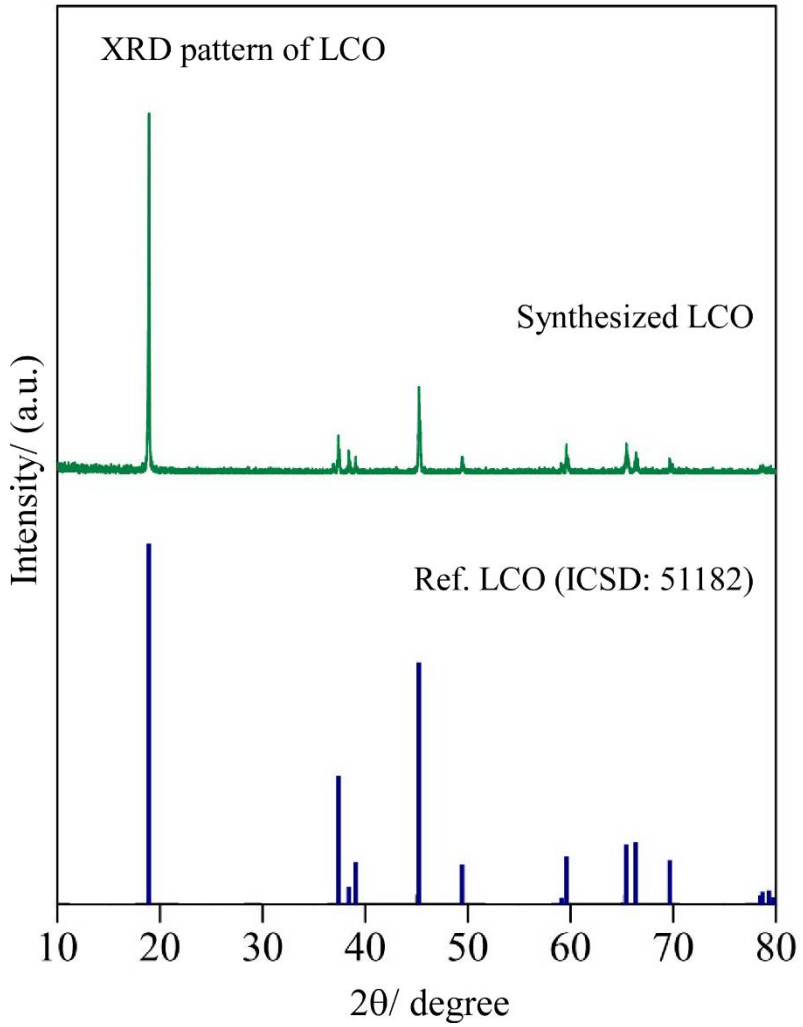

Figure 7 S1 XRD pattern of the synthesized $LiCoO_2$ (LCO) powder, which has a trigonal crystalline structure with $R\bar{3}m$ symmetry. The particle size is about 0.5-3.0 μm.

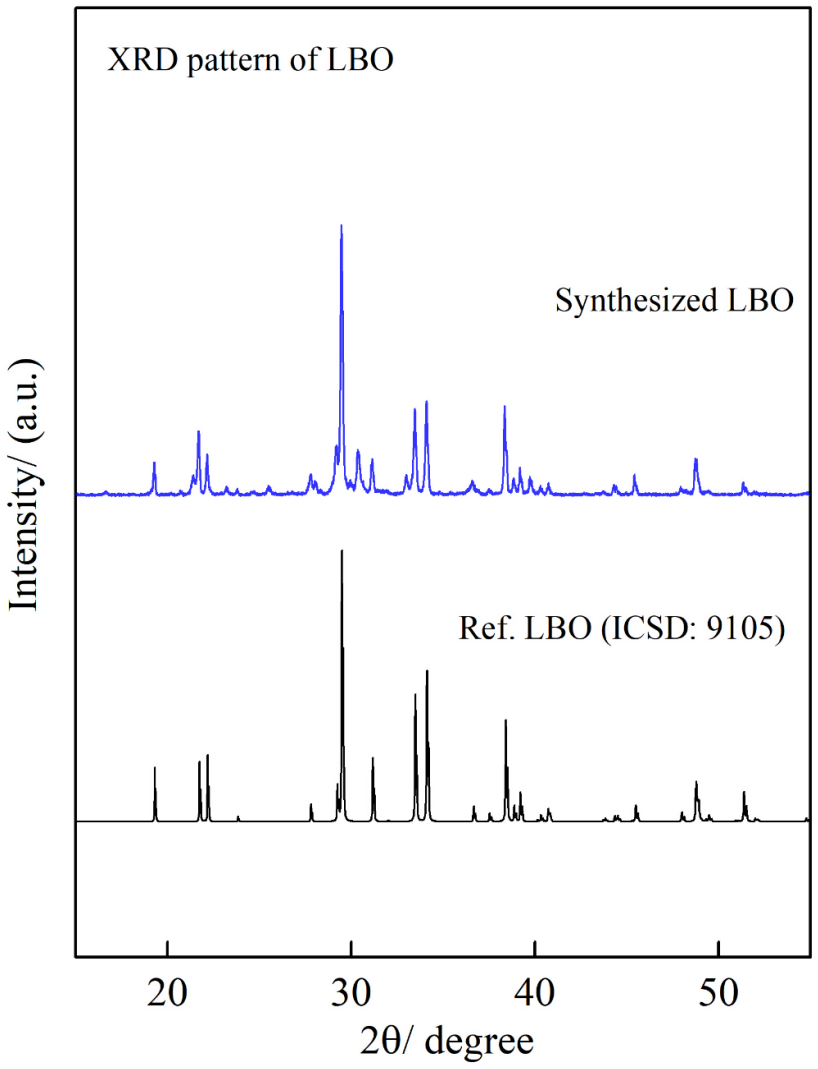

Figure 7 S2 XRD pattern of the synthesized Li_3BO_3 (LBO) powder, which has a monoclinic crystalline structure with $P2_1/c$ symmetry. The average particle size is less than 1.0 μm.

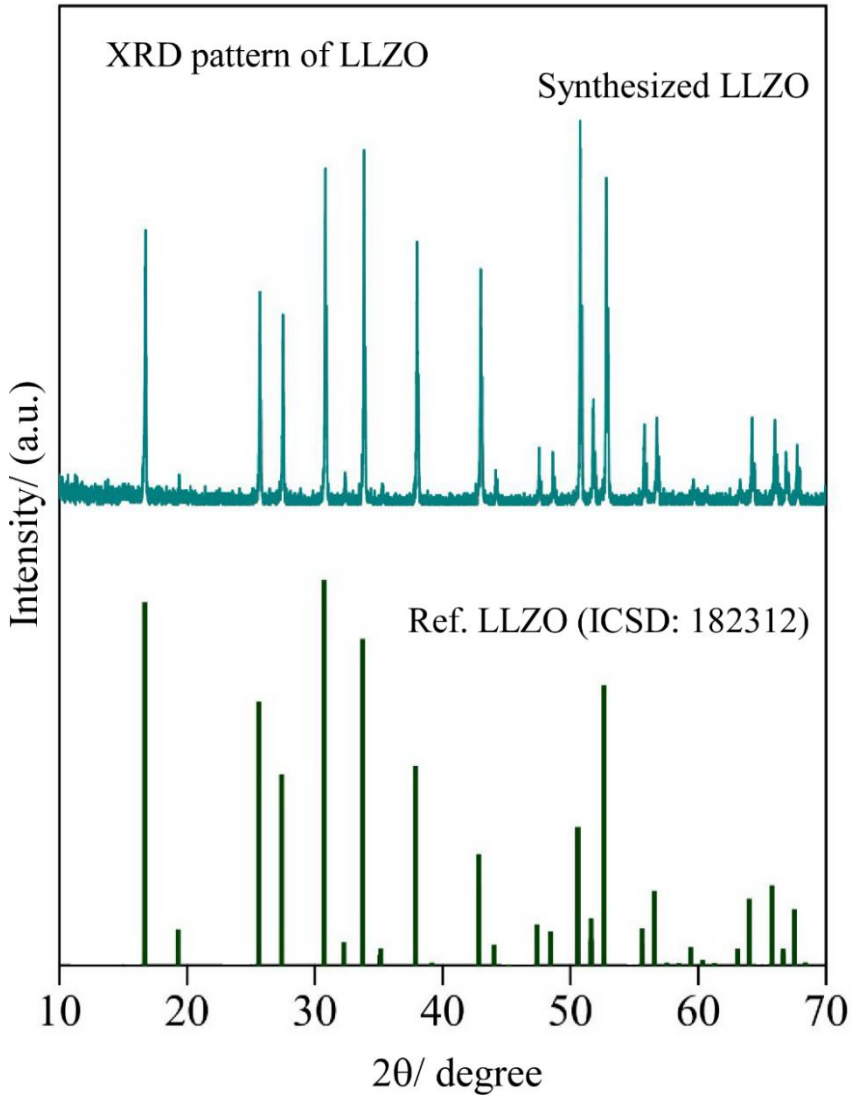

Figure 7 S3 XRD pattern of the sintered Al-doped $Li_7La_3Zr_2O_{12}$ (LLZO) pellet, which has a cubic crystalline structure with $Ia\bar{3}d$ symmetry.

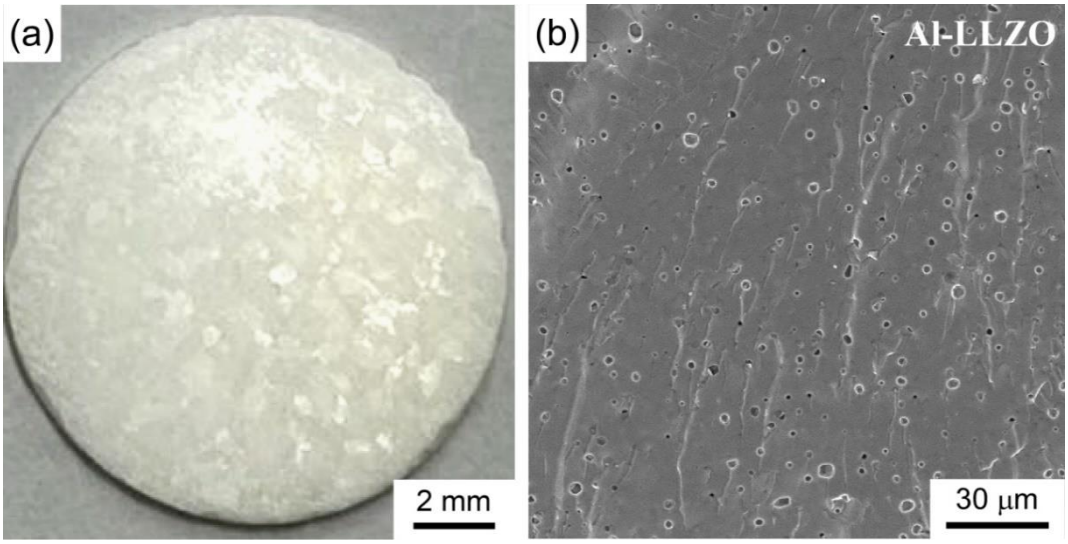

Figure 7 S4 Optical and SEM images of the high-temperature sintered Al-doped LLZO pellet. (a) An optical image, (b) An SEM cross-sectional image. The relative density of the pellet is estimated to be about 95%.

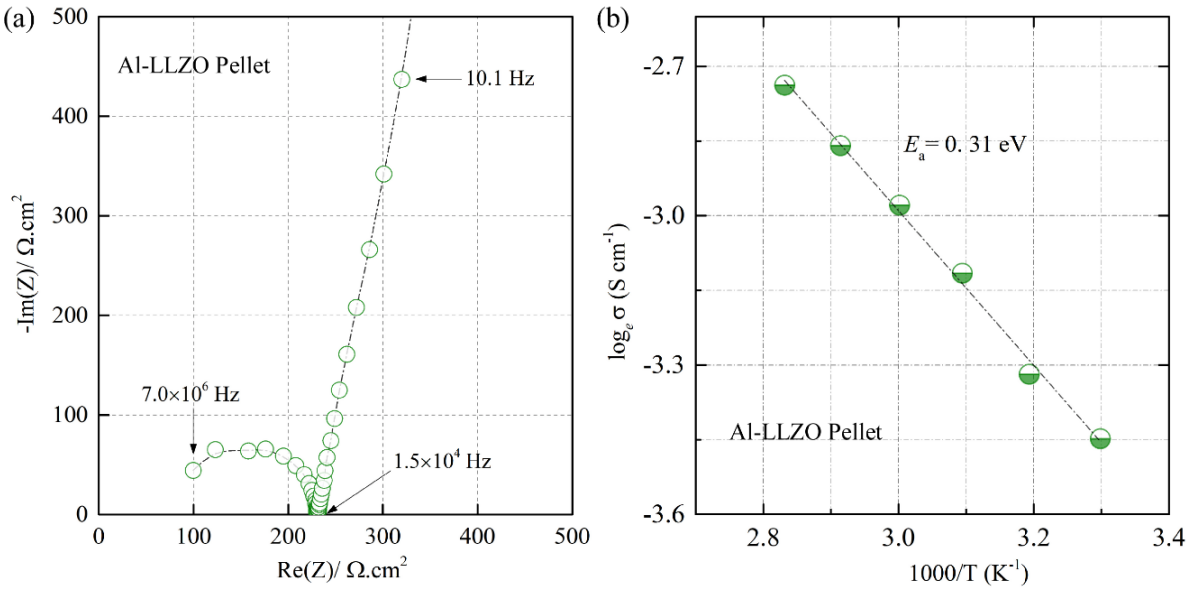

Figure 7 S5 EIS and Arrhenius spectra of the Al-doped LLZO pellet. (a) EIS spectrum of the synthesized Al-doped LLZO pellet at 25-30°C from 3 MHz to 0.1 Hz. The pellets' thickness was 400-500 μm, and the ionic conductivity was about 3.6×10^{-4} S cm^{-1} at 30 °C, (b) Arrhenius conductivity of the Al-doped LLZO pellet.

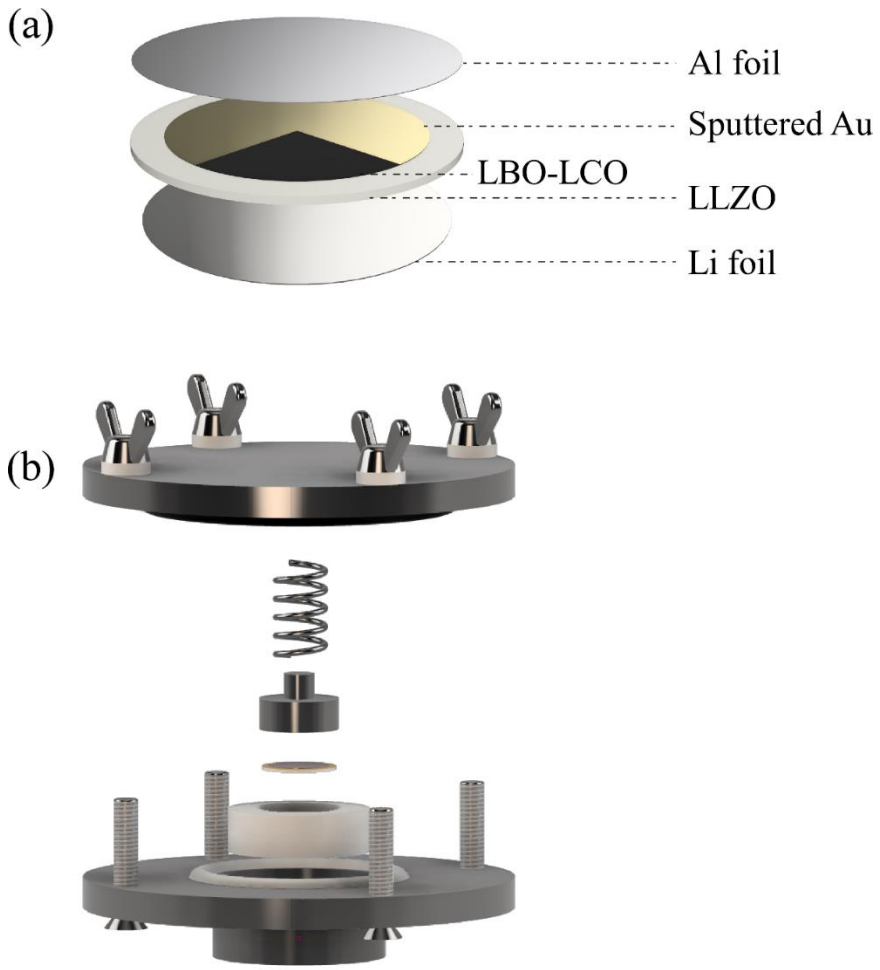

Figure 7 S6 Cell configuration. (a) Configuration of the LBO-LCO/Al-doped LLZO/Li cell, (b) A UFO-shaped battery apparatus designed and built for the cycling test.

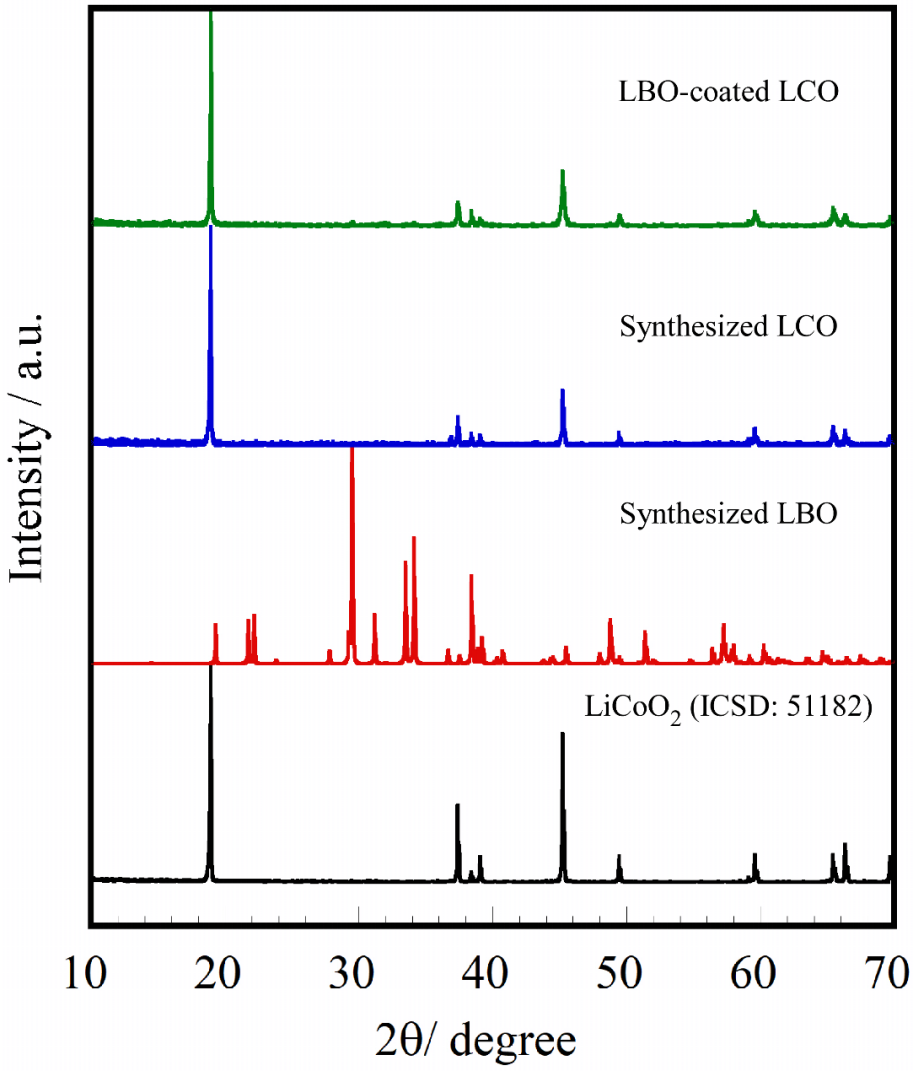

Figure 7 S7 XRD pattern of the LBO-coated LCO, in which the LBO has been ball milled. The degree of crystallinity of the synthesized LBO is significantly reduced after ball milling.

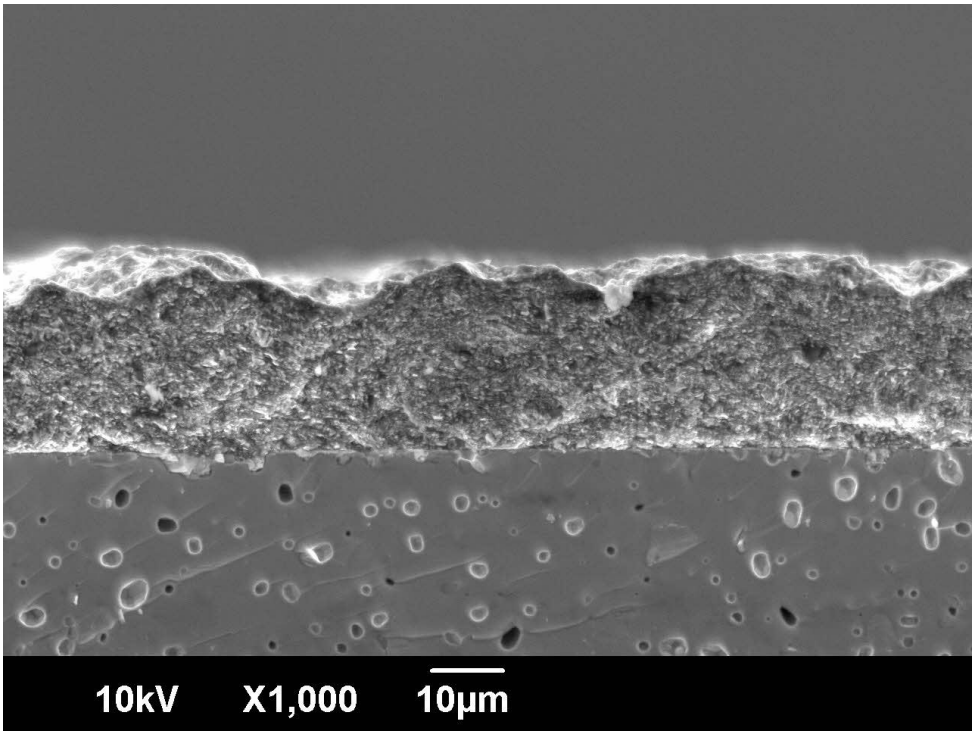

Figure 7 S8 A cross-sectional SEM image of a 25 μm-thick LBO-LCO film deposited on Al-doped LLZO by aerosol deposition at room temperature.

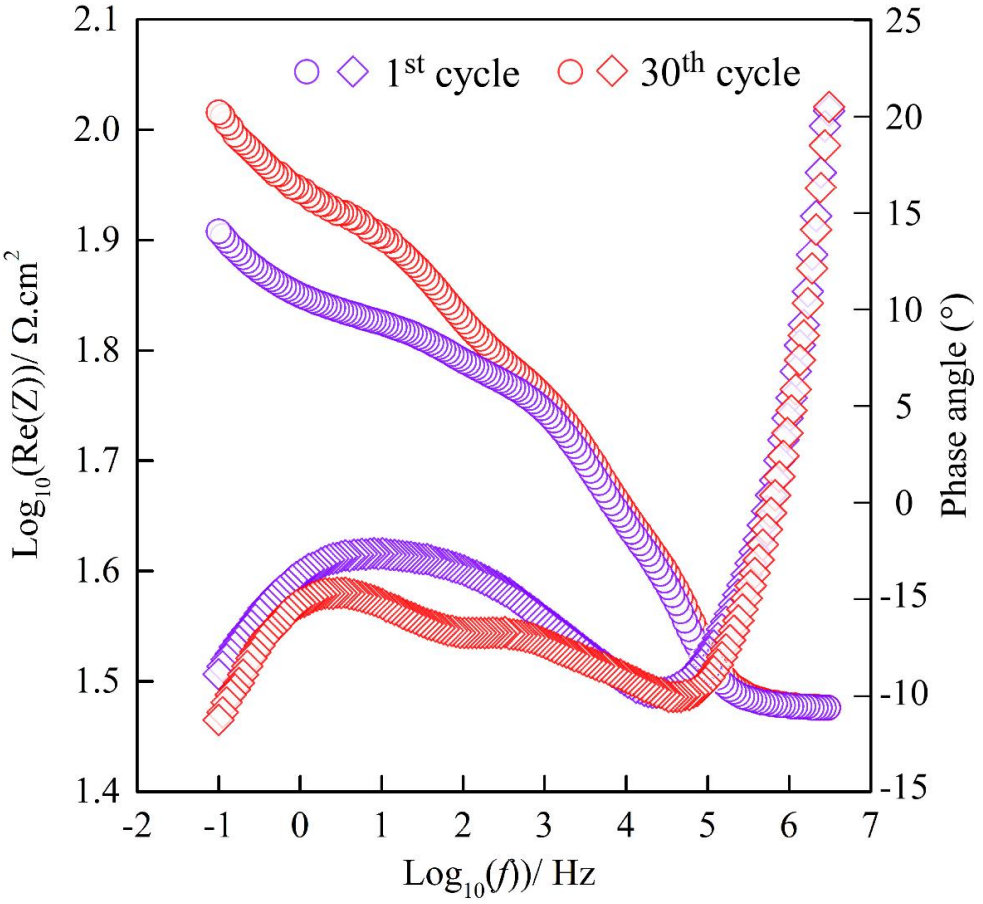

Figure 7 S9 Bode plots of the Li/Al-LLZO/LBO-LCO cell at 10% SOC during the first and 30th charging processes.

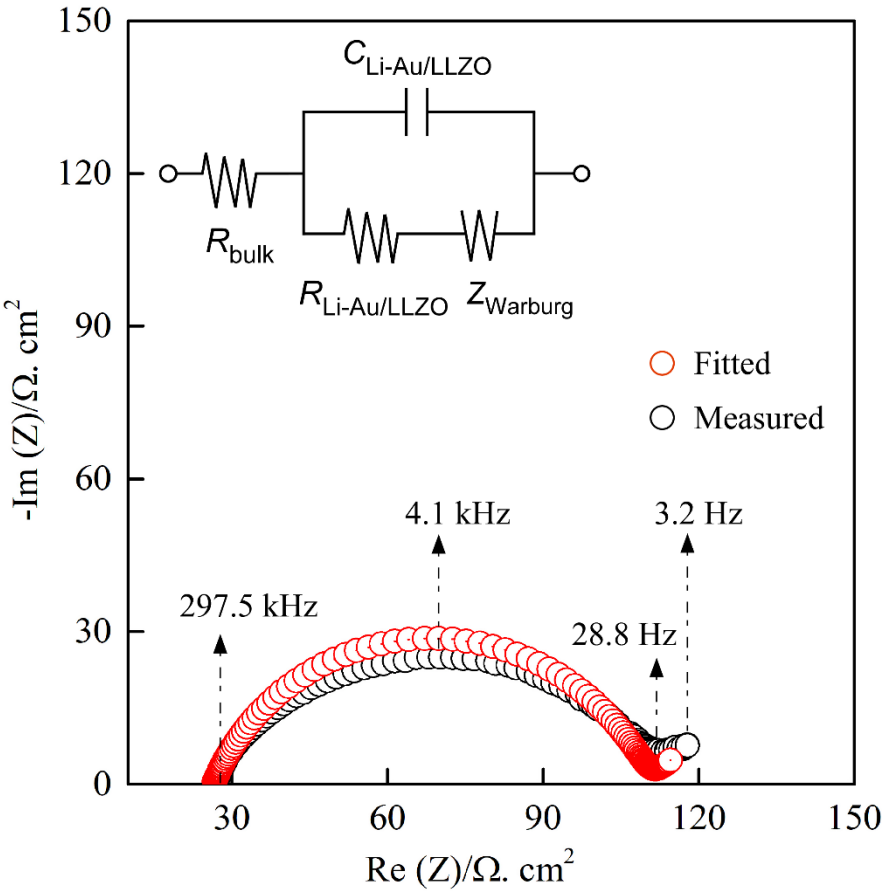

Figure 7 S10 EIS spectrum and the simulated spectrum of the Li-Au/Al-doped LLZO/Au-Li symmetric cell. The insect is the corresponding equivalent electrical circuit.

Reference

[1] Global EV Outlook 2021, IEA, Paris, 2021. https://www.iea.org/reports/global-ev-outlook-2021.

[2] Tracking Transport 2020, IEA, Paris, 2020. https://www.iea.org/reports/tracking-transport-2020.

[3] N. Kamaya, K. Homma, Y. Yamakawa, M. Hirayama, R. Kanno, M. Yonemura, T. Kamiyama, Y. Kato, S. Hama, K. Kawamoto, A lithium superionic conductor, Nature Materials 10(9) (2011) 682-686.

[4] K. Subramanian, G.V. Alexander, K. Karthik, S. Patra, M. Indu, O. Sreejith, R. Viswanathan, J. Narayanasamy, R. Murugan, A brief review of recent advances in garnet structured solid electrolyte based lithium metal batteries, Journal of Energy Storage 33 (2021) 102157.

[5] R. Murugan, V. Thangadurai, W. Weppner, Fast Lithium Ion Conduction in Garnet-Type $Li_7La_3Zr_2O_{12}$, Angewandte Chemie International Edition 46(41) (2007) 7778-7781.

[6] S. Yu, R.D. Schmidt, R. Garcia-Mendez, E. Herbert, N.J. Dudney, J.B. Wolfenstine, J. Sakamoto, D.J. Siegel, Elastic properties of the solid electrolyte $Li_7La_3Zr_2O_{12}$ (LLZO), Chemistry of Materials 28(1) (2016) 197-206.

[7] D. Wang, C. Zhu, Y. Fu, X. Sun, Y. Yang, Interfaces in garnet-based all-solid-state lithium batteries, Advanced Energy Materials 10(39) (2020) 2001318.

[8] A. Sharafi, E. Kazyak, A.L. Davis, S. Yu, T. Thompson, D.J. Siegel, N.P. Dasgupta, J. Sakamoto, Surface chemistry mechanism of ultra-low interfacial resistance in the solid-state electrolyte $Li_7La_3Zr_2O_{12}$, Chemistry of Materials 29(18) (2017) 7961-7968.

[9] X. Xiang, Y. Zhang, H. Wang, C. Wei, F. Chen, Q. Shen, Improving the Interfacial Contact between $Li_7La_3Zr_2O_{12}$ and Lithium Anode by Depositing a Film of Silver, Journal of The Electrochemical Society 168(6) (2021) 060515.

[10] X. Han, Y. Gong, K.K. Fu, X. He, G.T. Hitz, J. Dai, A. Pearse, B. Liu, H. Wang, G. Rubloff, Negating interfacial impedance in garnet-based solid-state Li metal batteries, Nature Materials 16(5) (2017) 572.

[11] C.L. Tsai, V. Roddatis, C.V. Chandran, Q. Ma, S. Uhlenbruck, M. Bram, P. Heitjans, O. Guillon, $Li_7La_3Zr_2O_{12}$ interface modification for Li dendrite prevention, ACS Applied Materials & Interfaces 8(16) (2016) 10617-10626.

[12] H. Zheng, S. Wu, R. Tian, Z. Xu, H. Zhu, H. Duan, H. Liu, Intrinsic lithiophilicity of Li–garnet electrolytes enabling high-rate lithium cycling, Advanced Functional Materials 30(6) (2020) 1906189.

[13] W. Huang, Z. Bi, N. Zhao, Q. Sun, X. Guo, Chemical interface engineering of solid garnet batteries for long-life and high-rate performance, Chemical Engineering Journal 424 (2021) 130423.

[14] K.J. Kim, J.L. Rupp, All ceramic cathode composite design and manufacturing towards low interfacial resistance for garnet-based solid-state lithium batteries, Energy & Environmental Science 13(12) (2020) 4930-4945.

[15] E.J. Cheng, N.J. Taylor, J. Wolfenstine, J. Sakamoto, Elastic properties of lithium cobalt oxide ($LiCoO_2$), Journal of Asian Ceramic Societies 5(2) (2017) 113-117.

[16] C.Z. Zhao, B.C. Zhao, C. Yan, X.Q. Zhang, J.Q. Huang, Y. Mo, X. Xu, H. Li, Q. Zhang, Liquid phase therapy to solid electrolyte–electrode interface in solid-state Li metal batteries: a review, Energy Storage Materials 24 (2020) 75-84.

[17] E.J. Cheng, M. Shoji, T. Abe, K. Kanamura, Ionic liquid-containing cathodes empowering ceramic solid electrolytes, iScience 25(3) (2022) 103896.

[18] E.J. Cheng, T. Kimura, M. Shoji, H. Ueda, H. Munakata, K. Kanamura, Ceramic-based flexible sheet electrolyte for Li batteries, ACS Applied Materials & Interfaces 12(9) (2020) 10382-10388.

[19] E.J. Cheng, M. Liu, Y. Li, T. Abe, K. Kanamura, Effects of porosity and ionic liquid impregnation on ionic conductivity of garnet-based flexible sheet electrolytes, Journal of Power Sources 517 (2022) 230705.

[20] F. Han, J. Yue, C. Chen, N. Zhao, X. Fan, Z. Ma, T. Gao, F. Wang, X. Guo, C. Wang, Interphase engineering enabled all-ceramic lithium battery, Joule 2(3) (2018) 497-508.

[21] S. Iwasaki, T. Hamanaka, T. Yamakawa, W.C. West, K. Yamamoto, M. Motoyama, T. Hirayama, Y. Iriyama, Preparation of thick-film $LiNi_{1/3}Co_{1/3}Mn_{1/3}O_2$ electrodes by aerosol deposition and its application to all-solid-state batteries, Journal of Power Sources 272 (2014) 1086-1090.

[22] M. Sakakura, Y. Suzuki, T. Yamamoto, Y. Yamamoto, M. Motoyama, Y. Iriyama, Low-Resistive $LiCoO_2/Li_{1.3}Al_{0.3}Ti_2(PO_4)_3$ Interface Formation by Low-Temperature Annealing Using Aerosol Deposition, Energy Technology 9(5) (2021) 2001059.

[23] J. Akedo, Aerosol deposition of ceramic thick films at room temperature: densification mechanism of ceramic layers, Journal of the American Ceramic Society 89(6) (2006) 1834-1839.

[24] T. Kato, S. Iwasaki, Y. Ishii, M. Motoyama, W.C. West, Y. Yamamoto, Y. Iriyama, Preparation of thick-film electrode-solid electrolyte composites on $Li_7La_3Zr_2O_{12}$ and their electrochemical properties, Journal of Power Sources 303 (2016) 65-72.

[25] M. Shoji, H. Munakata, K. Kanamura, Fabrication of all-solid-state lithium-ion cells using three-dimensionally structured solid electrolyte $Li_7La_3Zr_2O_{12}$ pellets, Frontiers in Energy Research 4 (2016) 32.

[26] R. Inada, S. Yasuda, H. Hosokawa, M. Saito, T. Tojo, Y. Sakurai, Formation and stability of interface between garnet-type Ta-doped $Li_7La_3Zr_2O_{12}$ solid electrolyte and lithium metal electrode, Batteries 4(2) (2018) 26.

[27] R. Huggins, Advanced batteries: materials science aspects, Springer Science & Business Media2008.

[28] I.V. Krasnikova, M.A. Pogosova, A.O. Sanin, K.J. Stevenson, Toward standardization of electrochemical impedance spectroscopy studies of Li-ion conductive ceramics, Chemistry of Materials 32(6) (2020) 2232-2241.

[29] W. Choi, H.C. Shin, J.M. Kim, J.Y. Choi, W.S. Yoon, Modeling and applications of electrochemical impedance spectroscopy (EIS) for lithium-ion batteries, Journal of Electrochemical Science and Technology 11(1) (2020) 1-13.

[30] L.A. Middlemiss, A.J. Rennie, R. Sayers, A.R. West, Characterisation of batteries by electrochemical impedance spectroscopy, Energy Reports 6 (2020) 232-241.

Publications

1. Eric Jianfeng Cheng, Takeshi Kimura, Mao Shoji, Hiroshi Ueda, Hirokazu Munakata, Kiyoshi Kanamura*, *Ceramic-based flexible sheet electrolyte for Li batteries*, *ACS Appl. Mater. Interfaces*, 2020, 12, 10382–10388. (IF:10.383/ JCR: Q1) (Cited by 30)

2. Eric Jianfeng Cheng*, Mengyue Liu, Ying Li, Takeshi Abe, Kiyoshi Kanamura*, *Effects of porosity and ionic liquid impregnation on ionic conductivity of garnet-based flexible composite sheet electrolytes*, *J. Power Sources*, 2022, 517, 230705-230711 (IF: 9.794/JCR: Q1) (Cited by 10)

3. Eric Jianfeng Cheng*, Kei Nishikawa, Takeshi Abe, Kiyoshi Kanamura, Polymer-in-ceramic flexible separators for Li-ion batteries, *Ionics*, 2022, 28, 5089-5097 (IF: 2.961/JCR: Q3)

4. Eric Jianfeng Cheng*, Mao Shoji, Takeshi Abe, Kiyoshi Kanamura*, Ionic Liquid-Containing Cathodes Empowering Ceramic Solid Electrolytes, *iScience*, 2022, *25* (3), 103896-103913 (IF: 6.107/JCR: Q1/***Cell Press***) (Cited by 6)

5. Eric Jianfeng Cheng*, Ryo Oyama, Takeshi Abe, Kiyoshi Kanamura,* High-Voltage All-Solid-State Lithium Metal Batteries Prepared by Aerosol Deposition, *J. Eur. Ceram. Soc.*, 2023, 43, 2033-2038 (IF:6.364/ JCR: Q1)

6. Eric Jianfeng Cheng*, Yosuke Kushida, Takeshi Abe, Kiyoshi Kanamura*, Degradation mechanism of all-solid-state Li metal batteries studied by electrochemical impedance spectroscopy, *ACS Appl. Mater. Interfaces*, 2022, 14, 40881-40889 (IF:10.383/ JCR: Q1) (Cited by 5)

7. Eric Jianfeng Cheng*, Mayuko Kobayashi, Takeshi Abe, Kiyoshi Kanamura*, Aerosol deposition of $LiNi_{0.6}Co_{0.2}Mn_{0.2}O_2$ cathode film on $Li_7La_3Zr_2O_{12}$ ceramic electrolyte, To be submitted to *Acta Mater.*, (IF:9.210/ JCR: Q1)

8. Eric Jianfeng Cheng*, Takeshi Abe, Kiyoshi Kanamura,* Li-ion pathway in quasi-solid-state ceramic-based composite electrolyte, To be submitted to *J. Electrochem. Soc.*, (IF: 4.386/JCR: Q2)

9. Eric Jianfeng Cheng*, Huanan Duan, Michael J. Wang, Eric Kazyak, Hirokazu Munakata, Regina Garcia-Mendez, Bo Gao, Hanyu Huo, Tao Zhang, Ryoji Inada, Kohei Miyazaki, Takeshi Abe, Kiyoshi Kanamura, Garnet Solid Electrolytes: Current Status, Challenges, and Perspectives for Practical Application in Li-Metal Batteries, To be published in *Batteries*, (Invited review paper; IF: 5.938/JCR: Q2)

Acknowledgments

I am incredibly grateful to my Ph.D. advisor, Prof. Takeshi Abe, for taking me on as a student. I have significantly benefited from his guidance, kindness, patience, and wealth of knowledge.

Words cannot express my gratitude to my Ph.D. co-advisor, Prof. Kiyoshi Kanamura, for his guidance, financial support, encouragement, and expertise in the Energy Conversion and Storage field. In addition, I want to thank my dissertation committee members, Prof. Tetsuo Sakka and Prof. Hiroshi Kageyama, for their expertise, patience and dedication to my research.

I am also grateful to Prof. Hirokazu Munakata for his guidance in my research. I also want to thank Dr. Takeshi Kimura and Dr. Mao Shoji for their help and support over the years. Meanwhile, I gratefully recognize the contributions of Dr. Mengyue Liu, Mr. Yosuke Kushida, and Mr. Ryo Oyama to this study. Besides, I acknowledge the technical support I received from Dr. Kei Nishikawa.

I want to thank Prof. Kohei Miyazaki, Mr. Toshio Minowa, Dr. Jungo Wakasugi, Dr. Koshin Takemoto, Dr. Yuta Maeyoshi, Mr. Yuma Shimbori, Dr. Yong Zhang, Dr. Dong Ding, Dr. Jie Yu, Mr. Kazuaki Sawada, Ms. Miyu Motosaki, Ms. Mayuko Kobayashi, Ms. Ayaka Tajima, Mr. Makoto Saito, Mr. Kohei Fukuda, Dr. Danni Yu, Mr. Yuhang Ju, Ms. Jiayuan Ni and Ms. Xinli Gao for their help and kindness in making this journey more fulfilling.

I thank secretaries Ms. Yukiko Maekawa, Ms. Miho Kotani, Ms. Chiaki Toki, Ms. Yuka Tanaka, Ms. Yuri Kodera and Ms. Shoko Makino for their patience and support.

Finally, I must express my profound gratitude to my family, especially my parents, my wife and my kids for providing unfailing support throughout my years of study.